Theoretical and Numerical Studies of Frequency Up-shifted Ionospheric Stimulated Radiation

Hong Xi

Dissertation submitted to the faculty of the Virginia Polytechnic Institute and State University in partial fulfillment of the requirements for the degree of

Doctor of Philosophy
in
Electrical Engineering

Wayne A. Scales, Chair
Christopher A. Beattie
Ioannis M. Besieris
Gary S. Brown
Ahmad Safaai-Jazi

September 2004
Blacksburg, Virginia

Keywords: SEE, BUM, Particle-In-Cell Code, Numerical Simulation, Four Wave Decay Process, Ring-Plasma Instability

Theoretical and Numerical Studies of Frequency Up-shifted Ionospheric Stimulated Radiation

Hong Xi

(ABSTRACT)

Stimulated electromagnetic emission (SEE) produced by interactions of high-power radio waves with the Earth's ionosphere is currently a topic of significant interest in ionospheric modification physics. SEE is believed to be produced by nonlinear wave-wave interactions involving the electromagnetic and electrostatic plasma waves in the altitude region where the pump wave frequency is near the upper hybrid resonance frequency. The most prominent upshifted feature in the SEE spectrum is the broad upshifted maximum (BUM). In this study, the instability processes thought to be responsible to the BUM spectra in the SEE experiments are discussed and analyzed using theoretical and electrostatic particle-in-cell (PIC) models.

From characteristics of this feature, a four-wave parametric decay process has been studied as a viable mechanism for its production. The object is to (1) investigate the early time nonlinear development of the four-wave decay instability by using theoretical and numerical simulation models, (2) study the variation of the four-wave decay instability spectral features for a wide range of plasma and pump wave parameters, and (3) access its possible role in the production of the BUM spectral feature. Results of this investigation show that there is good agreement between predictions of the proposed theoretical model and the numerical simulation experiments. The simulation electric field power spectrum exhibits many of the important features of the experimental observations. The numerical simulation results show that consideration of the full nonlinear development of the four-wave parametric instability is crucial in providing insight into the asymmetric nature of the wave frequency spectrum observed during the experiments.

The velocity-space ring-plasma instability, another generation mechanism for the BUM spectra, is studied using a theoretical model. The theoretical calculations show that the growth rate is larger in the region of the upper hybrid wave than that of the electron Bernstein wave. In addition, the effects of various plasma parameters are analyzed and it is predicted that the BUM should be more prominent with a hotter ring, at the direction perpendicular to the magnetic field, or in a closer region of cyclotron harmonic. A detailed comparison of the velocity space ring-plasma instability and the four-wave parametric process is presented where both the differences and the possible relations are discussed.

Acknowledgments

First and foremost I would like to express my deepest and sincere gratitude to my advisor, Dr. Wayne A. Scales, for his valuable advice, guidance and encouragement during the course of this work. I sincerely appreciate his enthusiasm and patience in guiding me during this research work. His insight, kindness, and genuine concern for his students made working with him a truly memorable experience.

I am also grateful to Professors Christopher A. Beattie, Ioannis M. Besieris. Gary S. Brown, and Ahmad Safaai-Jazi for their time spent serving on my advisory committee.

No words can express my gratitude to my parents, parents-in-law, sisters and brother for endless encouragement, support, and kind words throughout my life.

Special thanks to my lovely wife, Yan, and daughter, Belinda for their love and encouragement and for bringing joy to me everyday.

This work was supported by the National Science Foundation under grant ATM-9713717.

Contents

List of Figures

List of Tables

Chapter 1

Introduction

The study of nonlinear waves in the ionospheric plasma has been a topic of considerable interest during the past two decades. Some of the important phenomena include the excitation of plasma waves, generation and saturation of parametric instabilities, and cavitons (soliton waves). Such disturbances in the upper atmosphere affect the performance of communication systems, navigation systems such as GPS, and power systems. Traditionally, in the analysis of such systems the effects of these disturbances are modeled as stochastic noises. A predictive capability for these disturbance is essential as the world becomes more and more dependent on high-performance electrical devices. Experiments conducted in the laboratory environments have been helpful for expanding our knowledge of plasma physics. However, such investigations are impeded by the effects of physical boundary conditions imposed by laboratory instruments. On the other hand, the Earth's ionospheric plasma presents a natural laboratory because the relevant experimental parameters, such as electron and ion densities, temperature, and collision frequency, vary smoothly with altitude. Ground-based waves can be used to probe and/or perturb the ionosphere, and consequently are varied to study plasma-wave interactions in this natural laboratory environment. Diagnostics and analysis of the reflected radio waves provide abundant information revealing the physical conditions and processes occurring in this region of the upper atmosphere.

In the past two decades, a number of such heating facilities have been built in Europe, Russia and the United States to conduct these experimental radio science research including plasma-wave interactions. These heating facilities include HIPAS facility and HAARP facility in Alaska, EISCAT facility in Tromsø, Norway; SURA facility in Nizhniy Novgorod, Russia; and Arecibo facility in Peurto Rico. The locations of these heating facilities depend on the orientation of the Earth's geomagnetic field. Current topics of interest in ionospheric modification research include such diverse aspects as modification of polar electrojet and ELF/VLF generation, hot electrons and artificial airglow emissions, large scale density and temperature modifications and generation of electrostatic waves, parametric instabilities and production of small-scale density irregularities.

Stimulated electromagnetic emission (SEE) has been observed during these ionospheric modification experiments when a powerful high-frequency, ordinary mode (*O*-mode) pump wave is transmitted from heating facilities as a result of a complicated series of interactions between the HF radiowave pump (the heater) and the internal plasma waves in the ionized upper atmosphere. A schematic representation of the experimental geometry involved is illustrated in Figure (1.1). The SEE exhibits frequency sidebands upshifted and downshifted from the pump wave frequency within roughly 100 kHz bandwidth. Interest in SEE has been steadily growing since it was first experimentally observed [*Thidé et al.,* 1982] because it may be used as a diagnostic tool for the ionosphere and it is also a fundamental nonlinear plasma phenomenon [*Stenflo,* 1990] that is not well understood. A classification of SEE spectral features and the description of their possible generation through parametric decay instability processes were provided by *Stubbe et al.* [1984]. Some of the important SEE features that consist of frequency-downshifted sidebands are the downshifted maximum (DM), the broad downshifted maximum (BDM), and the downshifted peak (DP). Some of the frequency-upshifted sidebands are the broad upshifted maximum (BUM) and the upshifted maximum (UM). There are other less prominent components, and new ones are likely to be discovered with continued experimentation. More details about these features will be provided in Chapter 2. Plasma structures that are believed to be involved in the production of these emissions include small-scale, field-aligned electron density irregularities (striations), upper hybrid (UH) and lower hybrid (LH) waves, and electron Bernstein (EB) waves.

The BUM is one of the most prominent upshifted features in the SEE spectrum and a likely indicator of wave-wave and wave-particle interactions occurring during ionospheric heating experiments. It has been the subject of intensive investigations in past ionospheric modification experiments [*Leyser et al.,* 1989, 1993; *Stubbe et al.,* 1994; *Frolov et al.,* 1996, 1997, 1998; *Wagner et al.,* 1999]. The BUM is a broad upshifted sideband extending more than 100 kHz above the pump frequency and develops only when the pump frequency ω_0 is in the vicinity of harmonics of the electron cyclotron frequency, $n\Omega_{\text{ce}}$. It is widely considered that the BUM develops for ω_0 slightly above $n\Omega_{\text{ce}}$. However, it was also reported that the BUM could appear when the pump frequency is a few tens of kHz below the gyroharmonic frequency [*Frolov et al.*, 1996]. When the pump frequency is more than 25 kHz above the gyroharmonic frequency, as it is for most experiments where the BUM is observed, the frequency of the BUM peak ω_{BUM} follows closely the empirical relation $\omega_{\text{BUM}} = 2\omega_0 - n\Omega_{\text{ce}}$ [*Leyser et al.*, 1989; *Stubble et al.,* 1994; *Frolov et al.,* 1996, 1997]. Recently, extensive SEE measurements were conducted at the SURA ionospheric modification facilities of the Radiophysical Research Institute (NIRFI) of Nizhniy Novgorod, Russia [*Frolov et al.*, 1996, 1997, 1998; *Wagner et al.*, 1999]. Various experimental conditions and plasma

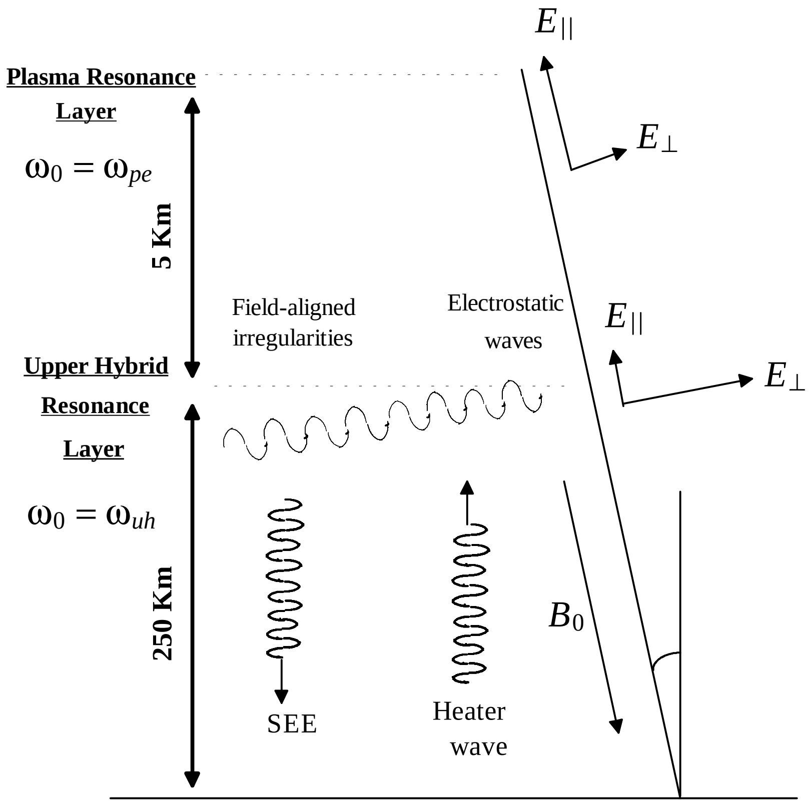

Figure 1.1: A schematic diagram showing the experimental geometry for the generation of SEE. Usually high powered heater waves are sent from an antenna array. The radio waves interact with the charges, the electric and magnetic fields in the plasma. The radiated secondary waves are received on the ground.

and pump wave parameters, which include the number of individual pumps, their powers, frequencies, polarizations, and on-off patterns, were used to investigate the effects on the BUM behavior. Other major findings of these experiments include the two-component nature of the BUM [*Frolov et al.*, 1998] and the ionospheric self-conditioning and preconditioning effects on the BUM components [*Wagner et al.*, 1999].

The empirical relation $\omega_{\mathrm{BUM}} = 2\omega_0 - n\Omega_{\mathrm{ce}}$ suggests that the BUM feature is generated through a four-wave interaction, involving two pump photons or upper hybrid plasmons, a decay mode at $n\Omega_{\mathrm{ce}}$, and a stimulated radiation at ω_{BUM} [*Leyser et al.*, 1989, 1990; *Bud'ko and Vas'kov*, 1992; *Goodman et al.*, 1993; *Tripathi and Liu*, 1993; *Huang and Kuo*, 1994]. In the generation mechanism proposed by *Tripathi and Liu* [1993] and *Goodman et al.* [1993], the BUM is produced by nonlinear mixing of lower and upper hybrid waves through a two-step process. The first step involves the parametric decay of the *O*-mode heater wave into a lower hybrid decay and a frequency downshifted electron Bernstein wave. In the second step, frequency upshifted *O*-mode emissions are produced through a scattering process. Thus the upper hybrid waves, generated through a direct conversion of the HF heater wave, are converted into frequency upshifted *O*-mode emissions by scattering off the parametrically excited lower hybrid waves. *Huang and Kuo* [1994] pointed out that the difficulty of using the two-step process to explain the asymmetric feature of the BUM spectrum lies in the assumption used in their theory that the frequency-downshifted *O*-mode emissions produced in the second step of the scattering process must be strongly cyclotron damped. *Bud'ko and Vas'kov* [1992] and *Huang and Kuo* [1994] developed theoretical models for a four-wave interaction process involving the decay of the pump wave into a frequency-upshifted upper hybrid wave, a frequency-downshifted electron Bernstein wave, and a lower hybrid wave. They proposed that nonlinear mixing of the upshifted electrostatic sideband with the field-aligned ionospheric irregularities produces beat currents that radiate the SEE observed on the ground. *Huang and Kuo* [1994] showed that the first-order process of *Bud'ko and Vas'kov* [1992] was not operative for conditions consistent with past experimental observations. Those studies are usually limited to a set of parameters and applicable to the linear growth period.

A completely different generation mechanism for the BUM feature was proposed by *Grach* [1999] that considers the effects related to acceleration of electrons perpendicular to the background magnetic field by high-frequency plasma turbulence. The electron velocity distribution modified over the transverse velocities in the presence of Coulomb collisions may form a velocity space ring distribution with $\partial f/\partial v_\perp > 0$ which may be unstable to upper hybrid and electron Bernstein waves. It is possible for such an instability to be more efficient at generating upper hybrid than electron Bernstein waves which would result in an upshifted asymmetric spectrum. This theory is still a preliminary one thus a detailed discussion is needed to study the full process and the effects of varying plasma parameters.

1.1 Objectives

Both the four-wave second-order process [*Huang and Kuo*, 1994] and the velocity ring-plasma instabilities [*Grach*, 1999] have been successful in interpreting some aspects of the experimental observations of the BUM. However, the asymmetric nature of the spectrum that is a fundamental feature of the experimental observations is still open to questions within the framework of past purely theoretical investigations. Furthermore, past work has not considered the full nonlinear development of the four-wave decay instability and the important consequences to the experimental SEE spectrum. Although numerical simulations may ultimately provide important contributions to the understanding of nonlinear processes and bridge the gap between theoretical development and experimental observations, there have been few studies in the past [*Goodman et al.*, 1994; *Scales et al.*, 1997; *Hussein and Scales*, 1997; *Hussein et al.*, 1998]. The purpose of this work is to blend the gap between the generation theories and the heating experiments by using theoretical models and numerical simulations to verify and predict experimental results of the BUM. We will discuss in detail the possible role of the four-wave decay process and that of the velocity space ring-plasma instability. We will interpret the behavior of the BUM spectral features for a wide range of plasma and pump wave parameters. Particularly effects of varying the harmonic number and the frequency offset $\Delta\omega_0 = \omega_0 - n\Omega_{\rm ce}$ will be examined in detail. Our in-depth studies of these two instabilities will also enable us to conduct a detailed comparison of their roles in producing the asymmetric spectrum and discuss their possible relationship. The predictions from this study will provide interpretation of many of the past important observations of the SEE experimental data, as well as insight into the nonlinear processes that could occur during ionospheric heating experiments, the design of future experiments, and the usage of the SEE as a diagnostic tool.

1.2 Organization

The remainder of this dissertation is organized as follows. In Chapter 2 we provide an overview on important plasma parameters, the SEE, and the BUM. Chapter 3 discusses the theoretical model of the four-wave electrostatic parametric process for various plasma and pump wave parameters. Chapter 4 covers the Particle-In-Cell (PIC) simulation model and numerical results based on the four-wave model. Next chapter discusses the theoretical model of the velocity ring-plasma instability along with a comparison with the four wave process. Finally, Chapter 6 will discuss the conclusions and future work.

Chapter 2

Plasma Parameters and SEE

In this chapter, we will review some of the basic plasma theory. The objective is to define and develop the important concepts that will appear in the discussion of the stimulated electromagnetic emissions (SEE) and the broad up-shifted maximum (BUM) in this chapter and the following chapters. These concepts include physical plasma parameters such as plasma frequency, cyclotron frequency, and Debye length. We then discuss important waves in the plasma including upper hybrid waves, Bernstein waves, and ion waves. After that, some of the important SEE spectral features including the BUM are presented. Finally we discuss a generation mechanism for the SEE and explain the feasibility of using a particle-in-cell simulation model to conduct our investigation.

2.1 The ionosphere is a plasma

The ionosphere, the ionization layer of the Earth's upper atmosphere, is essentially a plasma. The structure of the Earth's upper atmosphere can be described in several ways, and each leads to a classification of the altitude regions that is appropriate to the physical process under consideration. Four commonly used classifications are:

- Classification via temperature (e.g. troposphere, mesosphere, etc.)
- Classification via chemical composition (e.g. homosphere, heterosphere, etc.)
- Classification via ionization (e.g. ionosphere, magnetosphere, etc.)
- Classification via dynamics/mixing (e.g. barosphere, exosphere, etc.)

In this work, we will focus on the ionization layer known as the ionosphere shown in Figure (2.1). At high altitudes the radiation from the sun causes substantial

Ionospheric Layer	Altitude	Electron density
D	60-90 km	$10^8 - 10^{10}\,\mathrm{m}^{-3}$
E	105-160 km	several $10^{11}\,\mathrm{m}^{-3}$
F1	168-180 km	several $10^{11} - 10^{12}\,\mathrm{m}^{-3}$
F2	maximum variable around 300 km	up to several $10^{12}\,\mathrm{m}^{-3}$

Table 2.1: Daytime Classification of layers in the ionosphere.

photoionization of the upper atmosphere. This results in significant numbers of free electrons and free ions which usually tend to recombine. However, in the ionosphere, the recombination of ions and electrons is slow due to low gas densities. Thus, the ionosphere is a region characterized by a relatively high density concentration of both free electrons and free ions. In general, any region that has the same characterization is classified as a plasma.

A plasma state is the fourth state of matter: heating a solid makes a liquid, heating a liquid makes a gas, heating a gas makes a plasma. At low temperatures collisions between atoms are rare, and these collisions do not have enough energy to ionize one or both atoms. However, as a gas heats up the number of collisions between atoms, with energy sufficient enough to ionize the atoms, increases. At a certain point the number of ionized atoms will increase enough that there is an abrupt change in the ratio between ionized and neutral atoms. At this point we are no longer talking about a gas, but a plasma. It is possible for a plasma to heat up enough that the number of ionized atoms will exceed the number of neutral atoms, making the plasma fully ionized.

A plasma can also be considered a quasineutral gas of charged and neutral particles which exhibits a collective behavior.

The ionosphere, being a plasma and a conducting medium, supports propagation and reflection of radio waves, depending on their frequencies; thus, allowing for long distance radio communication.

The ionosphere is classified into vertical regions. This vertical structure is continuously changing, and varies from day to night, with the seasons of the year, and with the latitude. The daytime characteristics of the ionospheric layers are summarized in Table 2.1.

The E and F layers are the most important layers for radio communications in the frequency range of 3 to 30 MHz. Electromagnetic waves with a frequency above 40 MHz are able to penetrate through the ionosphere. In the D region, only waves of 2

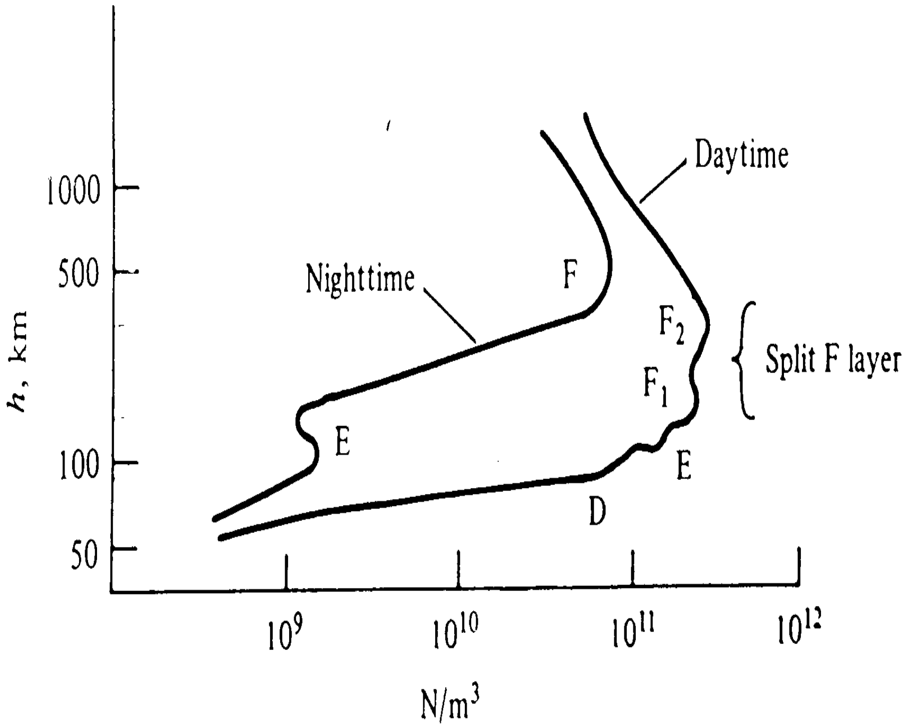

Figure 2.1: A plot showing the variation of the ionospheric density with height [*Collin, 1985*].

MHz and below are reflected. This is because the D region has a much lower electron density than the other layers. The D region also has a much larger collision frequency, due to a high neutral density.

Understanding the development of irregularities in the plasma is one of the most active areas of ionospheric research. There are many physical processes that can produce irregularities. One set of physical processes that we are interested in are plasma instabilities. There are several different classifications of plasma instabilities, but all of them are caused by waves produced by free particles in the ionosphere.

2.2 Basic plasma physics

2.2.1 Plasma oscillations and plasma frequency

If the electrons in a plasma are displaced from a uniform background of ions, electric fields will be set up, causing the electrons to be pulled back toward the much less mobile ions. Because of their inertia, the electrons will overshoot and oscillate around their equilibrium positions with a frequency known as the plasma frequency ω_p. Their oscillations are so fast such that the massive ions may be assumed fixed. The plasma frequency is given by the expression:

$$\omega_p{}^2 = \frac{q^2 n_0}{m \epsilon_0} \tag{2.1}$$

where, ω_p is the plasma frequency, q, n_0, m are the charge, charge density and the mass of the species respectively, and ϵ_0 is the permittivity of free space.

2.2.2 Cyclotron frequency

If a constant magnetic field is applied on a charged particle, the particle will experience a cyclotron gyration with a frequency known as the cyclotron frequency (gyrofrequency) Ω_c. The cyclotron frequency is given by:

$$\Omega_c = \frac{qB}{m} \tag{2.2}$$

where, Ω_c is the cyclotron frequency, q, m are the charge and mass of the species respectively, and B is the applied magnetic field magnitude.

2.2.3 Debye Shielding

A fundamental characteristic of the plasma is its ability to shield out electric potentials that are applied to it for the majority of the plasma. Suppose an electric field is applied into a plasma by putting two charged metal surfaces connected to a battery. The charged surfaces would attract potentials of opposite charges and almost immediately a cloud of ions will surround the negatively charged surface and a cloud of electrons will surround the positively charged surface. If the plasma were cold and there were no thermal motions, there would be just as many charges in the cloud as on the surface, and the shielding would be perfect. No electric field in this case would be present in the body of the plasma outside the cloud. On the other hand, if the temperature is finite, the particles that are at the edge of the cloud, where weak electric field is present, would have enough thermal energy to escape from the electrostatic potential well. The edge of the cloud occurs at the radius where the potential energy is approximately equal to the thermal energy KT, where K is Boltzman's constant and T is the temperature of the species, and the shielding is not complete. Potentials of the order KT/q can leak into the plasma and cause a finite electric field to exist [*Chen,* 1984]. A measure of the plasma shielding is called the Debye length λ_D which is given by :

$$\lambda_D = \sqrt{\frac{\epsilon_0 K T_e}{n q_e^2}} \tag{2.3}$$

which is a measure of the shielding distance. Note that describing the plasma as a quasineutral gas means that its neutral enough to assume $n_i = n_e = n$ where n is the plasma density.

2.2.4 Criteria for plasmas

An ionized gas is called a plasma if it satisfies the following three criteria:

- the Debye length is much smaller than other physical dimensions of interest, for example, the plasma system length; and
- there are a lot of charged particles inside a "Debye sphere" whose radius equals a Debye length, in order to enable the Debye shielding to be statistically valid; and
- the collision frequency between charged and neutral particles is small compared with the frequency of typical plasma oscillations. In other words, $\omega_p \tau > 1$, where τ is the mean time between collisions with neutral atoms.

The upper ionosphere meets all these three criteria. Therefore it is considered as a plasma.

2.2.5 Upper hybrid frequency

Assume that high frequency electrostatic electron oscillations propagate at right angles to the background geomagnetic field. These electrostatic electron waves across B will oscillate with the frequency called the upper hybrid frequency, ω_{uh}. The upper hybrid frequency is given by

$$\omega_{uh}^2 = \omega_{pe}^2 + \Omega_{ce}^2 \tag{2.4}$$

where, ω_{uh} is the upper hybrid frequency, ω_{pe} is the electron plasma frequency, and Ω_{ce} is the electron cyclotron frequency. Note that those are different oscillations than those along B which are the usual plasma oscillations with $\omega = \omega_p$.

2.2.6 Bernstein Waves

The Bernstein Waves are electrostatic waves propagating at right angles to B at harmonics of the cyclotron frequency, $n\Omega_c$.

2.2.7 Electrostatic ion waves perpendicular to B_0

Assume k, the wave vector, is almost perpendicular to the background magnetic field B_0. Assume also an infinite plasma in equilibrium with uniform density, n_0 and magnetic field B_0. Also the assumption of cold ions is considered, i.e T_i=0. The geometry is shown in Figure (2.2). The angle $\pi/2 - \theta$ is taken to be so small that we may take $E = E_1\hat{x}$ as far as ions are concerned. For the electrons, however, it makes a great difference whether $\pi/2-\theta$ is zero or small and finite. The electrons have small Larmor radii that they cannot move in the x-direction to preserve charge neutrality; all that the E field does is make them drift back and forth in the y direction. If θ is not exactly $\pi/2$, the electrons can move along the dashed line (along B_0) to carry charge from negative to positive regions in the wave and carry out Debye shielding. The ions cannot do this effectively because their inertia prevents them from moving such a long distance in a wave period. This critical angle $\pi/2 - \theta$ is proportional to the ratio of ions to electrons thermal velocity which is proportional to $\sqrt{m_e/m_i}$. Considering the plasma approximation $n_i = n_e$, the dispersion equation of the ion cyclotron waves is obtained [*Chen,* 1984], which is given by:

$$\omega^2 = \Omega_{ci}^2 + k^2 v_s^2 \tag{2.5}$$

where, Ω_{ci} is the ion cyclotron frequency, k is the wave number, v_s is the electron oscillating velocity.

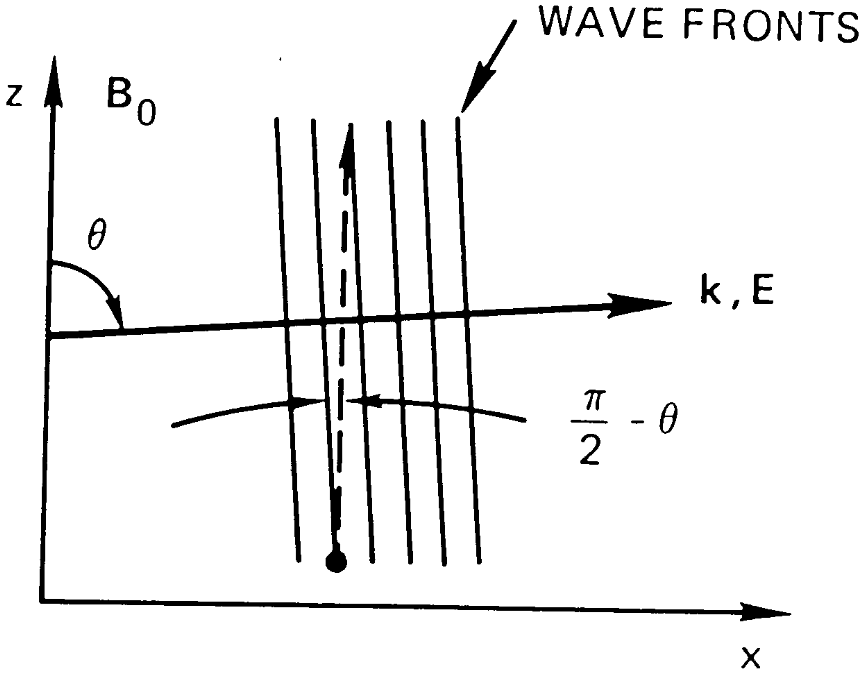

Figure 2.2: A plot showing the geometry of an ion cyclotron wave propagating nearly at right angles to B_0 [*Chen, 1984*].

Now, consider the case with θ is exactly equal to $\pi/2$, and the electrons are not allowed to preserve their charge neutrality by flowing along the lines of force. Assuming also that the electron mass is finite and considering the plasma approximation $n_i = n_e$, we obtain the frequency called the lower hybrid frequency ω_{lh} [*Chen,* 1984] which is given by

$$\omega_{lh} \equiv \sqrt{\Omega_{ci}\Omega_{ce}} \tag{2.6}$$

where Ω_{ci} and Ω_{ce} are the ion cyclotron and electron cyclotron frequencies respectively. Note that the lower hybrid oscillations are only observed when θ is very close to $\pi/2$.

2.2.8 Parametric instability

Ion density fluctuations may couple an electromagnetic wave into an electron plasma wave to give us an electric field $\tilde{E}$. In turn, the electron plasma wave beats with the electromagnetic wave to generate a spatial variation in the electric field intensity which can enhance the ion density fluctuations via the ponderomotive force. Hence, a feedback loop is formed and depending on the pump amplitude, instability can result. Such instability is called parametric instability, with the parameter being the wave's amplitude.

In order for the parametric instability to occur, a minimal set of common characteristics is required:

- Matching conditions

  The spatially varying electric field E_0 which is resulting from beating of two waves requires a two-wave number matching condition to produce sustaining instability. Mathematically,

  $$k_0 = k_i + k_s \tag{2.7}$$

  where the scripts "0"," i" and "s" stand for the pump, idler and the signal respectively. In the SEE problem, the electromagnetic wave is the pump, the electron plasma wave is the idler, and E_0 is the signal. The wave number matching condition is equivalent to *conservation of momentum.*

  The parametric instability also has to satisfy the *conservation of energy* to take place. This translates into the frequency matching condition

  $$\omega_0 = \omega_i + \omega_s \tag{2.8}$$

- Threshold

  The instability can occur only when the pump amplitude is above a critical value in order to maintain the feedback growth. If the pump amplitude is below the instability threshold, even a small amount of either collision or Landau damping will prevent the instability from occurring.

Figure (2.3) shows the parallelogram construction for the parametric decay instability process. Here, (ω_0, k_0) is an incident electromagnetic wave of large phase velocity $(\omega_0/k_0 \simeq c)$. It excites an electron wave and an ion wave moving in opposite directions. Since $|k_0|$ is small we have $|k_1| \simeq -|k_2|$ and $\omega_0 = \omega_1 + \omega_2$ for this instability. It should be noted that the BUM feature involves four waves and is a result of a more complex process than the three wave parametric decay process shown here.

2.3 Stimulated Electromagnetic Emission (SEE)

Stimulated electromagnetic emissions (SEE) are high-frequency (HF) radio emissions that are generated as a result of a complicated series of interactions between a high-power, ordinary mode (O-mode), HF radiowave pump (the heater), and internal plasma waves in the ionized upper atmosphere. The internal waves include upper hybrid, lower hybrid, and ion cyclotron waves. The SEE spectrum exhibits sidebands that are up-shifted and down-shifted from the pump wave within roughly about several tens of KHz bandwidth.

The SEE is a very important diagnostic tool for studying parametric instabilities and other nonlinear physical processes that may occur around the heated region. It is noted that the spectrum from SEE may be used to measure the electric field strength in the heated region. The SEE spectrum is used in many experimental observations to measure the magnitude of the background magnetic field. The results show that the SEE can be a very important diagnostic tool and it is also considered a fundamental plasma phenomenon.

The classification of SEE spectral features and the description of their generation through parametric decay instability processes was provided by *Stubbe et al.* [1984]. The SEE spectral sidebands were found to depend on a number of ionospheric parameters in addition to the pump wave. It was also postulated that the sidebands in the SEE spectrum should develop in the altitude region where ω_0 is near the plasma upper hybrid frequency ω_{uh}. It was also found that this spectrum is dependent on the proximity of ω_0 to the harmonics of the electron cyclotron frequency $n\Omega_{ce}$.

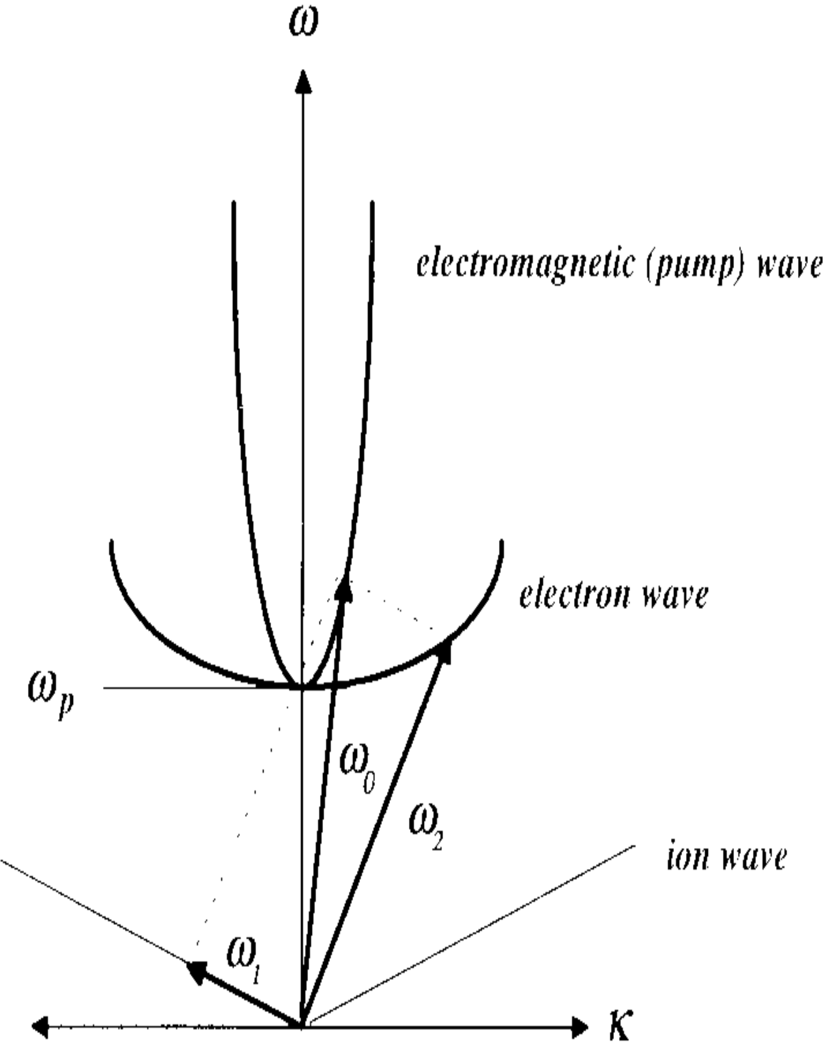

Figure 2.3: A parallelogram construction illustrating the parametric decay instability process [*Chen, 1984*].

In the following, we discuss some of the SEE spectral features sidebands which extend above and below the pump frequency by multiples of the lower hybrid frequency or less than a lower hybrid frequency. Emphasis will be placed on the Broad up-shifted maximum (BUM) that is our primary interest in this work.

2.3.1 Downshifted maximum (DM)

The downshifted maximum DM is one of the prominent SEE spectral features. This sideband in the SEE spectrum has a frequency shift below the pump frequency approximately equal to the local plasma lower hybrid frequency ω_{lh}. The theoretical studies of the DM considered the generation through the parametric decay of the electromagnetic pump wave into upper hybrid waves. The upper hybrid waves either decay into a lower hybrid wave and an O-mode wave [*Murtaza and Shukla*, 1984; *Leyser et al.*, 1990; *Stenflo and Shukla*, 1992] or decay into a lower hybrid wave and an electrostatic upper hybrid electron Bernstein wave which is scattered by field-aligned irregularities into electromagnetic waves that are observed on the ground [*Zhou et al.*, 1994]. Some of the experimental results showing the DM and the cascading structure of the DM are shown in Figure (2.4).

2.3.2 Downshifted peak (DP)

Another SEE spectral feature is the downshifted peak DP. The DP is a downshifted sideband which is usually observed when the pump frequency is very close to the third harmonic of the electron cyclotron frequency $3\Omega_{ce}$. Its offset frequency from the pump is about 2 KHz. It was postulated by *Huang and Kuo* [1995] that the generation mechanism for the DP feature is through parametric decay of an electron Bernstein pump wave into an electron Bernstein sideband wave and a nearly perpendicularly propagating ion acoustic or electrostatic ion cyclotron decay wave. Some experimental results are shown in Figure (2.5). The figure shows the down shifted peak extending below ω_0 by a factor less than a lower hybrid frequency ω_{lh}. It was also noted that the DP may appear in a cascading structure when the upper hybrid resonance frequency is equal to third electron cyclotron harmonic $\omega_{uh} = 3\Omega_{ce}$ (double resonance) and ω_0 is very close to $3\Omega_{ce}$. An experimental result showing the cascading of the DP is also shown in Figure (2.5).

2.3.3 Continuum feature

It is an asymmetric feature, with more energy on the down-shifted side. The width of the down shifted portion of the continuum is strongly variable, ranging from a

Downshifted Maximum (DM) [Thide` et al., 1982]

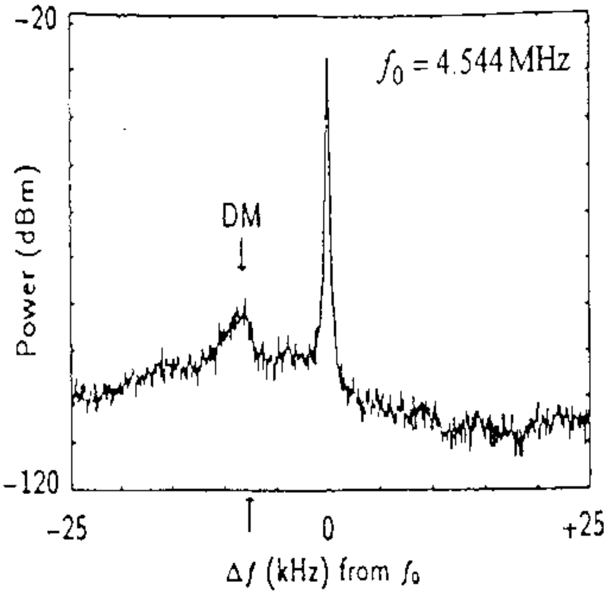

Downshifted Maximum (DM) [Leyser et al., 1990]

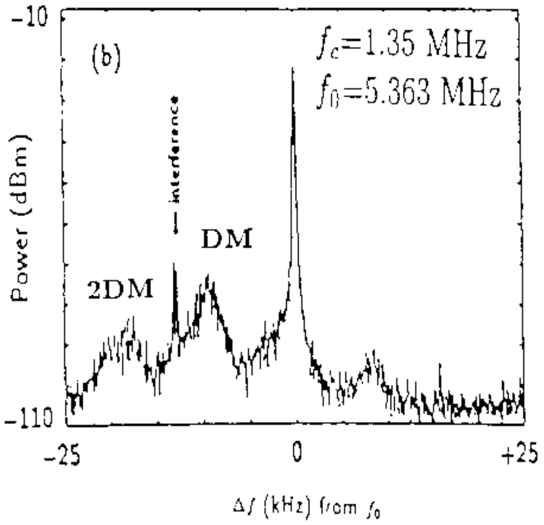

Figure 2.4: Two results from experimental data showing the DM and the cascading of the DM.

Downshifted Peak (DP) [Leyser et al., 1990]

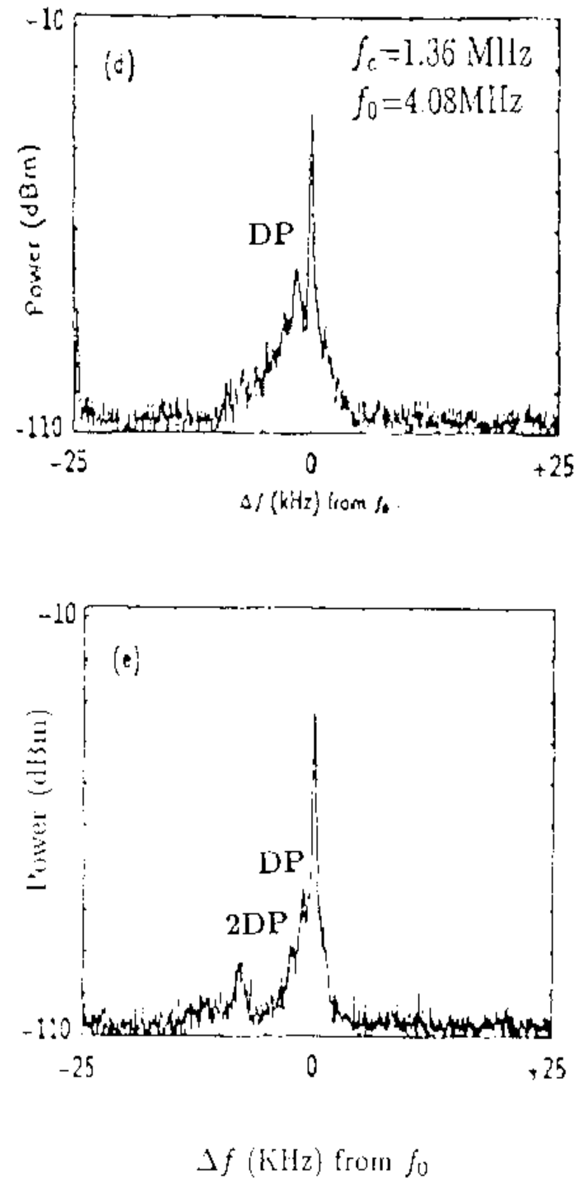

Figure 2.5: Two results from experimental data showing the DP and the cascading of the DP.

few KHz, Narrow Continuum NC, to as much as 100 KHz, Broad Continuum BC. A result from experimental data for the continuum feature is shown in Figure (2.6).

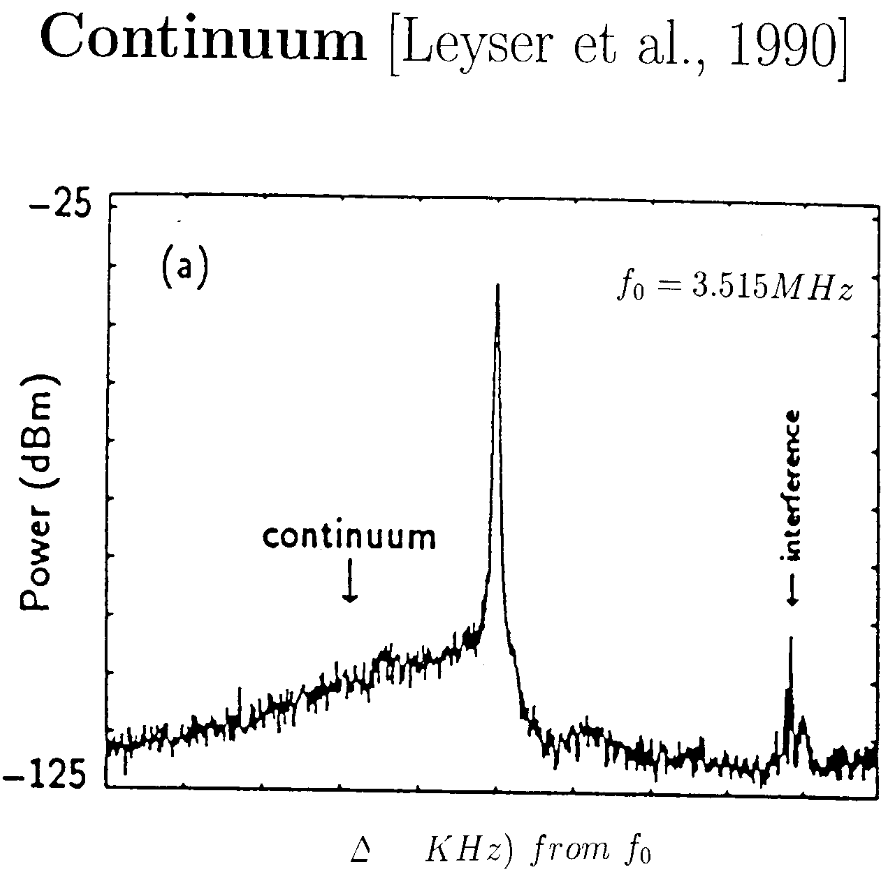

Figure 2.6: A result from experimental data showing the continuum structure.

2.3.4 Upshifted maximum (UM)

It is an up-shifted sideband mostly seen with the DM. The frequency shift of the UM from the pump frequency is about 5 to 9 KHz. This feature is much weaker than the DM. Figure (2.7) shows the UM during a heating experiment.

Broad Symmetric Structure (BSS) [Stubbe et al. 1990]

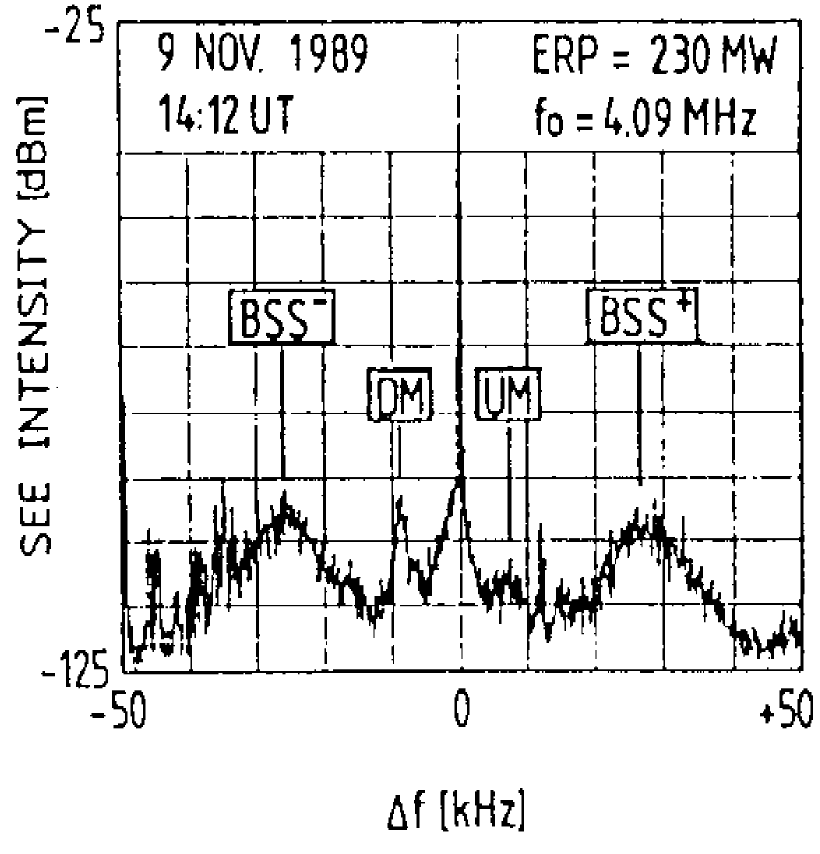

Figure 2.7: A result from experimental data showing the BSS.

2.3.5 Broad symmetrical structure (BSS)

It is a symmetrical structure composed of two equal sidebands symmetrical about the pump frequency by about 15 to 30 KHz. The BSS has the narrowest pump frequency range of existence among all the primary features and occurs for pump frequencies in the range of 40 KHz near 3 f_{ce}, which is very similar to the DP feature. An experimental result for the BSS is shown in Figure (2.7).

2.3.6 Broad downshifted maximum (BDM)

It is a broad down-shifted sideband which is often observed accompanying the presence of the BUM. It has a broad frequency spread like the BUM with a smaller amplitude. Figure (2.8) shows the BDM during a heating experiment.

2.3.7 Broad upshifted maximum (BUM)

The BUM is one of the most prominent up-shifted features in the SEE spectrum and has been the subject of intensive investigation in past ionospheric modification experiments. The behavior of the BUM with pump frequency is relatively complex. The BUM is a broad upshifted sideband extending more than 100 kHz above the pump frequency and develops only when the pump frequency ω_0 is in the vicinity of harmonics of the electron cyclotron frequency, $n\Omega_{\rm ce}$. A typical BUM spectrum is shown in Figure (2.8). The BUM appears continuously over a range of pump frequencies starting at 10 kHz below the gyroharmonic frequency [*Frolov et al.,* , 1996] and continuing to a maximum frequency (f_{pmx}) 100 kHz above the gyroharmonic frequency [*Leyser et al.,* 1989, 1993; *Stubbe et al.,* 1994; *Frolov et al.,* 1996, 1997, 1998; *Wagner et al.,* 1999]. The frequency of the BUM peak (f_{Bpk}) follows a linear dependence on the pump frequency given by $f_{Bpk} = 2f_0 - nf_{ce}$. This relationship is conveniently expressed as $\triangle f_{Bpk} = \triangle f_0$ where $\triangle f_{Bpk} = f_{Bpk} - f_0$ and $\triangle f_0 = f_0 - nf_{ce}$.

Recent evidence [*Frolov et al.* 1997, 1998] suggests that there are actually two components of the BUM, namely, the BUM$_1$, and the BUM$_2$. BUM$_1$ is found only at pump frequencies in close proximity to the gyroharmonic, while BUM$_2$ is present more generally over a range of pump frequencies in the vicinity of the gyroharmonic. These two components are possibly caused by different physical processes and thus need to be treated separately. An important characteristic of the BUM$_1$ feature is that it may exist for pump frequencies ω_0 slightly below the cyclotron harmonic frequency $n\Omega_{\rm ce}$. In this work we will discuss the possible roles of the four-wave decay instability and

Broad Upshifted Maximum (BUM) [Stubbe et al. 1984]

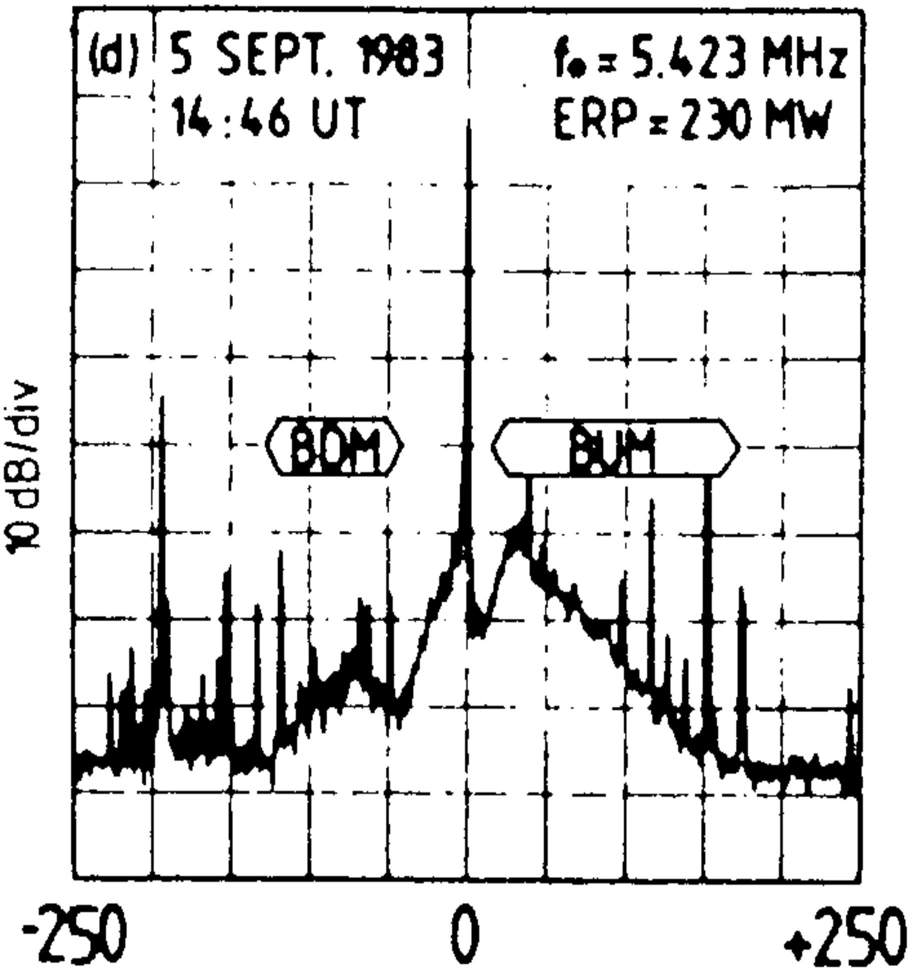

Δf (KHz) from f_0

Figure 2.8: Experimental data result showing the BUM and BDM features.

the velocity ring-plasma instability in the production and moderation of the BUM feature.

2.4 SEE generation mechanism

An electrostatic particle-in-cell simulation model was used in our study to study the SEE. To explain the reasoning for this simulation model we need to discuss the generation mechanism of SEE. Past theoretical and simulation studies have predicted that the development of frequency sidebands in the SEE spectrum are produced by interactions between electrostatic waves which are scattered into electromagnetic waves to produce the observed stimulated waves [*Zhou et al., 1994; Goodman et al., 1994; Mjølhus et al., 1995*]. A theoretical model for SEE generation is shown in Figure (2.9). When an *O*-mode heater wave is launched into the ionosphere and at the altitude region of the upper hybrid resonance layer, the pump wave excites electrostatic waves at this altitude. These electrostatic waves parametrically decay into low frequency waves and electrostatic high frequency HF sidebands. The conversion from electromagnetic wave (pump wave) into electrostatic waves is called mode conversion and in this case it is called "direct conversion". Another mechanism that could also produce these electrostatic waves is the thermal oscillating two stream instability OTSI [*Dysthe et al. 1982; Lee and Kuo 1983; Huang and Kuo 1994*]. The crucial part in the direct conversion is the pre-existing short scale ($\sim$ 1m) field aligned density irregularities. Irregularities of a variety of scale sizes (varying over many orders of magnitude) exist in the different regions of the ionosphere. They arise from a number of sources such as wind, gravity, etc. The physical process of the direct conversion is as follows [Antani 1991]. The incident o-wave induces oscillating electron drift in the upper-hybrid resonance layer. This induced electron velocity mixes with the pre-existing density irregularities to generate a source current that plays the role of an in-situ antenna radiating the excited upper hybrid wave

$$J_s = -e\,\tilde{n}_{el}\,v_{eh} \tag{2.9}$$

where e is the electron charge, $\tilde{n}_{el}$ is the low frequency electrons density fluctuation and v_{eh} is the high frequency pump induced velocity (oscillating velocity) which is given by

$$v_{eh} = v_0 \;\; exp(i(k_x x - k_z z - \omega_0 t)) \tag{2.10}$$

The low frequency density irregularities produced by the parametric instability propagate in either the forward or backward direction.

The low frequency forward propagating density irregularities are given by

$$\delta^+_{ne} = \delta_{n0} \;\; exp(i(k_x x - \omega_l t)) + c.c. \tag{2.11}$$

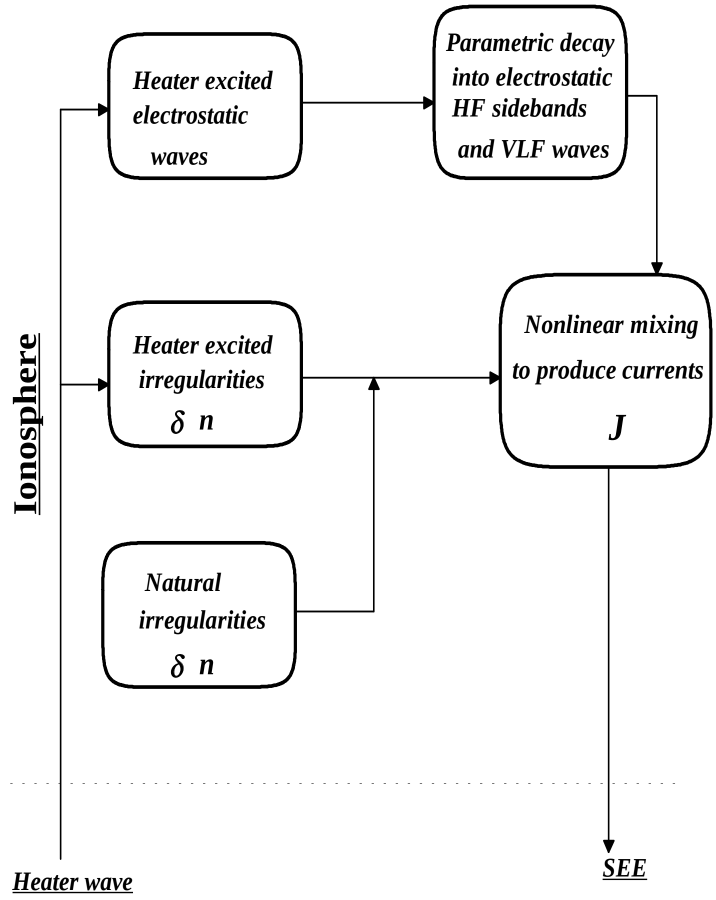

Figure 2.9: A physical model for the generation of SEE.

where *c.c.* denotes the complex conjugate.
These low frequency forward propagating density irregularities mix with the high frequency electron oscillations to produce a current responsible for producing the down-shifted frequency

$$J^{+} \simeq J_0 \ exp(i(-k_z z - (\omega_0 - \omega_l)t)) \tag{2.12}$$

The low frequency backwards propagating density irregularities are given by

$$\delta^{-}_{ne} = \delta_{n0} \ exp(i(k_x x + \omega_l t)) + c.c \tag{2.13}$$

These low frequency backwards propagating density irregularities mix with the high frequency electron oscillations to produce a backward propagating beat current which is responsible for producing the up-shifted frequency

$$J^{-} \simeq J_0 \ exp(i(-k_z z - (\omega_0 + \omega_l)t)) \tag{2.14}$$

These beat currents are responsible for the propagation of the up-shifted and the down-shifted frequencies seen on the ground as SEE. This process is called nonlinear scattering.

This process occurs whenever the following frequency and wave matching conditions are satisfied

$$\omega_0 = \omega_{uh} + \omega_n \tag{2.15}$$

$$k_0 = k_{uh} + k_n \tag{2.16}$$

where the subscripts "0" and "n" refer to the pump and the irregularities respectively. The direct conversion process differs from the parametric process in that it has no threshold field power requirement and also it leads to a linear growth that is linear in time. Note that since the direct conversion relies on these irregularities in the ionosphere, which vary with time and position, we can expect that the direct conversion process is not a static process but a process with high degree of fluctuations.

So, from the above discussion, the generation of SEE is through two steps the first and the most important step is the mode conversion "forward conversion", where the electromagnetic *O*-mode pump wave decays into electrostatic sidebands and low frequency decay mode at the altitude region of the upper hybrid resonance layer. The second step is the "backward conversion" from the electrostatic sideband waves into radiated electromagnetic waves radiated by the currents back to the ground as SEE. So, the reason for using a pure electrostatic model to study SEE is that we are looking at the electrostatic sidebands developed in the altitude region of upper hybrid resonance layer. In this region, most of the physical processes responsible for the generation of the SEE sidebands take place before it is scattered from the field aligned density irregularities and radiated to the ground through backward conversion and seen as SEE.

In essence of the above, we have chosen to use a purely electrostatic rather than a fully electromagnetic model to study SEE. It is also worth mentioning that a pure electrostatic model is computationally more feasible and consequently provides more resolution of the electrostatic parametric processes that produce SEE.

2.4.1 Cascading of electron waves

During ionospheric heating experiments, it was found that the down-shifted side bands can appear in a cascading or multiple structure. The mechanism is attributed to the fact that ω_0 might decay into electrostatic electron waves and low frequency ion waves. These electrostatic upper hybrid/electron Bernstein sidebands may act as a secondary pump that would in turn decay into a second sideband and thereby causing the multiple sideband feature. This mechanism is demonstrated in Figure (2.10).

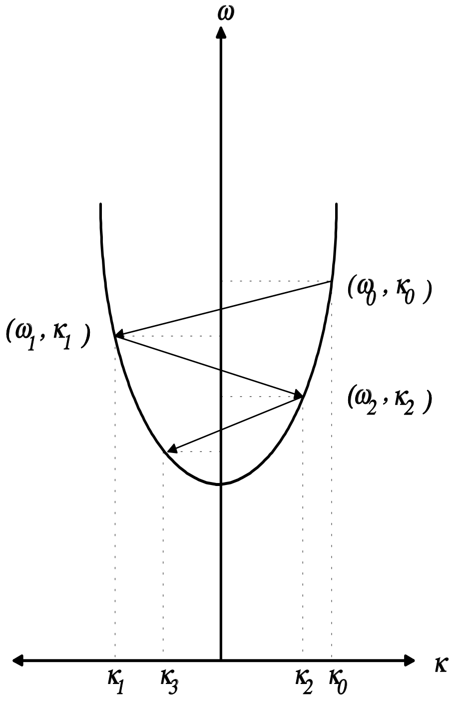

Figure 2.10: A schematic diagram showing the cascading of the electron waves.

Chapter 3

Theoretical Studies of Four-Wave Decay Instability

The fact that the BUM only appears at pump frequencies in the vicinity of the gyroharmonics suggests the involvement of the electron Bernstein waves [*Leyser et al.,* 1989, 1990]. Interactions capable of generating the BUM waves that satisfy the empirical relation $\omega_{\mathrm{BUM}} = 2\omega_0 - n\Omega_{\mathrm{ce}}$ generally involve what are referred to as a four-wave interaction [*Leyser et al.,* 1989, 1990, 1993; *Bud'ko and Vas'kov*, 1992; *Goodman et al.*, 1993; *Tripathi and Liu*, 1993; *Huang,* 1994; *Huang and Kuo*, 1994]. These interactions involve two pump photons or upper hybrid plasmons, a decay mode at $n\Omega_{\mathrm{ce}}$, and the stimulated radiation at ω_{BUM}. In the generation mechanism proposed by *Tripathi and Liu*, and of *Goodman*, the BUM radiation is the result of subsequent interactions between the UH and LH initial interaction decay products through a two-step process. *Huang and Kuo* [1994] pointed out that the difficulty of using the two-step process to explain the asymmetric feature of the BUM spectrum lies in the assumption used in their theory that the frequency-downshifted *O*-mode emissions produced in the second step of the scattering process must be strongly cyclotron damped. *Huang and Kuo* [1994] developed theoretical models for a four-wave second-order interaction process involving the decay of the pump wave into a frequency upshifted upper hybrid wave, a frequency downshifted electron Bernstein wave, and a driven low frequency oscillation near the lower hybrid wave. The excited frequency upshifted upper hybrid waves can then scatter off field-aligned density irregularities to generate *O*-mode emissions with frequencies around $2\omega_0 - n\Omega_{\mathrm{ce}}$. The concomitantly excited frequency downshifted electron Bernstein waves are found to have smaller amplitude, hence, their scattering products are also relatively weak. This proposed mechanism explains the asymmetry property between the frequency upshifted sideband and the downshifted sideband as a direct result of the theory. It also has successfully explained many of the important characteristics of the observed BUM feature in the SEE spectrum.

The purpose of this chapter is to study the behavior of the four-wave second-order process under various pump-wave parameters. Parameters that are varied include the pump powers, their frequencies, and propagation angles. Detailed discussion of the effects of varying these parameters will be provided along with the numerical simulation results in the next chapter.

3.1 Theoretical model

The wave-wave interaction process considered in the four-wave process is the parametric decay of the second harmonic oscillation $(2\omega_0, 2k_0 \approx 0))$ associated with a long wavelength electromagnetic pump wave $(\omega_0, k_0 \approx 0))$ in the plasma into a frequency downshifted electron Bernstein wave $(\omega_{\text{eB}}, k_{\text{eB}})$ and a frequency upshifted upper hybrid wave $(\omega_{\text{uh}}, k_{\text{uh}})$ (sideband) along with a nonlinear coupling induced lower hybrid oscillation $(\omega_{\text{lh}}, k_{\text{lh}})$. The presence of the second harmonic oscillation is inherent in the nonlinearity of the plasma medium. The wave number and frequency matching conditions for this parametric process are $k_{\text{eB}} + k_{\text{lh}} = 0$, $k_{\text{uh}} - k_{\text{lh}} = 0$, and $\omega_{\text{eB}} + \omega_{\text{lh}}^* = \omega_0 = \omega_{\text{uh}} - \omega_{\text{lh}}(2\omega_0 = \omega_{\text{lh}}^* + \omega_{\text{eB}})$, where the asterisk denotes the complex conjugate. In the coordinate system used for the present analysis, the wave vector $\bar{k}_{\text{lh}}$ points to the x direction (i.e., $\bar{k}_{\text{lh}} = \hat{x}k_{\text{lh}}$) and the background magnetic field to the $-z$ direction. Since an O-mode HF heater has been used in many SEE experiments, the heater wave is assumed to have a right hand circular polarization in the region away from the reflection height and is expressed to be

$$\bar{E}_{\text{p}} = (\hat{x} + i\hat{y})E_0 e^{-i\omega_0 t} + c.c.$$

Using the oscillating frame transformation [*Kuo and Cheo*, 1978] and the method of characteristics, the Vlasov equation is solved for δf_e. The result is integrated over the velocity space to obtain δn_e, the perturbed eletron density, which is then substituted into Poisson's equation to obtain the coupled mode equations for the two high frequency electrostatic waves and a low frequency oscillation in the frequency range of the lower hybrid wave. Considering the lower hybrid wave as a coupling product generated through the scattering of the HF heater wave off the excited high frequency electrostatic waves, those equations can be reorganized to derive the dispersion relation for the four-wave second-order process as given by [*Huang and Kuo*, 1994]

$$\begin{aligned}\epsilon_{\text{eB}}^*\epsilon_{\text{uh}} - \frac{\beta_e^4}{16}\Big\{\frac{1}{\epsilon_{\text{lh}}}[\chi_e(\omega_{\text{lh}}) - \chi_e(\omega_{\text{uh}})][\chi_e(\omega_{\text{lh}}) - \chi_e(-\omega_{\text{eB}}^*)] \\ +\frac{1}{2}[\chi_e(-\omega_{\text{eB}}^*) - 2\chi_e(\omega_{\text{lh}}) + \chi_e(\omega_{\text{uh}})]\Big\}^2 = 0,\end{aligned} \tag{3.1}$$

where $\epsilon_{\text{eB,uh}} = 1 + \chi_e(\omega_{\text{eB,uh}})$ and $\epsilon_{\text{lh}} = 1 + \chi_{\text{e}}(\omega_{\text{lh}}) + \chi_i(\omega_{\text{lh}})$. The susceptibility of the jth ($j = e$ or i) species χ_j is given by

$$\chi_j(\omega, k) = \frac{1}{k^2 \lambda_{\text{Dj}}^2} \left\{ 1 + \zeta_{j0} \sum_{n=-\infty}^{\infty} \Gamma_n(b_j) Z(\zeta_{\text{j}n}) \right\}, \tag{3.2}$$

where $\beta_e = 2kv_{\text{osc}}/(\omega_0 + \Omega_{\text{ce}})$, $v_{\text{osc}} = qE_0/m_e\omega_0$ is the electron oscillating velocity, k is the wave number, m_e is the electron mass, E_0 is the pump electric field strength, q is the electron charge, $b_j = k_\perp^2 \rho_j^2/2$, ρ_j is the cyclotron radius, $\zeta_{\text{j}n} = (\omega - n\Omega_{\text{cj}})/k_\parallel v_{\text{tj}}$, Ω_{cj} is the cyclotron frequency, v_{tj} is the thermal velocity, $\Gamma_n(b_j) = I_n(b_j)\exp(-b_j)$, Z is the Fried Conte function, I_n is the modified Bessel function of the first kind of order n, λ_{Dj} is the Debye length, and $k_\parallel(k_\perp)$ is the component of k parallel (perpendicular) to B.

3.2 Solution around the fourth cyclotron harmonic

The method of *Rönnmark* [1983] is used to calculate the plasma electron and ion susceptibilities in equation (3.2) as well as the derivatives of these susceptibilities. A Newton Raphson method is then used to find the root for equation (3.1). We have used the artificial ion-electron mass ratio $m_i/m_e = 400$ for both the theoretical calculations here and the numerical simulations in Chapter 4. This reduced m_i/m_e allows the numerical simulation model to be more computationally efficient. Caution has been taken to choose an appropriate value so that qualitative changes will not be introduced into the physical processes under investigation. Specifically, the chosen value is still large enough to provide sufficient frequency separations between the electron and ion plasma frequencies $\omega_{\text{pe}}, \omega_{\text{pi}}$, their respective cyclotron frequencies $\Omega_{\text{pe}}, \Omega_{\text{pi}}$, and a visible frequency separation between the pump frequency and the sidebands. In Section 3.7 we will show that comparisons with the theoretical calculations with the real mass ratio $m_i/m_e = 29,362$ have found that the reduced value does not qualitatively change the angular range and the wave number range over which the four-wave process develops. The oscillation velocity to electron thermal velocity ratio is $v_{\text{osc}}/v_{\text{te}} = 0.35$. This value is larger than its experimental counterpart that is typically of the order of 10^{-2}, and it improves the computational efficiency in the numerical simulation model while not qualitatively altering important processes. The dispersion relation has been solved for a wide range of parameters. We first describe a calculation for the case where the pump frequency is above the fourth cyclotron harmonic $4\Omega_{\text{ce}} < \omega_0 < \omega_{\text{uh}}$. This case has been studied in a number of past experiments. The frequency offset $\Delta\omega_0 = \omega_0 - 4\Omega_{\text{ce}}$ is taken to be $3\omega_{\text{lh}}$, where ω_{lh} denotes the lower hybrid resonance frequency. According to the frequency matching conditions the upper hybrid wave frequency is given by $\omega_{\text{uh}} = 4\Omega_{\text{ce}} + 6\omega_{\text{lh}}$. Figure (3.1) shows the dispersion relation for the electron Bernstein and upper hybrid waves and the location of pump frequency ω_0. Note that ω_0 is chosen to be about the mean of the electron Bernstein wave frequency and the upper hybrid wave frequency, as predicted by *Huang and Kuo* [1994]. For given values of ω_0 and $\omega_{\rm uh}$, the dispersion relation in equation (3.1) is solved to obtain the propagation angle with respect to the direction perpendicular to the magnetic field B for the maximum growth $\theta_{\max}$. In this case, the angle is found to be $\theta_{\max} \simeq 3.0\sqrt{m_e/m_i}$. The growth rate γ at $\theta_{\max}$ is calculated and plotted versus wave number $k_\perp\rho_e$. The result in Figure (3.1) shows the wavelength range for the four-wave process. The maximum growth occurs for $k_\perp\rho_e \simeq 0.3$, where $\gamma/\omega_{\rm lh} \simeq 0.01$.

A number of dispersion calculations have been performed to examine the effects of plasma and pump wave parameters on the development of the four-wave decay process. The result of those calculations is presented in term of the growth rate γ of the instability, the most important indicator of the strength of the BUM. Generally, a larger growth rate indicates that the BUM peak will be higher and the range of the BUM spectrum will be broader.

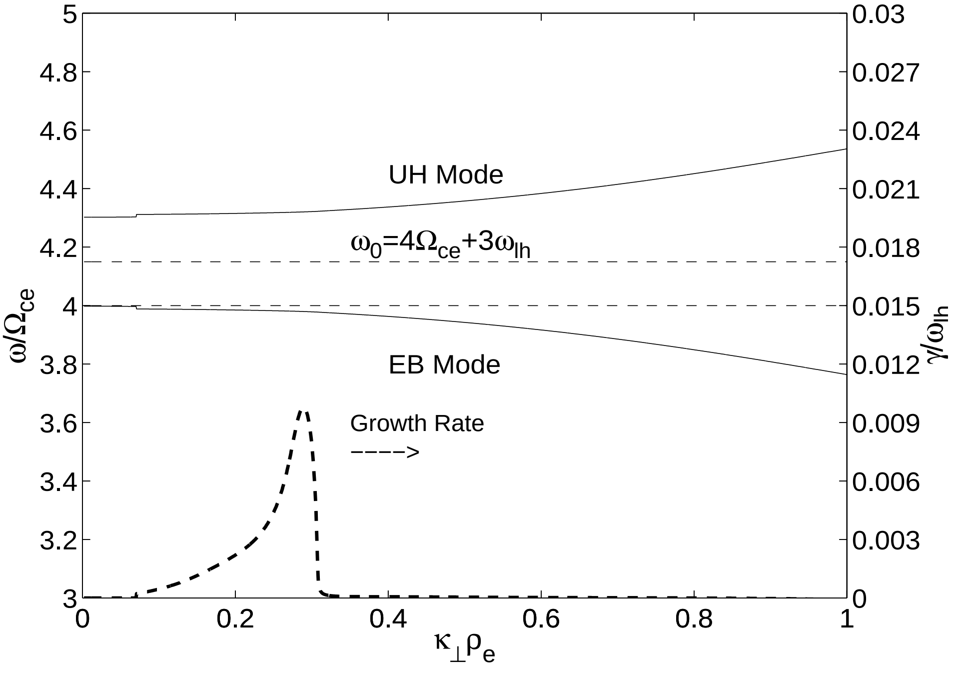

Figure 3.1: Plot for the growth rate γ in equation (3.1) versus wavelength $k_\perp\rho_e$ and the dispersion relation for the upper hybrid (UH) and the electron Bernstein (EB) modes for the case $\omega_0 = 4\Omega_{\rm ce} + 3\omega_{\rm lh}$, $\theta{\approx}3.0\sqrt{m_e/m_i}$ and $v_{\rm osc}/v_{\rm te} = 0.35$.

3.3 Effects of varying the cyclotron harmonic number

The first group of calculations considers the effects of changing the cyclotron harmonic number. The result in Figure (3.2) shows the growth rate γ versus the propagation angle θ for the cases $\omega_0 = n\Omega_{\text{ce}} + 3\omega_{\text{lh}}$, where $n = 3, 4, 5, 6, 7$ and $\Delta\omega_0 = 3\omega_{\text{lh}}$. It can be seen that the growth rate increases with the harmonic number, accompanied by a reduction in the angle of maximum growth toward propagation perpendicular to the magnetic field. Notice that the maximum growth rate $\gamma_{\max}$ occurs when $\theta \simeq 3.0\sqrt{m_e/m_i}$ for all the cases calculated here. For the real mass ratio $m_i/m_e = 29,362$, this implies that we can achieve the maximum growth rate when $\theta \approx 1°$. The relation between the harmonic number and the maximum growth rate is approximately linear as shown in Figure (3.3) for $v_{\text{osc}}/v_{\text{te}} = 0.35$.

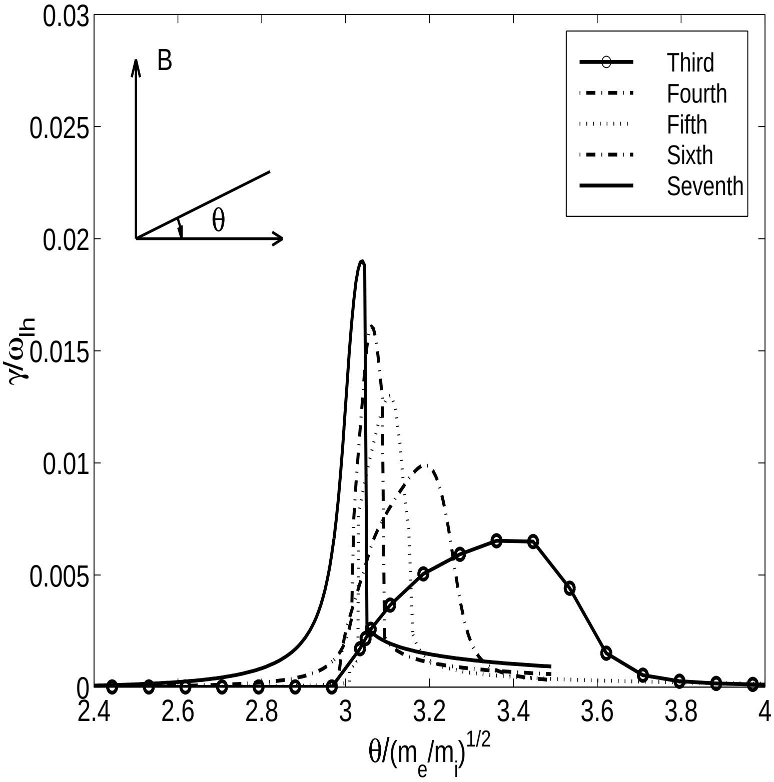

Figure 3.2: Growth rate γ versus θ for the cases $\omega_0 = n\Omega_{\text{ce}} + 3\omega_{\text{lh}}$ (n = 3, 4, 5, 6, 7) and $v_{\text{osc}}/v_{\text{te}} = 0.35$. Here γ is the maximum growth rate for each θ.

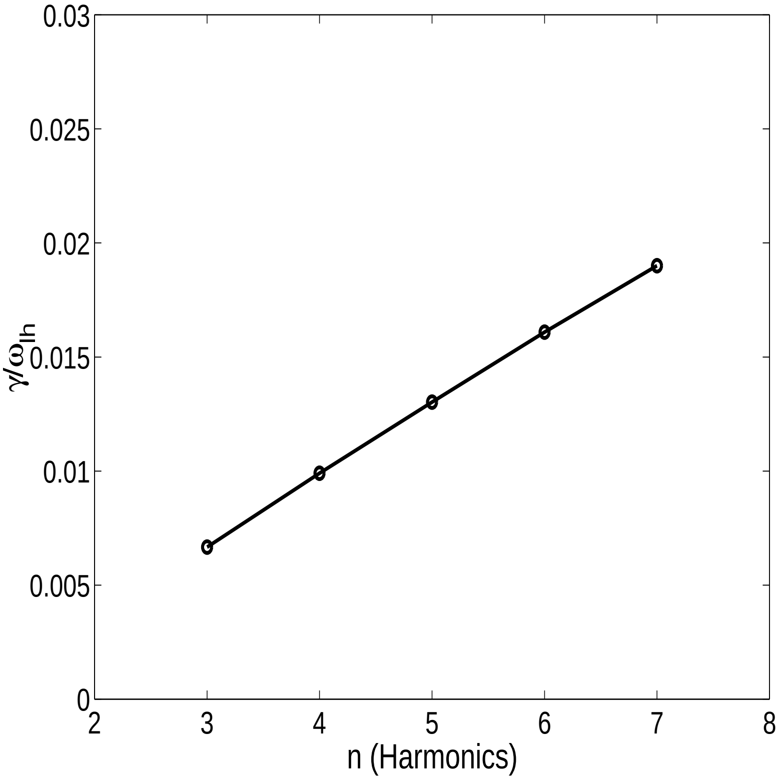

Figure 3.3: Dependence of γ on the harmonic number n for the cases $\omega_0 = n\Omega_{\rm ce}+3\omega_{\rm lh}$; γ is obtained for each n at a specific propagation angle θ.

3.4 Effects of varying the frequency offset

The effects of varying the frequency offset $\Delta\omega_0 = \omega_0 - n\Omega_{\rm ce}$ are very important in that past SEE experiment observations when stepping the pump frequency have shown the behavior of the BUM spectrum is sensitive to the change of pump frequency around the cyclotron harmonic frequency. It is indicated in Figure (3.4) that increases in the frequency offset $\Delta\omega_0$ lead to decreases in the maximum growth rate . Figure (3.5) shows the same trend where both the frequency offset and the harmonic number are varied. Also noted in Figure (3.4) is that the angle of maximum growth rate moves away from the direction perpendicular to the magnetic field when increasing the frequency offset $\Delta\omega_0$.

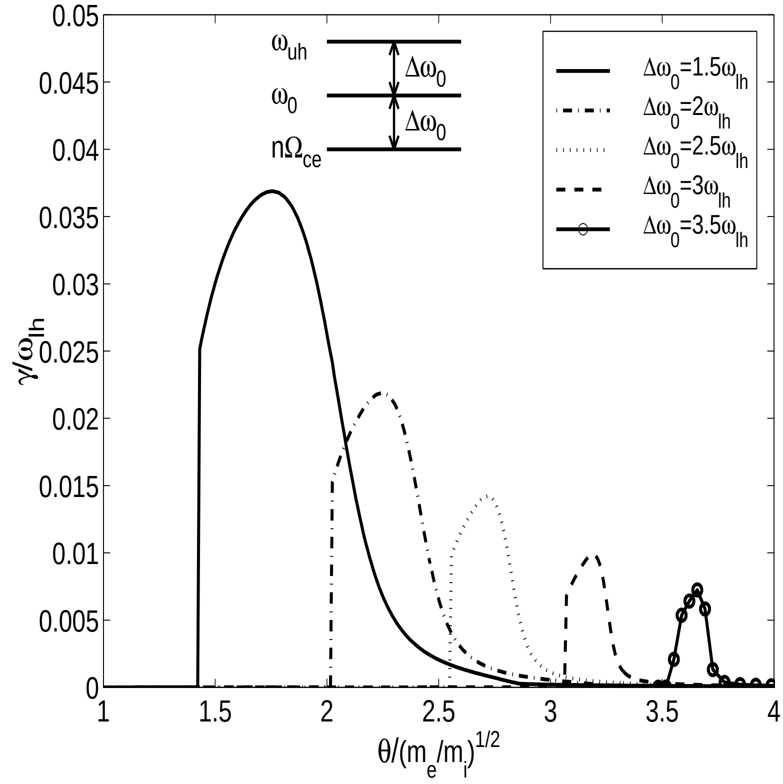

Figure 3.4: Growth rate γ versus θ for the cases $\omega_0 = 4\Omega_{\rm ce} + m\omega_{\rm lh}$ (m $= 1.5, 2, 2.5, 3, 3.5$) and $v_{\rm osc}/v_{\rm te} = 0.35$.

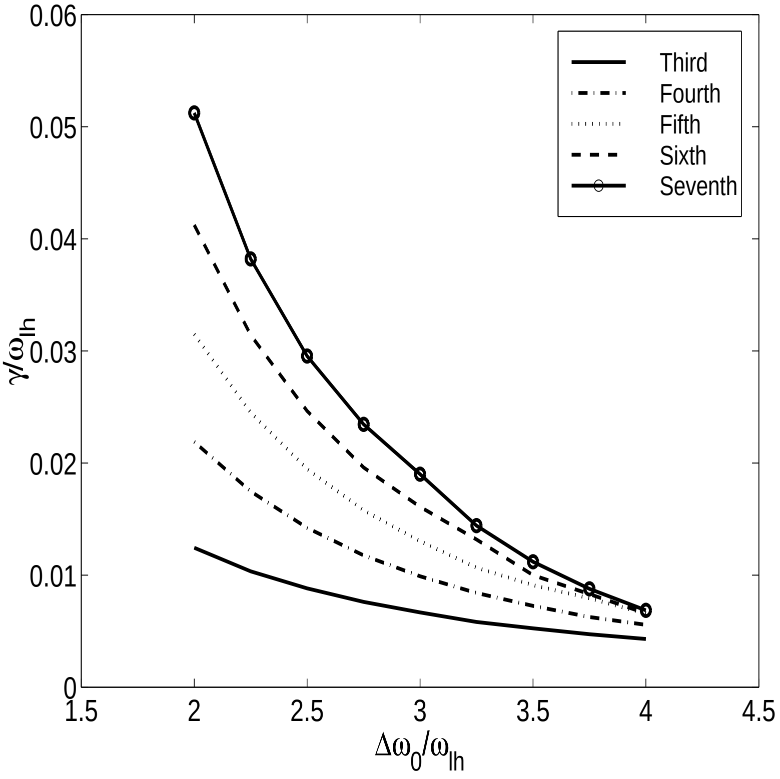

Figure 3.5: Growth rate γ versus frequency offset for the cases $\omega_0 = n\Omega_{\rm ce} + m\omega_{\rm lh}$ (n = 3, 4, 5, 6, 7 and m = 2, 2.5, 3, 3.5, 4) and $v_{\rm osc}/v_{\rm te} = 0.35$; γ is obtained for each case at a specific propagation angle θ.

3.5 Effects of varying the pump amplitude

Past experiments [*Wagner et al.*, 1999] also indicated that the BUM spectrum is closely related to the pump power. Figure (3.6) shows that increasing the pump amplitude causes an increase in the growth, while the wavelength range is essentially unchanged. The values of the amplitude in Figure (3.6) are chosen so that the difference between adjunct pump power levels is 3 dB.

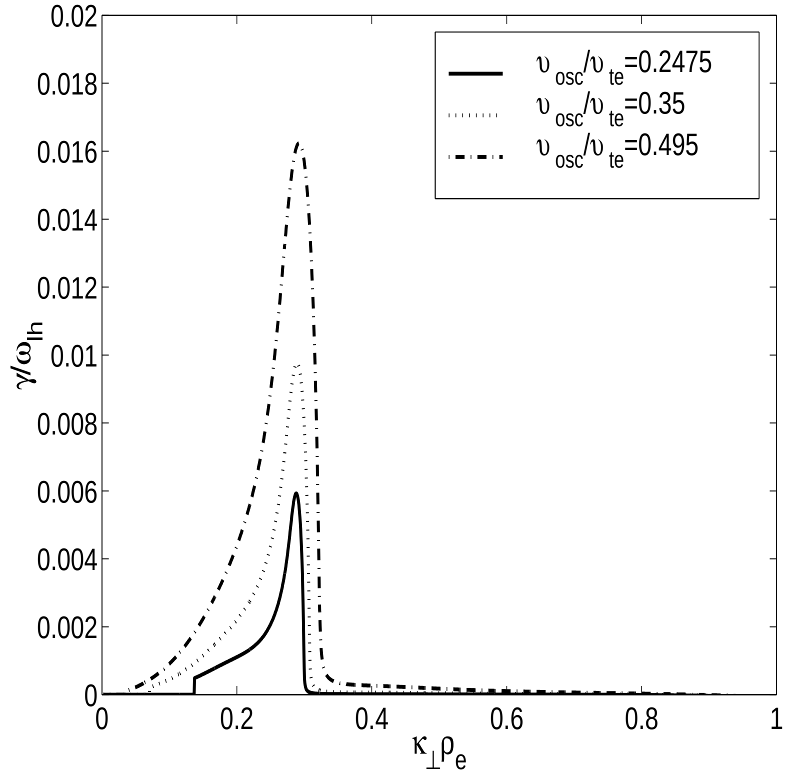

Figure 3.6: Growth rate γ versus pump amplitude for the cases $\omega_0 = 4\Omega_{\rm ce} + 3\omega_{\rm lh}$ and $v_{\rm osc}/v_{\rm te} = 0.2475$, 0.35, 0.495. Here $T_e = T_i$ and $v_{\rm te} = \text{const}$.

3.6 Effects of varying the temperature ratio $T_{\rm e}/T_{\rm i}$

The effect of the temperature ratio T_e/T_i on the four-wave process is of particular importance in the explanation of the asymmetry property between the frequency upshifted sideband and the downshifted sideband. In the theoretical calculations of

Figure (3.7), it is observed that $\gamma_{\max}$ decreases as we increase T_e/T_i. In the next chapter, we will discuss how this observation helps us understand the development of the four-wave decay after saturation because T_e/T_i is increased substantially at that time.

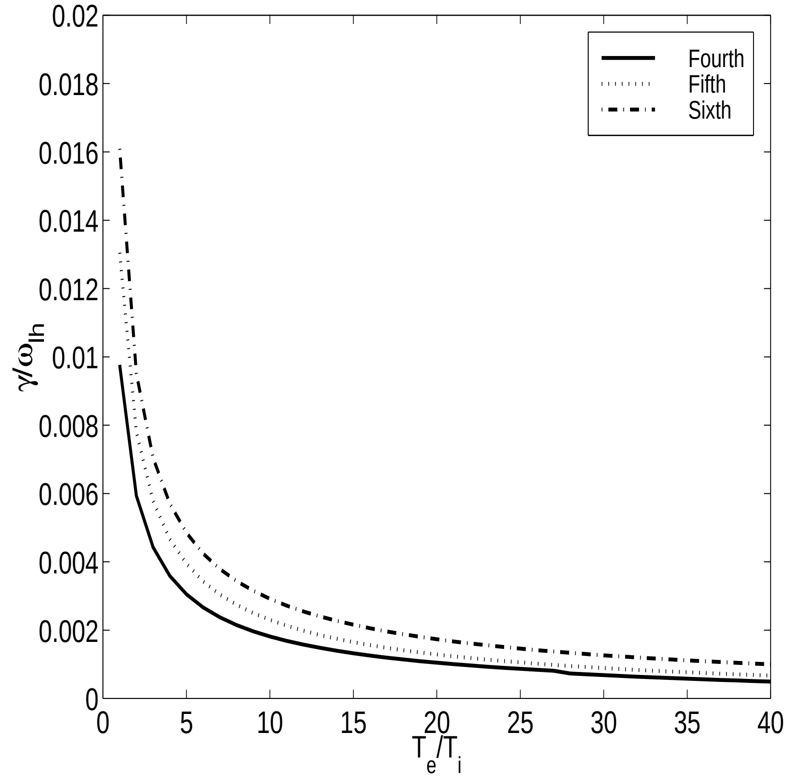

Figure 3.7: Dependence of growth rate γ on temperature ratio T_e/T_i for the cases $\omega_0 = n\Omega_{\mathrm{ce}} + 3\omega_{\mathrm{lh}}$ and $v_{\mathrm{osc}}/v_{\mathrm{te}} = 0.35$ for $n = 3, 4, 5$.

3.7 Effects of varying the mass ratio $M_{\mathrm{i}}/M_{\mathrm{e}}$

In this research we use a mass ratio $M_{\mathrm{i}}/M_{\mathrm{e}}$=400 for the theoretical calculations and numerical simulations. The reduced mass ratio enables us to run simulations more efficiently. Still a typical run on a DEC AlphaStation 600 with $M_{\mathrm{i}}/M_{\mathrm{e}}$=400 takes around 3 days to get enough resolution of frequency spectra as well as a full development of the nonlinear process. A simulation with $M_{\mathrm{i}}/M_{\mathrm{e}}$=29,362 would have taken weeks. In Figure (3.8) the angular regions for the growth rate are shown for the cases of $M_{\mathrm{i}}/M_{\mathrm{e}}$=400 and 29,362. It can be seen that with a reduced mass ratio the growth rate is much larger. However, the angular region, an indication of how

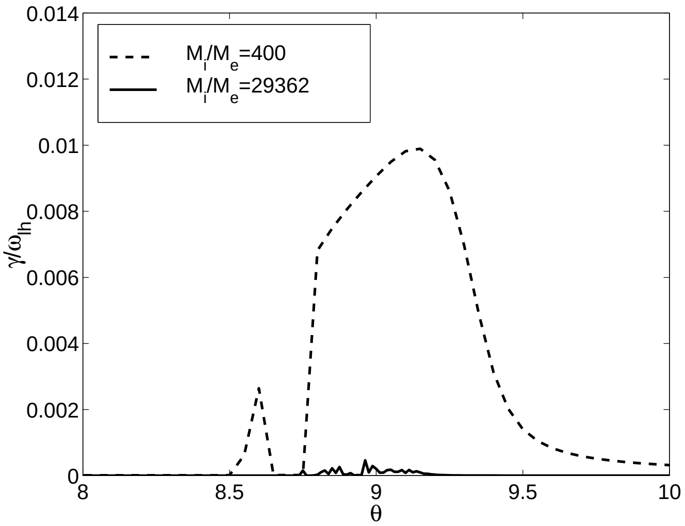

Figure 3.8: Angular regions for the growth rate for the cases of $M_{\mathrm{i}}/M_{\mathrm{e}}$=400 and 29,362.

broad the instability will develop, stays almost the same. Figure (3.9) shows that the wavenumber region does not change very much when the mass ratio is varied.

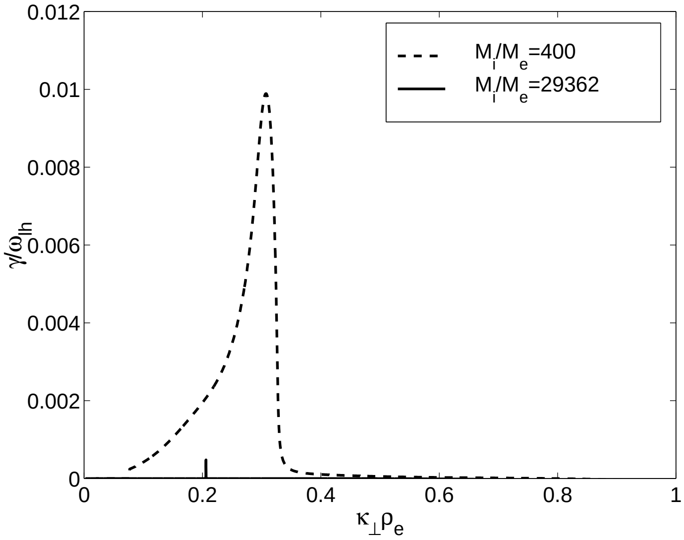

Figure 3.9: Wavenumber regions for the growth rate for the cases of $M_{\mathrm{i}}/M_{\mathrm{e}}$=400 and 29,362.

Chapter 4

Numerical Studies of Four-Wave Decay Instability

The four-wave decay instability model described in the previous chapter has been successful in interpreting some characteristics of the BUM spectrum in term of the growth rate of the instability. However, as this model is essentially based on linearization up to the second-order terms, we cannot predict how the instability will grow, when it will saturate, and how it will behave after saturation. When we deal with complicated processes such as SEE, a number of nonlinear physics processes occur inside an inhomogeneous plasma. It is impossible to derive the end results that describe the system analytically without sacrificing the nonlinear details. On the other hand, a numerical simulation, when conducted properly, provides much more details in the plasma, such as the phase space of a species at a particular time instance. It also offers unlimited flexibility to change plasma and wave parameters to do numerical experiments. Such flexibility is very important given the richness of past SEE experiment configurations. Although numerical simulations may ultimately provide important contributions to the understanding of nonlinear processes and bridge the gap between theoretical development and experimental observations, there have been few studies in the past [*Goodman et al.*, 1994; *Scales et al.*, 1997; *Hussein and Scales*, 1997; *Hussein et al.*, 1998]. The purpose of this chapter is to use various numerical experiments to investigate the full development of the four-wave decay instability that is proposed as a viable mechanism for the generation of the BUM. Our emphasis will be placed on interpreting the behavior of the BUM spectral features after saturation and for a wide range of plasma and pump wave parameters. In particular we will investigate the effects of varying the harmonic number and the frequency offset $\Delta\omega_0 = \omega_0 - n\Omega_{\mathrm{ce}}$, which have been the subject of intensive investigation during past SEE experiments.

4.1 Simulation model

A periodic one space dimension and three velocity dimension (1D3V) electrostatic particle-in-cell (PIC) simulation model using standard techniques [*Birdsall and Langdon*, 1991] is used to investigate the nonlinear evolution of the four-wave decay instability. The model has three velocity dimensions that allow for the propagation of lower hybrid waves as well as electron Bernstein and upper hybrid waves. The model geometry is shown in Figure (4.1). An external uniform oscillating electric field E with amplitude given by $E = E_0 \cos(\omega_0 t)$ is used to represent the long-wavelength pump wave and is applied uniformly across the simulation box. The system length is $1024\lambda_{\mathrm{D}}$, where λ_{D} is the initial electron Deybe length, with a uniform density of 400 particles per grid cell for each species. The total number of particles in the simulation is 819,200. The grid cell size is equal to λ_{D}. As was stated earlier, $m_i/m_e = 400$ and $v_{\mathrm{osc}}/v_{\mathrm{te}} = 0.35$. The electrons and ions initially have Maxwellian velocity distributions with $T_e = T_i$. The angle of propagation $\theta_{\max}$ described in the previous section is used for the simulation. The simulation usually runs for up to 1.8×10^6 time steps corresponding to the early stages (up to a few tenths of seconds) in the SEE experiments. The system length of $1024\lambda_{\mathrm{D}}$ corresponds to a system length of the order of tens of meters in the F region where λ_{D} is of the order of 1 cm. We assume that the heated electrons do not have the time to travel out of the turbulence layer during the simulation time. Therefore a periodic boundary condition is used here. The early time behavior of the four-wave process in a small area of the F region is our primary consideration in the numerical simulations.

Several diagnostics are used to analyze the development of the four-wave process. The most important is the simulation electric field power spectrum $|E(\omega)|^2$. The PIC simulations solve for the electric field $E(x,t)$ which varies in both time and space. To calculate the spectrum, we consider a number of fixed spatial points in the simulation box. The corresponding time series of the simulation electric field at each point is then used to calculate the frequency spectrum. This spectrum is calculated by taking a fast Fourier transform of the time series and forming the magnitude squared. The spectra at several different spatial points are averaged together to reduce the noise level.

4.2 Temporal behavior of the four-vave instability

The important result of a typical simulation run of the numerical model is shown in Figures (4.2-4.8). Figure (4.2a) shows the temporal evolution of the maximum amplitude of the electron Bernstein and upper hybrid waves during the simulation for the case of $\omega_{\mathrm{uh}} = 4\Omega_{\mathrm{ce}} + 6\omega_{\mathrm{lh}}$ and $\omega_0 = 4\Omega_{\mathrm{ce}} + 3\omega_{\mathrm{lh}}$ ($\Delta\omega_0 = 3\omega_{\mathrm{lh}}$). The simulation

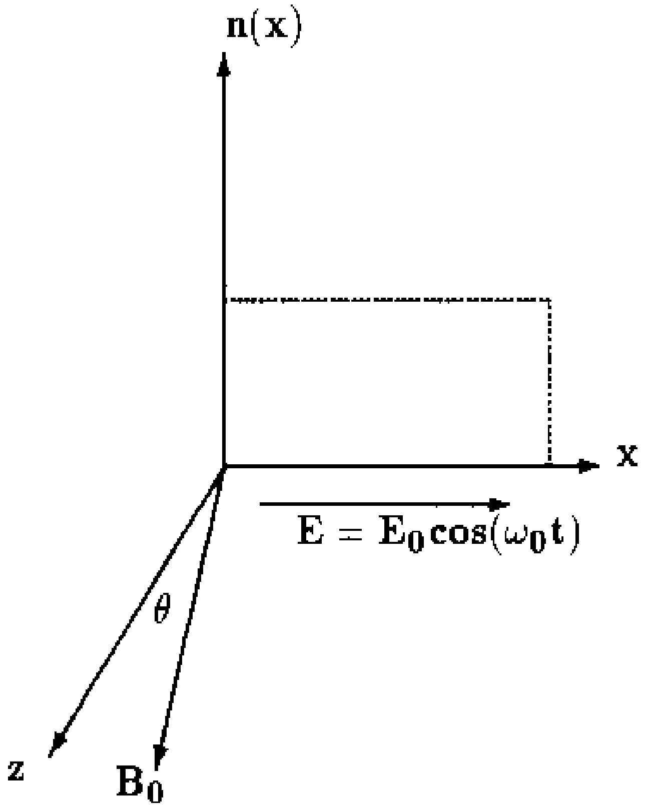

Figure 4.1: Schematic 1D3V particle-in-cell model for studying the four-wave process around electron gyroharmonic frequencies $n\Omega_{\rm ce}$.

runs for up to 1.2×10^6 time steps corresponding to an end time $\omega_{\mathrm{lh}}t = 3000$ and roughly four growth periods of the four-wave interaction process to allow for a steady state to take place and sufficient frequency resolution. The pump wave is turned on at time $\omega_{\mathrm{lh}}t = 300$ to observe the growth of the four-wave instability above the simulation thermal noise level. It is observed that after the pump field is turned on, the electron Bernstein and upper hybrid waves grow exponentially at essentially the same rate during the time period $300 < \omega_{\mathrm{lh}}t < 650$. A calculation of the simulation growth rate during this period has shown a quite good agreement with the theoretical prediction in Figure (3.1). It has been shown that the wavelength of these waves typically agrees with the theoretical predictions as well by using an interferogram calculation [*Hussein et al.*, 1998]. After time $\omega_{\mathrm{lh}}t \simeq 650$, the growth of the waves saturates. It can be seen that after saturation, the amplitude of the upper hybrid wave is nearly constant following an initial overshooting. This overshooting on millisecond timescales is consistent with previous experimental observations [*Sergeev et al.*, 1997]. The electron Bernstein wave behavior has an important difference in that the amplitude of this wave decays significantly after saturation. Near the end of the simulation, the electron Bernstein wave has an amplitude that is 10-15 dB below the upper hybrid wave. Figure (4.2b) shows that there is significant electron wave-particle heating along the magnetic field associated with the four-wave instability, while the ion heating is negligible. The electron heating saturates at nearly the same time as the upper hybrid and electron Bernstein wave amplitudes. It is important to note that the degree of electron temperature increase in our simulation is not meant to be directly compared with the bulk temperature increases observed during heating experiments where the measurements indicate maximum increases of about 30% in T_e [*Honary et al.*, 1995; *Robinson et al.*, 1996]. The numerical simulations use an enhanced value of oscillation velocity and a reduced ion-electron mass ratio and consider a small spatial region to be computationally feasible. However, the numerical simulations clearly show the importance of the effects of the wave-particle heating by the four-wave process on the ultimate asymmetry in the spectrum after nonlinear saturation, as will be discussed shortly. Also, our simulations use periodic boundary conditions which elevate the temperature somewhat. Semi-open boundary conditions may be used in which a small fraction of hot electrons that escape the simulation box are replaced by electrons from the cool background distribution [*Wang et al.*, 1997]. We find that this type of boundary condition reduces the saturated electron kinetic energy only by roughly 50% and does not qualitatively change the characteristics of the saturated spectra in our present simulations. Therefore we believe that periodic boundary conditions are reasonable for our intents and purposes here.

The time evolution of the simulation electric field power spectrum is shown in Figure (4.3). The low-frequency spectrum shows the evolution of the lower hybrid wave, and the high-frequency spectrum shows that of the electron Bernstein and upper hybrid waves. The first time period ($0 < \omega_{\mathrm{lh}}t < 300$) corresponds to the time before the pump field is turned on and shows the simulation noise level. The period

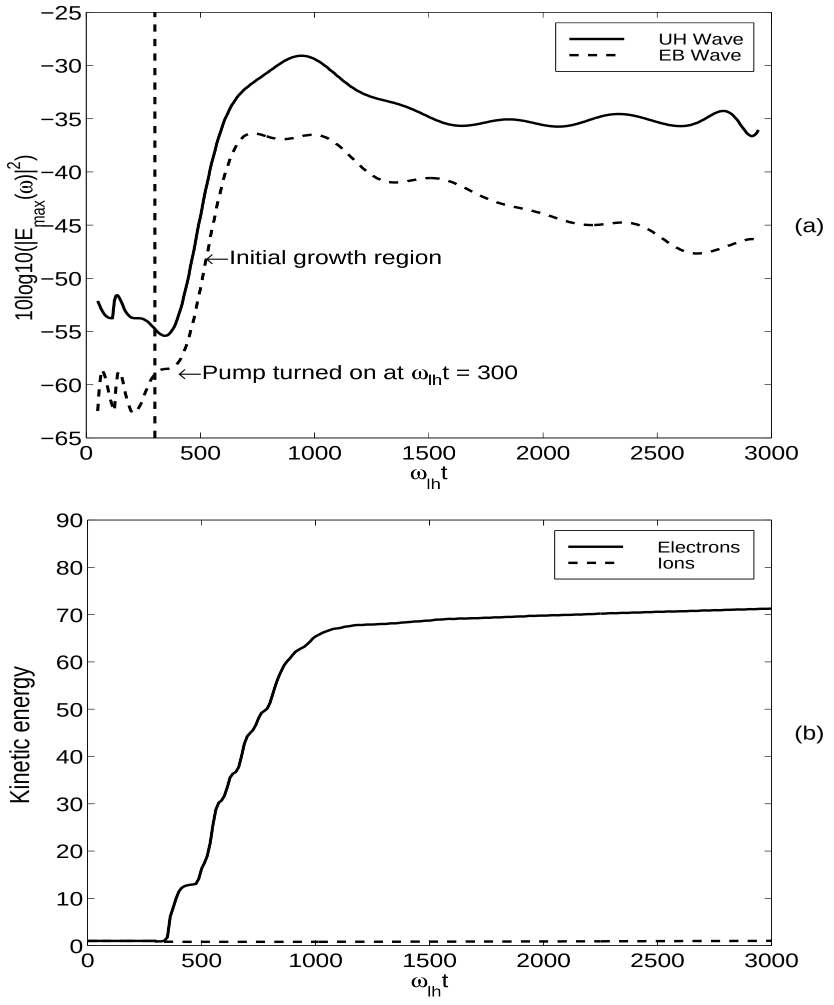

Figure 4.2: Results showing the time evolution of the peak amplitude of both the upper hybrid and electron Bernstein waves and the kinetic energy history for $\omega_0 = 4\Omega_{\mathrm{ce}} + 3\omega_{\mathrm{lh}}$ and $v_{\mathrm{osc}}/v_{\mathrm{te}} = 0.35$. Note that the electron Bernstein wave damps after saturation and the electron heating saturates near the same time as the sidebands.

$350 < \omega_{\mathrm{lh}} t < 650$ shows the spectrum during the exponential growth region where we notice that the electron Bernstein and upper hybrid waves grow at roughly the same rate and have comparable amplitudes. The upper hybrid wave exhibits a broader bandwidth owing to the difference in dispersion characteristics of the two waves, as can be seen in Figure (3.1). The period $750 < \omega_{\mathrm{lh}} < 1050$ shows the spectra near the time of maximum amplitudes. The final period $1500 < \omega_{\mathrm{lh}} t < 2500$ shows the spectrum after saturation which is most relevant to experimental observations. It can be clearly seen that the electron Bernstein wave amplitude has been significantly damped. The spectrum exhibits the asymmetric upshifted structure as is observed in the experimental observations of the BUM. It should be noted that the damped electron Bernstein wave produces a weak downshifted sideband that is reminiscent of the BDM [*Stubbe et al.*, 1984] often observed in the experiments. It should be noted that the BDM has been observed in recent SEE experiments [*Wagner et al.,* 1999] as well.

The result in Figure (4.3) also shows the frequency up-shifted upper hybrid, frequency down-shifted electron Bernstein, and the low frequency lower hybrid waves. Figure (4.3) indicates that the frequency matching condition is satisfied. In order to check the wavenumber matching conditions, an interferogram is constructed in which we compute

$$E_{\mathrm{x}}(x,\tau) = \frac{1}{T}\int_0^T \sin(\omega_{\mathrm{d}} t) E_{\mathrm{x}}(x, t+\tau)\ dt \tag{4.1}$$

where ω_{d} is either the up-shifted, down-shifted or the low frequency wave frequencies. The result in Figure (4.4) shows that the wavelength of both the up-shifted and down-shifted sidebands are comparable to that of the low frequency wave which shows good agreement with the theoretical prediction.

Figure (4.5) shows the electron phase space plots over the development of the four-wave process. Before the pump is turned on, the electrons are concentrated around zero velocity with small fluctuations due to thermal noises. As time goes on, they are heated substantially along the magnetic field.

The time evolution of the parallel and perpendicular (to the magnetic field) electron velocity distribution functions is also shown in Figure (4.6). It can be seen that the four-wave instability heats the electrons primarily in the direction perpendicular to the magnetic field. There is some tail heating observed in the parallel velocity distribution as well. It should be noted that significant perpendicular heating near the upper hybrid layer for pump frequencies near cyclotron harmonics has been predicted by *Grach* [1999]. This is important in that this type of anisotropic velocity distribution may be capable of being unstable to upper hybrid waves [*Zheleznyakov and Zlotnik*, 1975] which could be another source mechanism for the BUM as well [*Grach*, 1999]. This is an important issue that will require additional investigation.

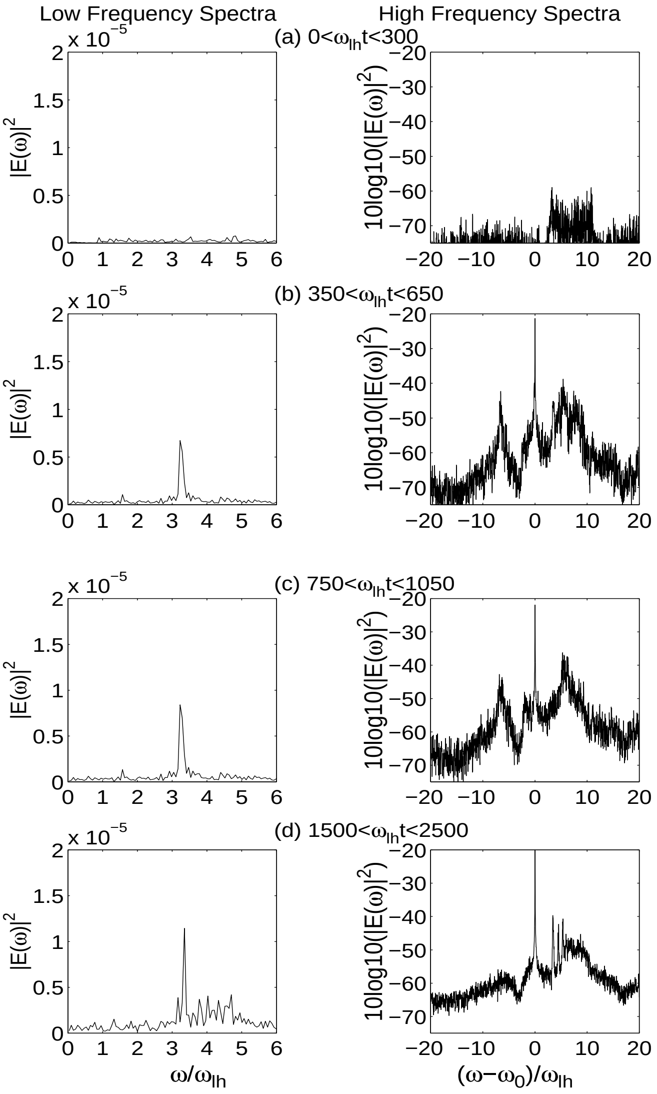

Figure 4.3: Simulation result showing the temporal evolution of high-frequency spectra (showing the UH and EB waves) and low-frequency spectra (showing the LH waves). Note the growing and damping processes of the downshifted sidebands that lead to the asymmetric spectrum.

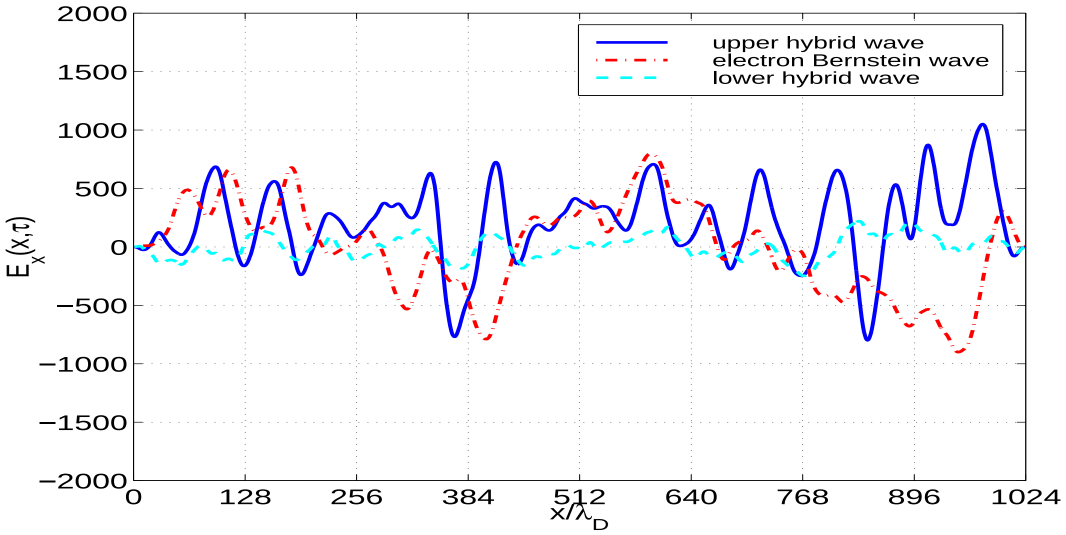

Figure 4.4: An interferogram verifying the wavenumber matching for the four-wave interaction process in the interval $500 < \omega_{\mathrm{lh}} t < 505$.

Figure (4.7) shows the time evolution of the electron density deviation from the background plasma during the four-wave process. After the pump is turned on at time $\omega_{\mathrm{lh}} t = 300$, cavities start to appear, and they tend to reappear at the same locations periodically while becoming broader and shallower over time. Note that the cavities appear as the black regions in Figure (4.7). Finally, they vanish after the electron Bernstein and upper hybrid wave amplitudes saturate. The physical mechanism for the generation of these cavities requires significant further investigation and is beyond the scope and intent of our present study. It should be noted that electron density cavities with similar spatial and temporal characteristics were observed in numerical Vlasov model simulations used to investigate early time Langmuir turbulence behavior during ionospheric modification experiments [*Wang et al.*, 1997].

A large number of numerical simulations have been run to consider the effects of harmonic number as well as frequency offset $\Delta\omega_0$. The growth rate calculations based on the theoretical model are used to guide the simulation runs. These simulations show the same qualitative behavior in terms of temporal evolution and saturated frequency spectral characteristics.

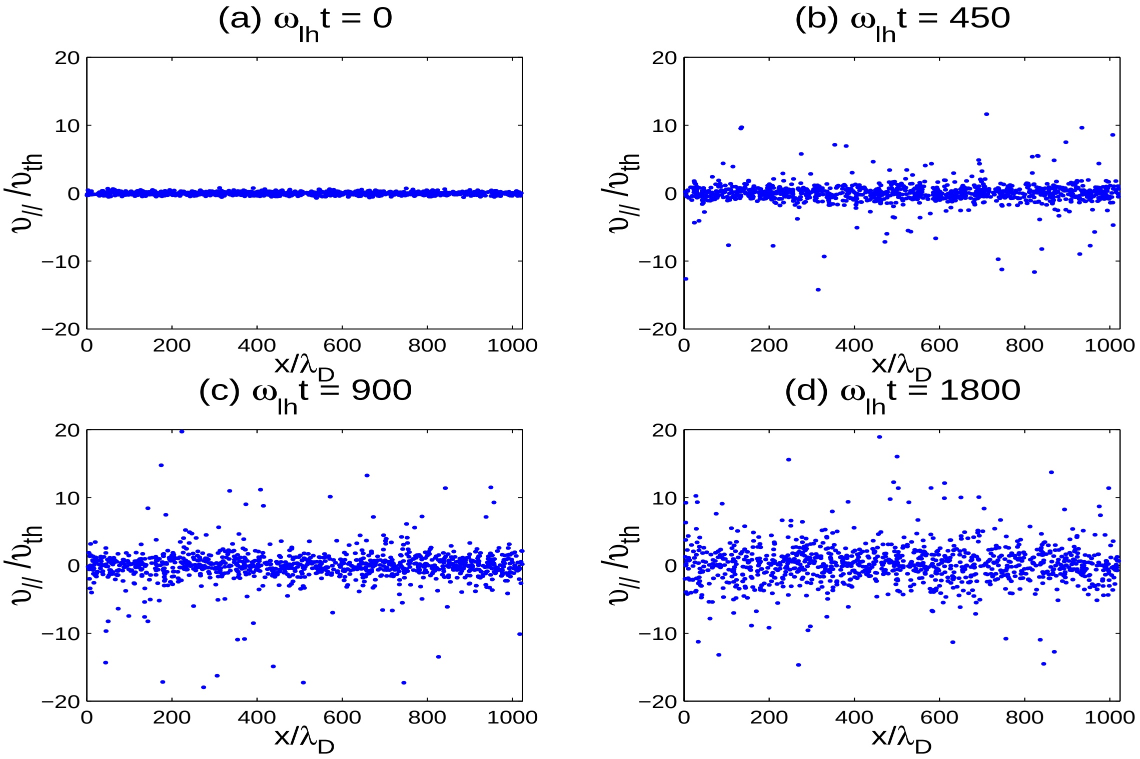

Figure 4.5: Electron phase space plots showing the electron heating along the magnetic field over time for $\omega_0 = 4\Omega_{\rm ce} + 3\omega_{\rm lh}$ and $\upsilon_{\rm osc}/\upsilon_{\rm te} = 0.35$.

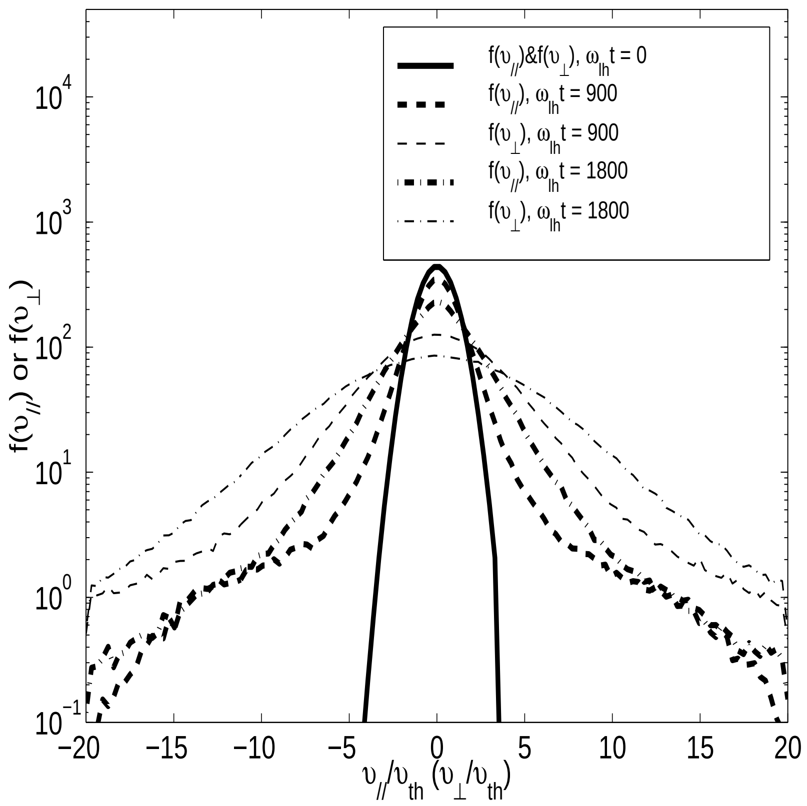

Figure 4.6: Simulation result showing the change of the electron velocity distribution functions across and along the magneticfield over time due to wave-particle heating. At $\omega_{\rm lh}t = 0$, both velocity distribution functions are the same. Note that the electrons are primarily heated in the direction perpendicular to the magnetic field.

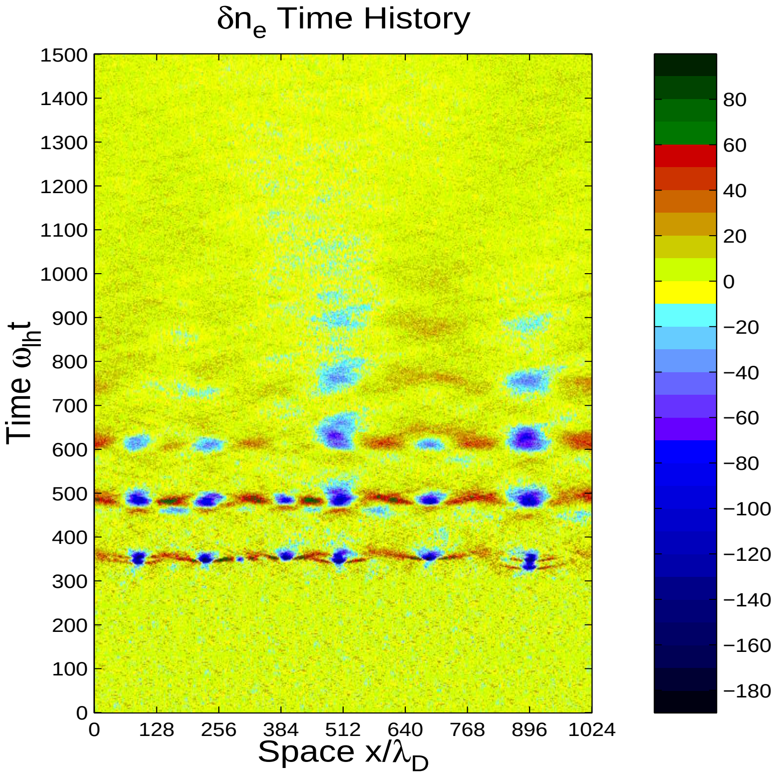

Figure 4.7: Time history of the electron density perturbation. After the pump is turned on at time $\omega_{\text{lh}} t = 300$, cavities start to appear, and they tend to reappear at the same locations periodically while becoming broader and shallower over time.

4.3 Effects of varying the pump frequency: $\omega_0 = 4\Omega_{\rm ce} + m\,\omega_{\rm lh}$, $v_{\rm osc}/v_{\rm te} = 0.35$

The behaviors of the SEE spectrum with varying pump frequency have been studied extensively during the past SEE experiments [*Leyser et al.*, 1989; *Stubbe et al.*, 1994; *Frolov et al.*, 1996, 1997]. Here we present numerical results showing how the pump frequency affects the growth period and the nonlinear saturation period of the four-wave decay process.

The simulation electric field power spectra for $m = 1.5$, 3.0, and 4.0 are shown in Figure (4.8). Notice that the pump wave frequency is chosen purposely as the mean of the upper hybrid wave frequency and the electron gyroharmonic frequency to facilitate the generation of the four-wave process. Hence the upper hybrid wave frequency is $\omega_{\rm uh} = 4\Omega_{\rm ce} + 2m\omega_{\rm lh}$. These spectral plots are captured after the simulation process has reached a steady state. The asymmetry property is evident for all these cases as the lower sidebands have damped significantly. Figure (4.8) shows that for smaller $\Delta\omega_0$, the frequency range of the upshifted sideband power is closer to the pump frequency. In Figure (4.8a), the peak of the power in the upshifted sideband in near $(\omega - \omega_0)/\omega_{\rm lh} = 2$, and in Figure (4.8c), the peak of the upshifted sideband power is near $(\omega - \omega_0)/\omega_{\rm lh} = 5$. The variation of the temporal evolution of the sideband amplitude and electron temperature with $\Delta\omega_0$ is shown in Figure (4.9). As is seen in Figure (4.9), both the upper hybrid waves and the electron Bernstein waves reach the steady state after the initial growth region. The simulation with $m = 1.5$ has the largest growth rate and saturates at the highest level for both the lower and upper sidebands. At the same time, more electron heating is observed for a smaller frequency offset. The downshifted electron Bernstein wave has a somewhat larger amplitude for the small $\Delta\omega_0$ as well.

4.4 Effects of varying the harmonic number: $\omega_0 = n\Omega_{\rm ce} + 3\,\omega_{\rm lh}$, $v_{\rm osc}/v_{\rm te} = 0.35$

The effects of increasing the harmonic number n on the four-wave process are shown in Figures (4.10) and (4.11) for $n = 3, 5, 7$. As n is increased for a fixed frequency offset $\Delta\omega_0$, the sidebands grow at a larger rate and reach a higher saturation level, and more electron heating is involved, as is observed in Figure (4.11). Figure (4.10) shows that the spectral maximum moves closer to the pump frequency and has a larger amplitude with increasing n. These simulation results are consistent with the predictions of the four-wave theoretical model as shown in Figure (3.5), where the growth rate increases with n.

(a) $\Delta\omega_0$=1.5ω_{lh}

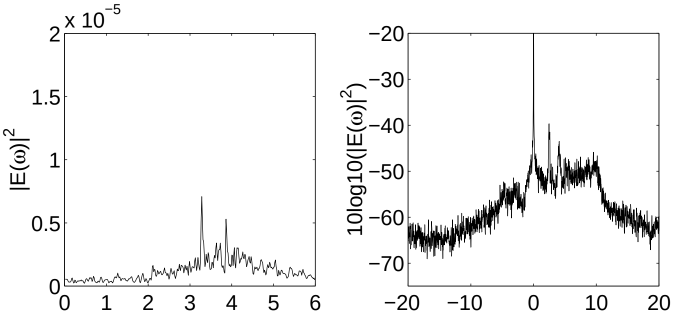

(b) $\Delta\omega_0$=3.0ω_{lh}

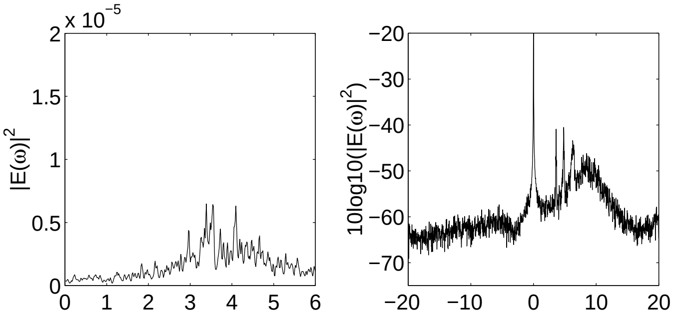

(c) $\Delta\omega_0$=4.0ω_{lh}

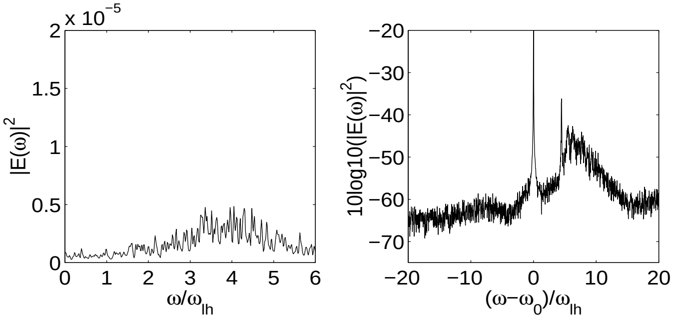

Figure 4.8: Simulation electric field power spectra showing the broad upshifted and and broad downshifted spectral features for $1500 < \omega_{\rm lh}t < 2500$. Here $\omega_0 = 4\Omega_{\rm ce} + m\omega_{\rm lh}$ (m = 1.5, 3, 4) and $\upsilon_{\rm osc}/\upsilon_{\rm te} = 0.35$.

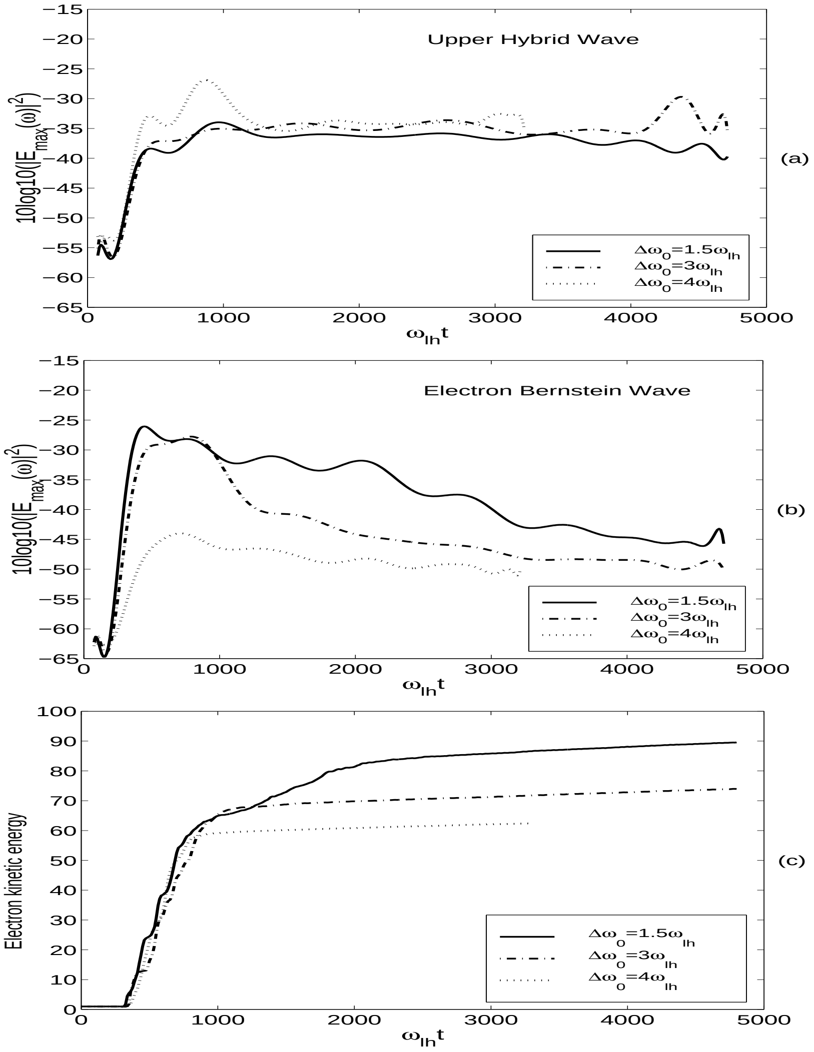

Figure 4.9: Results showing the time evolution of the peak amplitude of both the upper hybrid and electron Bernstein waves and the kinetic energy history for $\omega_0 = 4\Omega_{\rm ce} + m\omega_{\rm lh}$ (m = 1.5, 3, 4) and $\upsilon_{\rm osc}/\upsilon_{\rm te} = 0.35$.

(a) Third harmonic

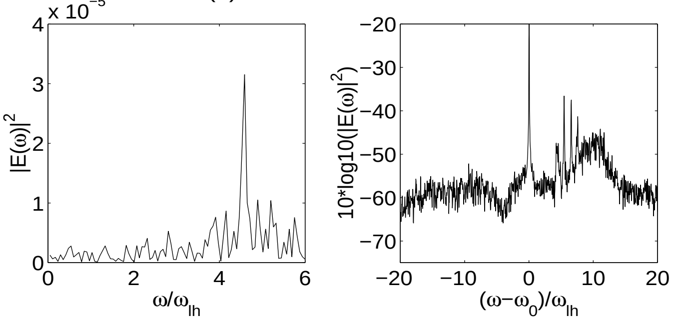

(b) Fifth harmonic

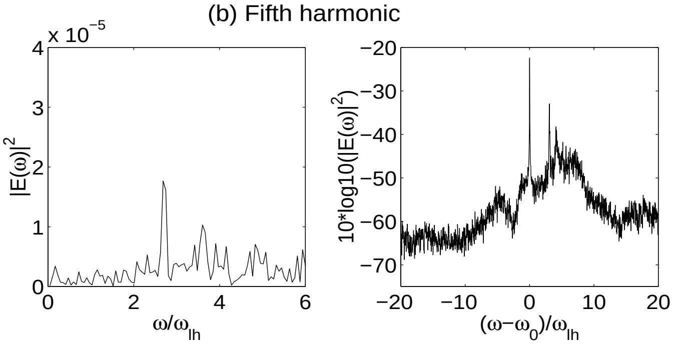

(c) Seventh harmonic

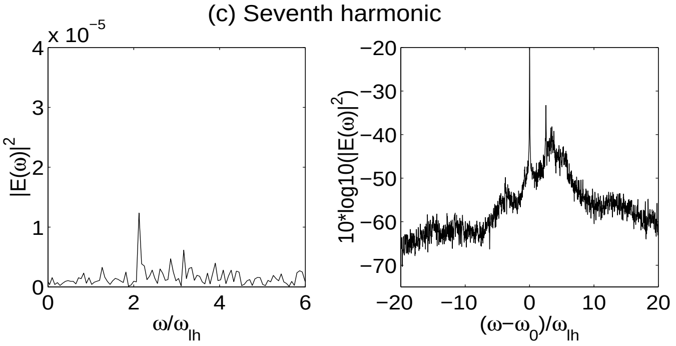

Figure 4.10: Simulation electric field power spectra showing the broad upshifted and and broad downshifted spectral features for $1500 < \omega_{\rm lh}t < 2500$. Here $\omega_0 = n\Omega_{\rm ce}+3\omega_{\rm lh}$ (n = 3, 5, 7) and $\upsilon_{\rm osc}/\upsilon_{\rm te} = 0.35$.

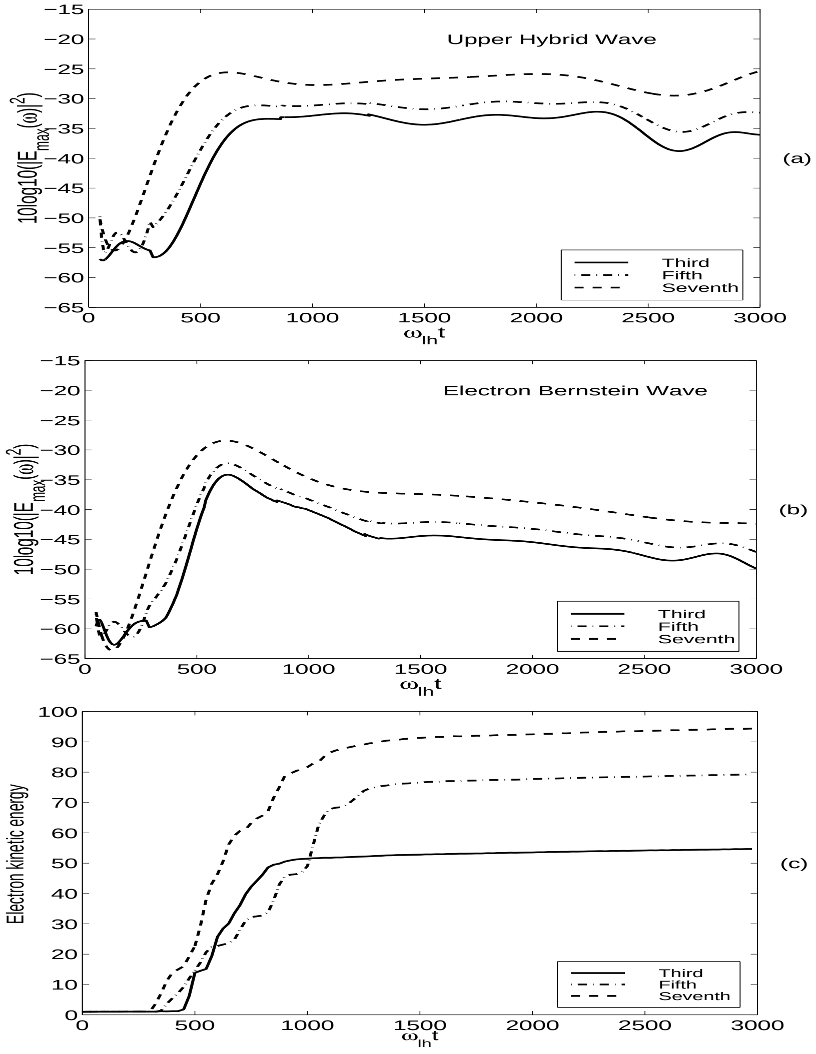

Figure 4.11: Results showing the time evolution of the peak amplitude of both the upper hybrid and electron Bernstein waves and the kinetic energy history for $\omega_0 = n\Omega_{\rm ce} + 3\omega_{\rm lh}$ (n = 3, 5, 7) and $\upsilon_{\rm osc}/\upsilon_{\rm te} = 0.35$.

4.5 Cyclotron damping

The mechanism of cyclotron damping is as follows. When a particle moving along B_0 in a wave with finite k_z, parallel component of k to B_0, has the right velocity, it sees a Doppler-shifted frequency $\omega - k_\mathrm{z} v_\mathrm{z}$ equal to $n\Omega_\mathrm{c}$ and is therefore subject to continuous acceleration by the electric field $E_\perp$ of the wave. Those particles with the right phase relative to $E_\perp$ will gain energy while those with wrong phase will lose energy. Since the energy change is the force times the distance, the faster accelerated particles gain more energy per unit time than what the slower decelerated particles lose. There is, therefore, a net gain of energy by the particles, on the average, at the expense of the wave energy; and the wave is damped.

To clarify the physical mechanism of cyclotron damping, consider a wave with $\mathbf{k} = k_x\hat{x} + k_z\hat{z}$ with k_z positive. The wave electric field $E_\perp$ can be decomposed into left- and right-hand circularly polarized components, as shown in Figure (4.12). For the left-hand component, the vector $E_\perp$ at positions A, B, and C along the z axis appears as shown in Figure (4.12a). Since the wave propagates in the $+\hat{z}$ direction, a stationary electron would sample the vectors at C, B, and A in succession and therefore would see a left-rotating E-field. It would not be accelerated because its Larmor gyration is in the right-hand (clockwise) direction. However, if the electron were moving faster than the wave in the $\hat{z}$ direction it would see the vectors at A, B, and C in that order and hence would be resonantly accelerated if its velocity satisfied the condition $\omega - k_z v_z = -\omega_c$. The right-hand component of E would appear as shown in Figure (4.12b). Now an electron would see a clockwise rotating E-field if it moved more slowly than the wave, so that the vectors at C, B, and A were sampled in succession. This electron would be accelerated if it met the condition $\omega - k_z v_z = +\omega_c$. A plane or elliptically polarized wave would, therefore, be cyclotron damped by electrons moving in either direction in the wave frame.

4.6 Discussions and summary

The above simulation results have shown the full nonlinear development of the four-wave process that is believed to be responsible for the asymmetric SEE spectrum in the steady state. *Huang and Kuo* [1994] suggested that because the electron Bernstein wave carries a larger kinetic energy to potential energy ratio than that associated with the upper hybrid wave, the wave field of the upper hybrid wave is much larger than that of the electron Bernstein wave given the same total energy. Our results indicate that a more likely self-consistent description of the evolution of this spectrum is as follows. As the four-wave instability develops, the associated wave-particle interactions elevate the electron temperature as is observed in Figure

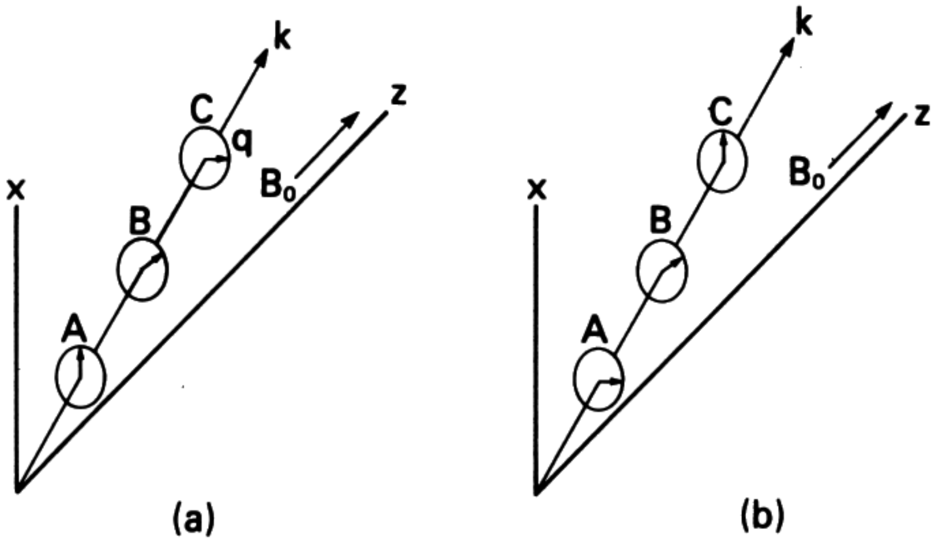

Figure 4.12: The mechanism of cyclotron damping.

(4.2a). This elevated T_e enhances the cyclotron damping, which is described in the previous section, of the electron Bernstein wave, damps the electron Bernstein wave, and eventually leads to the asymmetric spectrum after saturation.

In the present work, good agreement has been found between the predictions of the theoretical calculations and the numerical simulations. A number of consistent trends have been found in varying some important plasma and pump parameters. The early stage of the development of this process in nonlinear numerical simulations agrees well with past theoretical predictions of the growth rate. An overshooting in the amplitude of the upper hybrid wave after the saturation is clearly seen as consistent with previous experimental observations. The characteristics of the four-wave decay instability spectrum in the steady state stage when varying the pump frequency are consistent with past frequency stepping experiments. Experimental evidences [*Frolov et al.,* 1998] suggest that the BUM feature has the nature of two components, namely, the BUM_1 and the BUM_2, with different characteristics. These two components are possibly caused by different physical processes and thus need to be treated separately. An important characteristic of the BUM_1 feature is that it may exist for pump frequencies ω_0 slightly below the cyclotron harmonic frequency $n\Omega_{\text{ce}}$. The results we present here describing the evolution of the four-wave process are relevant to the BUM_2 feature. This is true, since the four-wave theory of *Huang and Kuo* [1994] predicts that the BUM does not exist when $\omega_0 \leq n\Omega_{\text{ce}}$. Before progress is made in investigating the BUM_1 feature, a firm theoretical foundation must be developed. We believe that nonlinear numerical simulations as we describe here will be crucial in investigating the physical mechanisms associated with this component of the BUM. Investigations for the case of $\omega_0 \leq n\Omega_{\mathrm{ce}}$ which are relevant to the BUM_1 will be the subject of future investigations.

Although numerous ionospheric modification experiments have been conducted so far, the effects of varying the harmonic number on the BUM features have not drawn enough attention. One reason is that it is much more convenient to perform the frequency stepping experiments around one gyroharmonic frequency than keeping track of multiple gyroharmonic frequencies. Our preliminary results show that for fixed frequency offsets and pump amplitudes the sidebands saturate at a higher level with a larger growth rate with increasing n. At the same time, more electron heating is involved and the BUM moves closer to the pump frequency with a larger amplitude.

Chapter 5

The Possible Role of Velocity Space Ring-plasma Instabilities in Upshifted SEE Production

The parametric four-wave process discussed in the previous two chapters has been one of the primary mechanisms proposed for the generation of the BUM SEE spectral feature. *Shvarts and Grach* [1997] noted that the efficiency of the nonlinear four-wave interaction should decrease significantly if $\Delta\omega_0 \gg \omega_{\mathrm{lh}}$. In Chapter 3, we also observed that the growth rate decreases substantially when $\Delta\omega_0/\omega_{\mathrm{lh}}$ increases. *Grach* [1999] noted that a cyclotron instability produced by the accelerated electrons might also lead to the formation of the upshifted plasma-wave spectrum in the BUM frequency range. In other words, the instability develops more efficiently in the region of normal dispersion of the upper-hybrid waves than that of the Bernstein waves. Thus an upshifted asymmetric spectrum is formed as a result of the difference between the growth rates in those two regions.

In this chapter, we will study the velocity space ring-plasma instability as a possible mechanism for the generation of the BUM in the SEE spectrum. First we will review past studies on the velocity space ring-plasma instability. We then present the theoretical model and propose a method to solve the dispersion relation. The results found around the fourth harmonic are discussed in the following section. The effects of varying plasma-wave parameters, such as the propagation angle, $\Delta\omega_0$, the harmonic number, the pump amplitude, and the percentage of ring electrons, are also considered. Finally a detailed comparison is made between the role of the velocity space ring-plasma and the four wave instabilities in producing the BUM spectra in the SEE.

5.1 Introduction

As shown in Figure (5.1), it is well known that a beam-plasma-like instability occurs when the beam is a ring in velocity space at speed $v_{\rm br}$ with the ring thermal spread, $v_{\rm tr} \ll v_{\rm br}$ and the background plasma is cold, $v_{\rm tp} \ll v_{\rm br}$. Waves propagating at a direction perpendicular to the uniform magnetic field $\mathbf{B} = B_{0\rm z}\hat{z}$ may be produced.

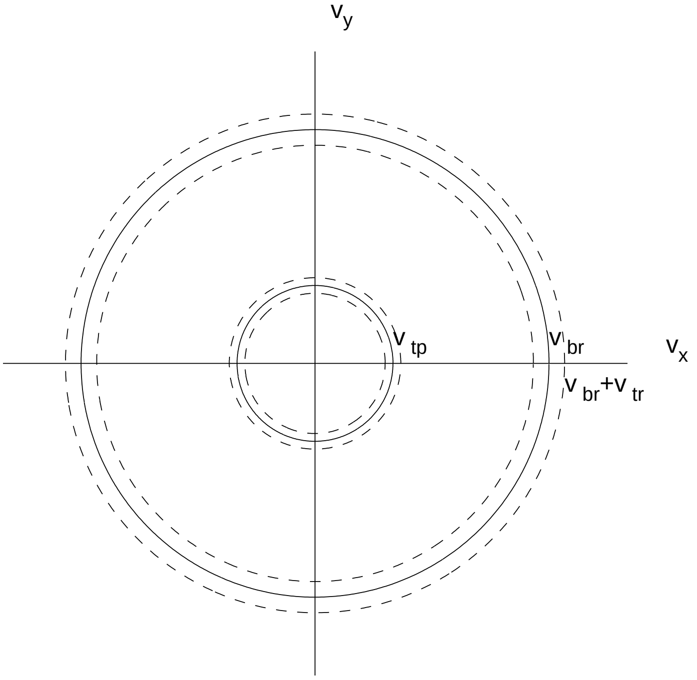

Figure 5.1: The distribution function of the two-component homogenous plasma in velocity space perpendicular to a uniform magnetic field $\mathbf{B} = B_{0\rm z}\hat{z}$. The cold homogenous plasma is a Maxwellian with thermal velocity $v_{\rm tp}$; the ring has a relatively high mean velocity $v_{\rm br}$ with thermal spread $v_{\rm tr}$. The wave vector considered for the unstable waves is in the x direction. Therefore the model is one-dimensional.

The interaction of the ring with a homogenous background cold plasma drives a flute-like velocity-space instability. For instance, Lee and Birdsall [1979] studied an ion ring-plasma instability using linear Vlasov theory and numerical simulation. While electrons are found to play a relatively unimportant role in the above ion-ion instability, recent studies indicate that acceleration of electrons might be crucial in generation of plasma instabilities that produce the SEE. For a hot electron ring, a distribution function with $\partial f/\partial v_{\perp} > 0$ as shown in Figure (5.1) can be unstable with respect to plasma wave excitation. Such an instability can most efficiently be developed under double-resonance conditions where $\omega_0 \approx n\Omega_{\rm ce} \approx \omega_{\rm uh}$. This cyclotron instability explains the so-called "zebra structures" in the sporadic radio emission from the sun [*Zheleznyakov and Zlotnik*, 1975] and the radio emission of the ionospheric plasma exposed to energetic particle fluxes [*Yoon et al.*, 1996].

Grach [1999] proposed that this instability can lead to the generation of the BUM spectral component of the SEE. A schematic diagram in Figure (5.2) shows the production of an electron ring velocity distribution. In the SEE experiments, the electrons are accelerated by high-frequency plasma turbulence in the ionospheric F-region. Given sufficient amplitude, the pump wave drives a steady-state density of accelerated electrons. These heated electrons are trapped in the accelerating layer due to scattering of plasma waves and the return of electrons due to Coulomb collisions. When the pump frequency is close to the electron cyclotron harmonic frequency, fast electron distribution with significant traverse anisotropy is formed. In the F-layer of the ionosphere the frequency of electron-neutral collisions (ν_{em}) is much lower than the effective frequency of electron-electron and electron-ion collisions (ν_e^{eff}). As the effective collision frequency ν_e^{eff} is higher for slower electrons ($\nu_e^{eff}(v_\perp) \propto v_\perp^{-3}$), the faster relaxation of slower electrons due to Coulomb collisions with charged particles outside the accelerating layer may lead to the formation of a maximum over transverse velocities in the tail of the distribution function. The cyclotron instability of such a nonequilibrium distribution can result in generation of the plasma waves at frequencies above the pump wave frequency. These plasma waves may be related to the generation of the BUM component of the SEE spectrum.

5.2 Theoretical model

A generic electron ring-plasma model in the velocity space will be used in this chapter to study its possible role in the generation of the BUM spectra. It is assumed that our velocity-space ring-plasma system is neutral ($n_{0\mathrm{i}} = n_{0\mathrm{e}}$) and has uniform density and magnetic field $B_{0\mathrm{z}}$. The background plasma has a Maxwellian electron velocity distribution of thermal velocity v_{teb} with density n_{eb}. The background electrons have the following Maxwellian distribution

$$f_{\mathrm{eb}}(v_\perp, v_\parallel) = \frac{1}{\pi^{3/2} v_{\mathrm{teb}}^3} \exp\left(-\frac{v_\perp^2 + v_\parallel^2}{v_{\mathrm{teb}}^2}\right) \tag{5.1}$$

The hot electron ring has thermal velocity v_{teh} with density n_{er}. The electron ring distribution is constructed as a combination of one cold component with thermal velocity v_{tec} and one hot component with thermal velocity v_{teh} and is expressed as

$$f_{\mathrm{er}}(v_\perp, v_\parallel) = \frac{1}{\pi^{3/2} v_{\mathrm{teh}}^3 (1-\alpha)} \exp\left(-\frac{v_\parallel^2}{v_{\mathrm{teh}}^2}\right) \left[\exp\left(-\frac{v_\perp^2}{v_{\mathrm{teh}}^2}\right) - \exp\left(-\frac{v_\perp^2}{\alpha v_{\mathrm{teh}}^2}\right)\right] \tag{5.2}$$

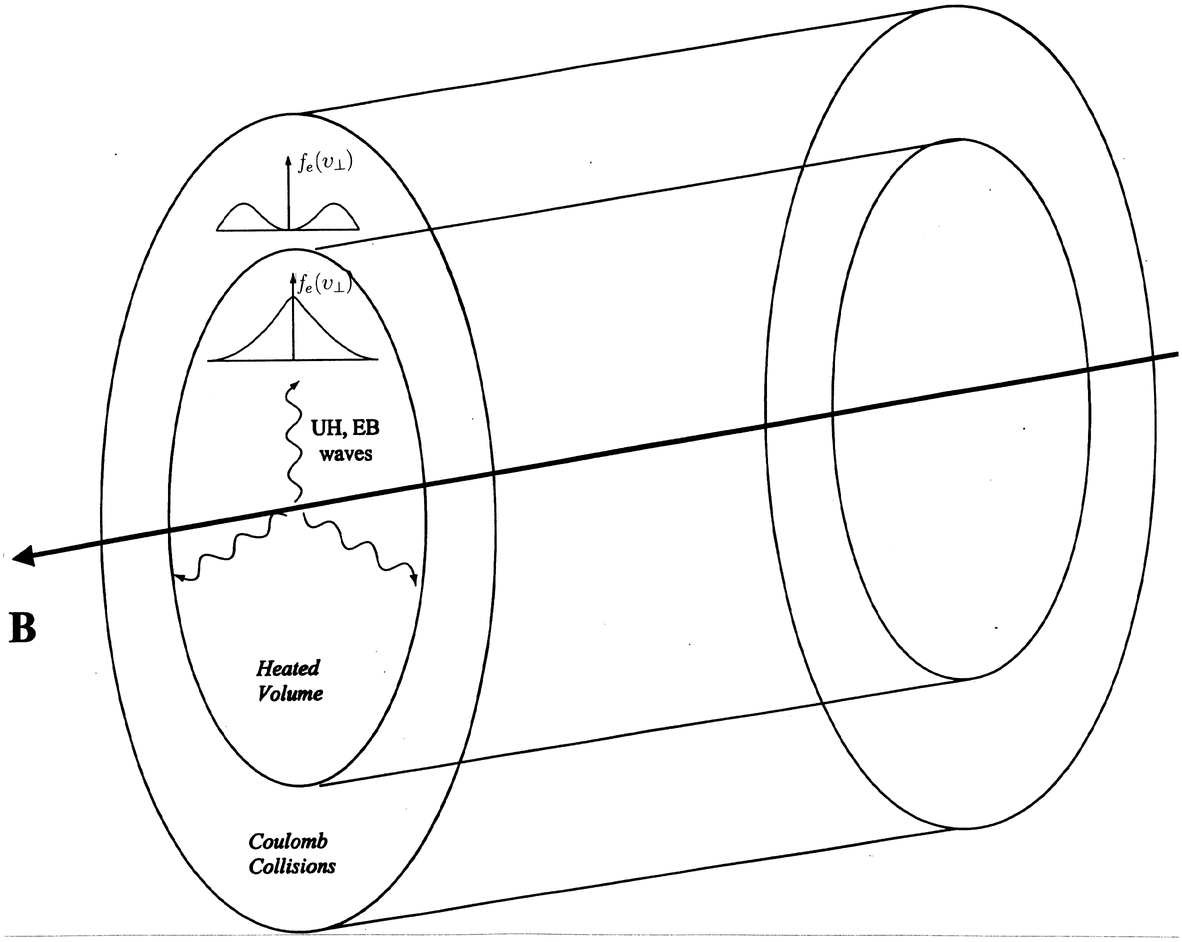

Figure 5.2: A schematic diagram showing the production of an electron ring velocity distribution during SEE experiments.

where $v_\perp (v_\parallel)$ is the velocity perpendicular (parallel) to the magnetic field $B_{0\mathrm{z}}$ and $\alpha = v_{\mathrm{tec}}^2/v_{\mathrm{teh}}^2 = T_{\mathrm{ec}}/T_{\mathrm{eh}}$ is the ring factor where $0 < \alpha < 1$.

Figure (5.3) shows the perpendicular velocity distribution with α =0.1 and 0.9. In the region with $\partial f/\partial v_\perp > 0$ where there are more faster particles than slow particles instability could develop.

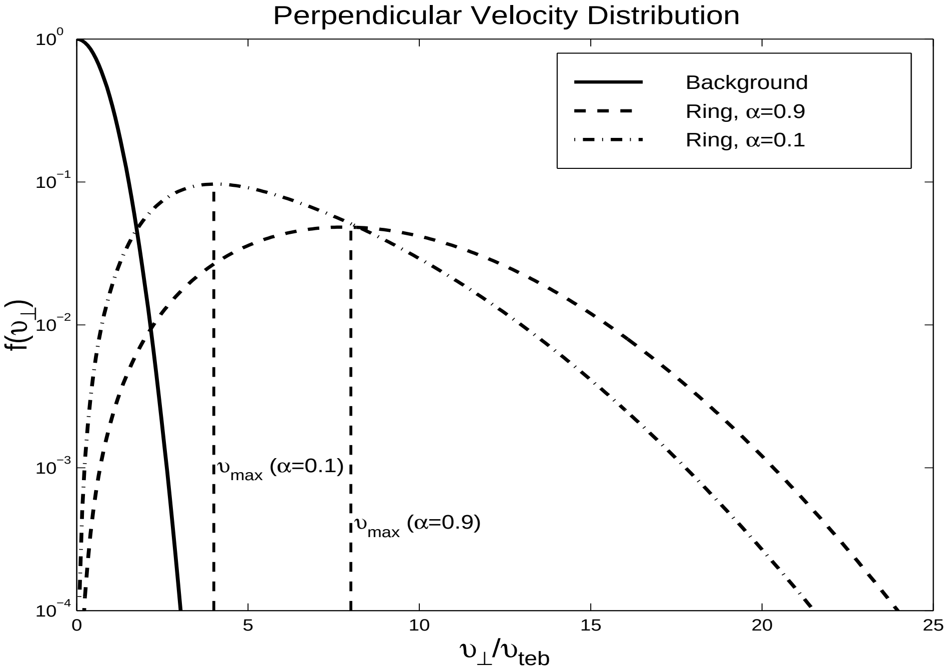

Figure 5.3: Plot for the ring-plasma perpendicular velocity distributions for $v_{\mathrm{teh}}^2/v_{\mathrm{teb}}^2 = 64$ and $\alpha = 0.9$ or 0.1.

The dispersion relation for waves produced by this distribution is given by

$$1 + \chi_{\mathrm{eb}} + \chi_{\mathrm{ib}} + \chi_{\mathrm{er}} = 0 \tag{5.3}$$

where χ_{eb} is the background electron susceptibility, χ_{ib} is the background ion susceptibility and χ_{er} is the ring electron susceptibility [*Ichimaru*, 1973].

The cool background electron susceptibility is given by (Appendix A)

$$\chi_{\mathrm{eb}}(\omega, k) = \frac{1}{k^2 \lambda_{\mathrm{Deb}}^2} \left\{ 1 + \zeta_{\mathrm{eb},0} \sum_{\mathrm{n}=-\infty}^{\infty} \Lambda_{\mathrm{n}}(\beta_{\mathrm{eb}}) Z(\zeta_{\mathrm{eb},n}) \right\} \tag{5.4}$$

where Z is the plasma dispersion (or the Fried Conte) function, $\beta_{\mathrm{eb}} = k_\perp^2 \rho_{\mathrm{eb}}^2/2$, $\zeta_{\mathrm{eb},n} = (\omega/\Omega_{\mathrm{ceb}} - n)/k_\parallel \rho_{\mathrm{eb}}$ (n is an integer), k is the wavenumber, ρ_{eb} is the gyroradius,

Ω_{ceb} is the cyclotron frequency, $\Lambda_{\mathrm{n}}(\beta_{\mathrm{eb}}) = I_{\mathrm{n}}(\beta_{\mathrm{eb}})\exp(-\beta_{\mathrm{eb}})$, I_{n} is the modified Bessel function of the first kind of order n, λ_{Deb} is the Debye length, and $k_{\|}(k_{\perp})$ is the component of k parallel (perpendicular) to $B_{0\mathrm{z}}$.

The background cold ion susceptibility is given by [*Ichimaru*, 1973]

$$\chi_{\mathrm{ib}}(\omega, k) = \frac{-\omega_{\mathrm{pi}}^2}{\omega^2} \tag{5.5}$$

Finally the ring electron susceptibility is given by (Appendix A)

$$\chi_{\mathrm{er}}(\omega, k) = \frac{1}{k^2\lambda_{\mathrm{Der}}^2}\left\{1 + \frac{1}{1-\alpha}\zeta_{\mathrm{er,0}}\sum_{\mathrm{n}=-\infty}^{\infty}\Lambda_{\mathrm{n}}(\beta_{\mathrm{er}})Z(\zeta_{\mathrm{er,n}}) - \frac{\alpha}{1-\alpha}\zeta_{\mathrm{er,0}}\sum_{\mathrm{n}=-\infty}^{\infty}\Lambda_{\mathrm{n}}(\alpha\beta_{\mathrm{er}})Z(\zeta_{\mathrm{er,n}}) \right.$$
$$\left. - \frac{1}{\omega/\Omega_{\mathrm{cer}}}\zeta_{\mathrm{er,0}}\sum_{\mathrm{n}=-\infty}^{\infty} n\Lambda_{\mathrm{n}}(\alpha\beta_{\mathrm{er}})Z(\zeta_{\mathrm{er,n}})\right\} \tag{5.6}$$

Next we will determine the parameter condition for instability to occur. Let us revisit the ring velocity distribution function (5.2). The instability condition is:

$$v_{\mathrm{phase}} = \frac{\omega}{k} \leq v_{\mathrm{max}}$$

where v_{max}, the most probable ring velocity as shown in Figure (5.3), is given by

$$\frac{\partial f_{\mathrm{er}}(v_{\perp}, v_{\|})}{\partial v_{\perp}} = 0 \ at \ v_{\perp} = v_{\mathrm{max}}$$

From this condition, it can be derived that the criteria for instability is

$$r_{\mathrm{temp}} \geq \frac{\alpha - 1}{\alpha\,\mathrm{ln}\alpha}\left(\frac{\bar{\omega}}{k\rho_{\mathrm{e}}}\right)^2 \tag{5.7}$$

where $r_{\mathrm{temp}} = T_{\mathrm{eh}}/T_{\mathrm{eb}}$ is the temperature ratio of the hot ring electrons to the background electrons, and $\bar{\omega} = w/\Omega_{\mathrm{ce}}$ is the normalized frequency.

For the fourth electron cyclotron harmonic $\bar{\omega}/(k\rho_{\mathrm{e}}) \approx 4$. The relationship between the ring factor and temperature ratio is shown in Table 5.1. It is observed that when α decreases, r_{temp} will have to be increased large enough for instability to occur.

Once instability is established, the growth rate depends on relative concentration of suprathermal electrons approximately as [*Grach*, 1999]

$$\gamma \sim \frac{n_{\mathrm{er}}}{n_{\mathrm{eb}}}\Omega_{\mathrm{ce}} \tag{5.8}$$

r_{temp}	α
400	0.0083
100	0.051
64	0.0966
36	0.2346

Table 5.1: Ring factor and temperature ratio relation for instability which will be considered in detail in the next section.

where n_{er}, n_{eb} are the electron densities of hot ring and cold background, respectively. Typically the ring percentage $r_{\text{percent}} = n_{\text{er}}/n_{\text{eb}} \sim 0.01\% - 0.1\%$ for significant growth.

5.3 Solution around the fourth cyclotron harmonic

To establish a base for comparison with the four-wave parametric instability process discussed in the previous two chapters the solution around the fourth cyclotron harmonic will be considered in this section. Again, the method of *Rönnmark* [1983] is used to calculate the electron susceptibilities in equations (5.4) and (5.5) and their derivatives with respect to ω. The Newton Raphson method is then used to find the root for equation (5.3). The FORTRAN program developed is shown in Appendix C.

An artificial ion-electron mass ratio $m_{\text{i}}/m_{\text{e}} = 400$ is used for consistency with calculations in Chapter 3 and it will not qualitatively alter the physical mechanism for the instability. The dispersion relation has been solved for a wide range of parameters. The upper hybrid wave frequency is given by $\omega_{\text{uh}} = 4\Omega_{\text{ce}} + 0.2\omega_{\text{lh}}$. The ring factor is α=0.5. The hot ring temperature ratio $r_{\text{temp}} = 576$. Note that $r_{\text{temp}} > 23$, which is required by equation (5.6) for instability to develop. The propagation angle with respect to the direction perpendicular to the magnetic field B is taken to be $\theta = 0.05°$. To produce a significant growth rate, the ring percentage is chosen to be $r_{\text{percent}} = 0.01$. Figure (5.4) shows the dispersion relation for the electron Bernstein and upper hybrid waves as well as the growth rates. It is apparent that the instability develops much more efficiently for the upper hybrid waves. The maximum of the growth rate $\gamma_{\text{max}}/\omega_{\text{lh}} \approx 0.3$ is reached when $\omega_{\text{uh}} - n\Omega_{\text{ce}}$ is very small, which is consistent with the analysis described in *Grach* [1999]. The growth rate $\gamma \approx 0.015$ is also found to be consistent with the condition for instability in equation (5.7). The wavenumber regions over which the instability grows are also shown. While the upper hybrid wave has a larger growth rate, the electron Bernstein wave has growth over a wider wavenumber range.

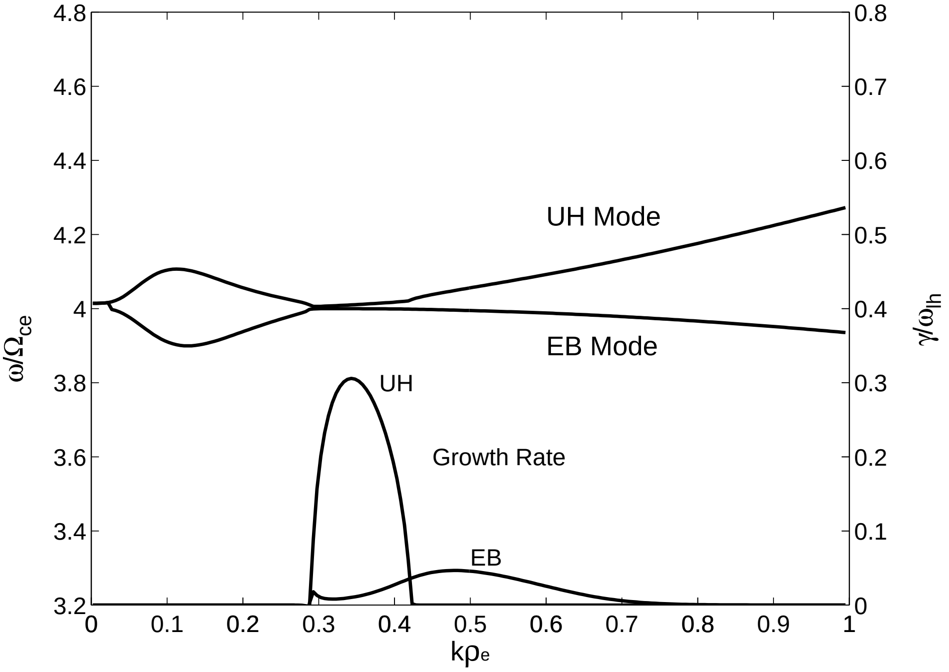

Figure 5.4: Plot for the growth rate γ versus wavenumber $k\rho_\mathrm{e}$ and the dispersion relation for the upper hybrid (UH) and the electron Bernstein (EB) modes for the case $\omega_\mathrm{uh} = 4\Omega_\mathrm{ce} + 0.2\omega_\mathrm{lh}$, $\theta = 0.05°$, $r_\mathrm{percent} = 0.01$, $\alpha = 0.5$ and $r_\mathrm{temp} = 576$.

Figure (5.5) shows the relationship between the frequency and the growth rate. Such a plot is very useful to study the spectral behavior qualitatively. More details will be provided in Section 5.9 for a comparison with the four wave decay process.

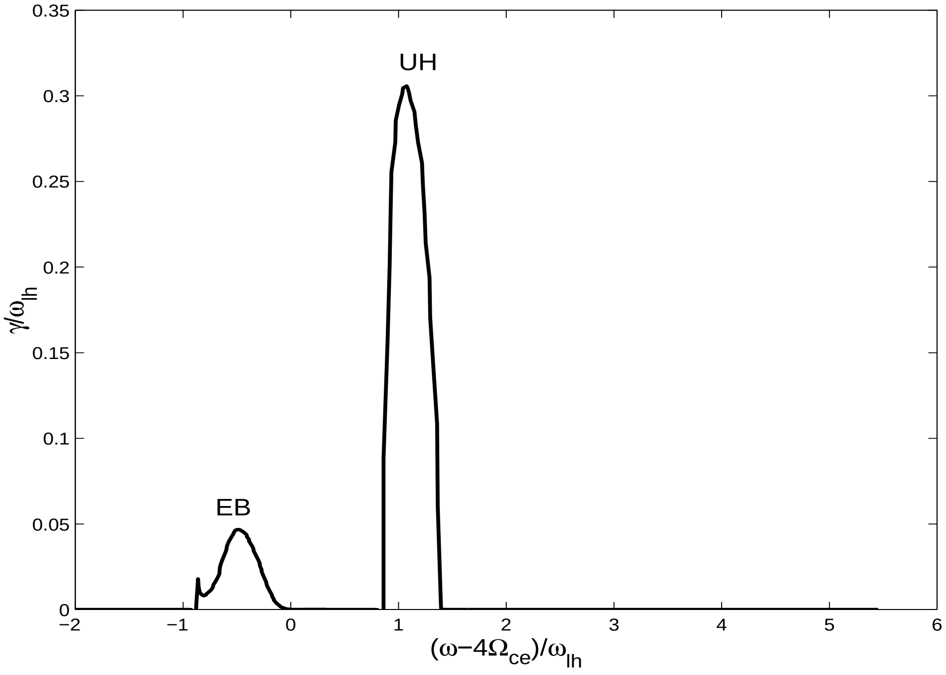

Figure 5.5: Plot for the growth rate γ versus frequency $(\omega - 4\Omega_{\mathrm{ce}})/\omega_{\mathrm{lh}}$ for the case $\omega_{\mathrm{uh}} = 4\Omega_{\mathrm{ce}} + 0.2\omega_{\mathrm{lh}}$, $\theta = 0.05^\circ$, $r_{\mathrm{percent}} = 1\%$, $\alpha = 0.5$ and $r_{\mathrm{temp}} = 576$.

A number of dispersion calculations have been performed to examine the effects of plasma parameters on the development of the ring velocity plasma instability. The results of those calculations are presented in the following sections in terms of the growth rates in the regions of upper hybrid and electron Bernstein wave frequencies.

5.4 Effects of varying the ring temperature

The ring temperature plays an important role in the development of ring-plasma instability in that hotter electrons tend to form a steeper velocity distribution. When $|\partial f/\partial v_\perp|$ increases, so does the growth rate. In Figure (5.6), it is observed that at $v_{\mathrm{er}}/v_{\mathrm{eb}} = 19.33$, the growth rate of the UH wave is equal to that of the EB wave, when $v_{\mathrm{er}}/v_{\mathrm{eb}} < 19.33$, the growth rate γ is greater for the EB wave. However, $\gamma_{\mathrm{uh}} \gg \gamma_{\mathrm{eb}}$ if $v_{\mathrm{er}}/v_{\mathrm{eb}} > 19.33$. Thus the hotter the ring temperature, the more asymmetric the BUM spectrum will be. It is also noted that the BUM will develop only in a certain ring temperature ratio region. When $v_{\mathrm{er}}/v_{\mathrm{eb}} < 19.33$, the broad down-shifted (BDM) spectrum may be produced. When $v_{\text{er}}/v_{\text{eb}} < 4$, as predicted by equation (5.7), there is no wave growth.

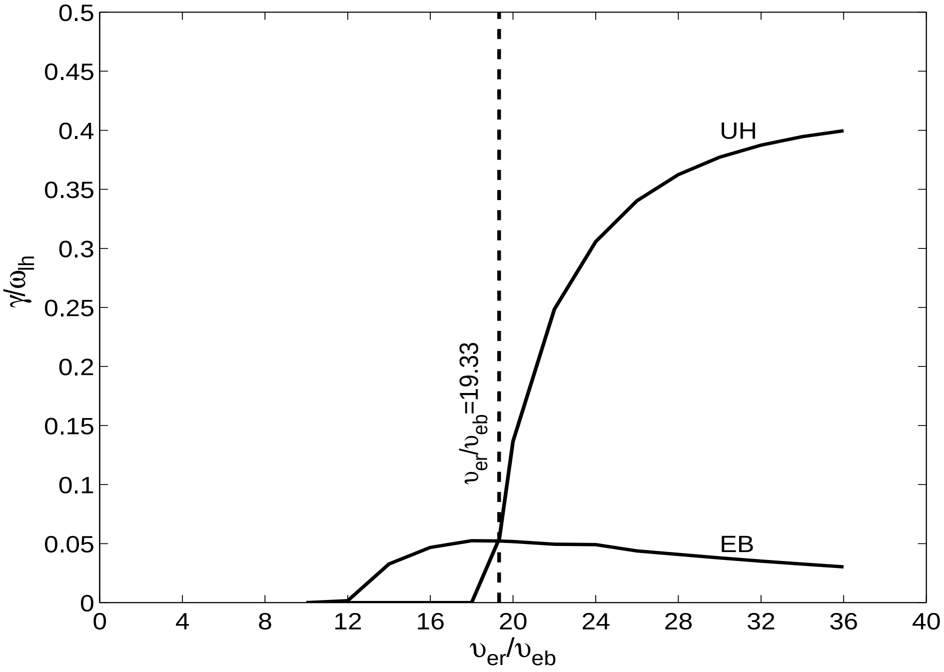

Figure 5.6: Plot for the growth rate for $\omega_{\text{uh}} = 4\Omega_{\text{ce}} + 0.2\omega_{\text{lh}}$, $\theta = 0.05°$, $r_{\text{percent}} = 1\%$, $\alpha = 0.5$, and $0 < v_{\text{er}}/v_{\text{eb}} < 40$.

5.5 Effects of varying the upper hybrid frequency

Figure (5.7) shows the growth rates when varying ω_{uh}. While the growth rate in the EB region remains relatively flat, the growth rate rises sharply near the double resonance when $(\omega_{\text{uh}} - 4\Omega_{\text{ce}})/\omega_{\text{lh}} \ll 1$. Thus when ω_{uh} is close to $n\Omega_{\text{ce}}$, the BUM spectrum will be much more prominent. Figure (5.8) shows the wavenumber regions for UH and EB wave instability. As ω_{uh} moves away from the electron cyclotron frequency, the wavenumber range for UH wave instability becomes much narrower. On the other hand, the wavenumber range for EB instability does not vary much as ω_{uh} changes.

5.6 Effects of varying the propagation angle

As shown in Figure (5.9), the growth rate γ_{uh} for the upper hybrid waves increases as θ moves closer to the direction perpendicular to the magnetic field and when $\theta = 0°$,

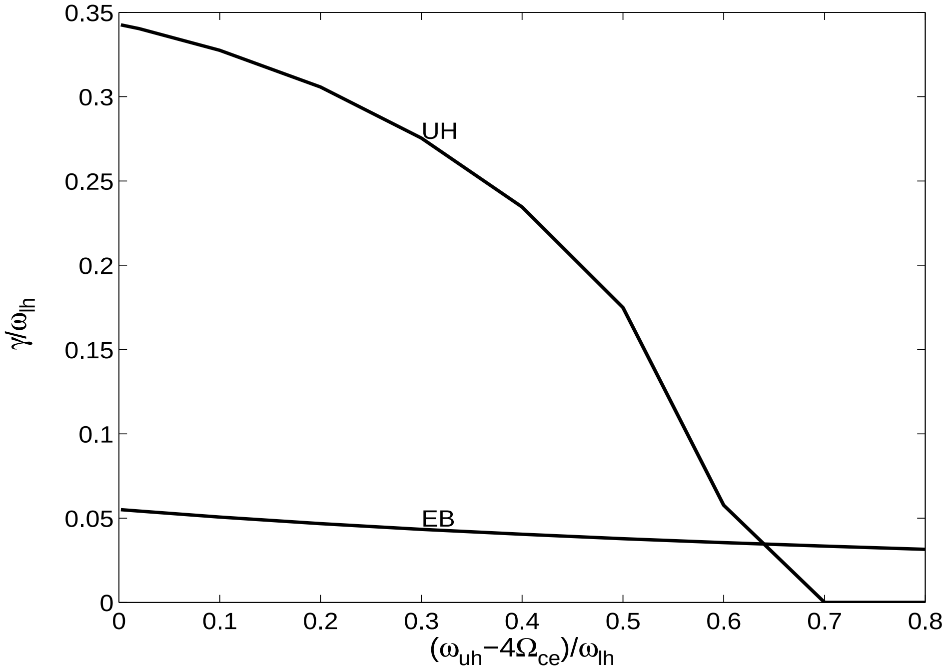

Figure 5.7: Plot for the growth rate for $\theta = 0.05°$, $r_{\text{percent}} = 1\%$, $\alpha = 0.5$, $r_{\text{temp}} = 576$, and $\omega_{\text{uh}} = 4\Omega_{\text{ce}} + (0 - 0.8)\omega_{\text{lh}}$.

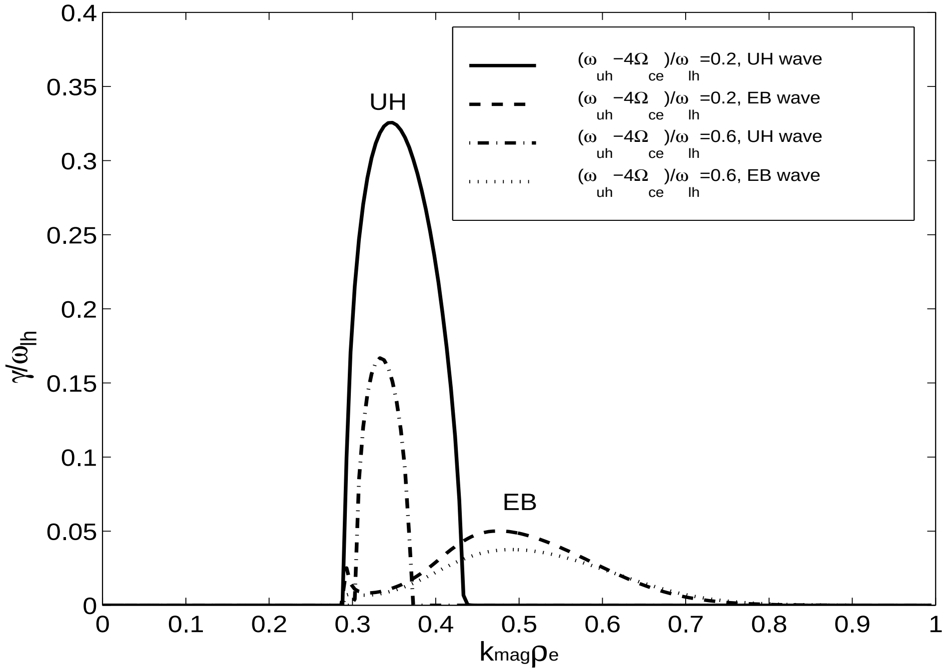

Figure 5.8: Plot for the UH and EB growth rates versus the wavenumber for $\theta = 0.05°$, $r_{\text{percent}} = 1\%$, $\alpha = 0.5$, $r_{\text{temp}} = 576$, and $\omega_{\text{uh}} = 4\Omega_{\text{ce}} + (0.2\, or\, 0.6)\omega_{\text{lh}}$.

$\gamma_{\rm uh}$ reaches the maximum. In contrast, $\gamma_{\rm eb} \approx 0$ if the direction is exactly at right angles to the magnetic filed $B_{0\rm z}$.

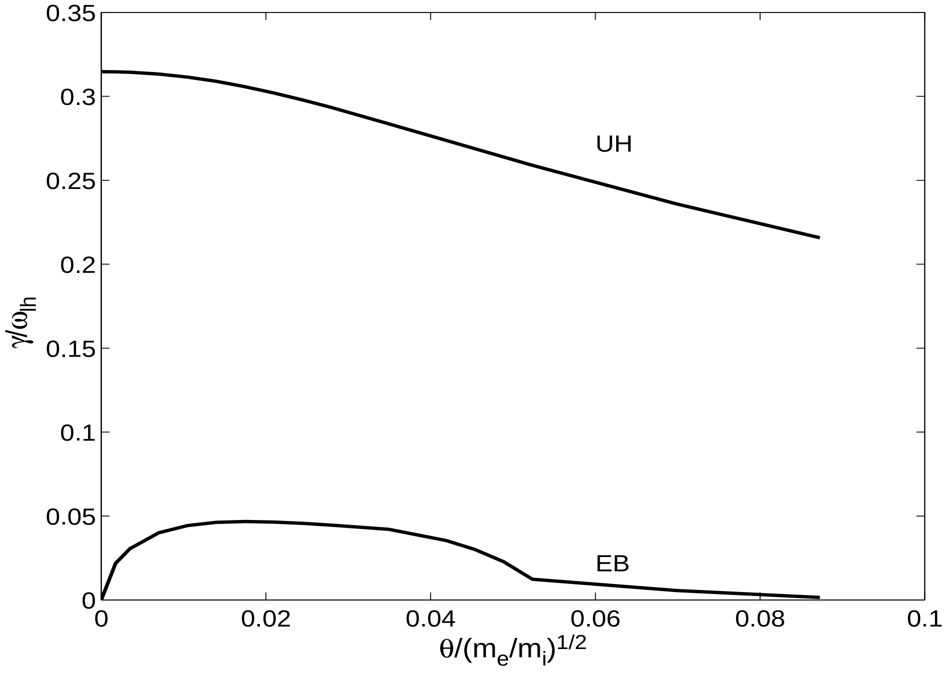

Figure 5.9: Plot for the growth rate for $\omega_{\rm uh} = 4\Omega_{\rm ce} + 0.2\omega_{\rm lh}$, $r_{\rm percent} = 1\%$, $\alpha = 0.5$, $r_{\rm temp} = 576$, and $0 < \theta/(m_{\rm e}/m_{\rm i})^{1/2} < 0.1$.

5.7 Effects of varying hot ring electron percentage

As predicted by equation (5.8), the growth rate is proportional to the hot ring percentage. In Figure (5.10), $\gamma_{\rm uh}$ and $\gamma_{\rm eb}$ increases nearly linearly as ring percentage increases, with $\gamma_{\rm uh}$ at a faster rate. For this set of parameters $\gamma_{\rm eb}$ is actually larger than $\gamma_{\rm uh}$ for small ring percentage.

5.8 Effects of varying the cyclotron harmonic number

The result in Figure (5.11) shows the growth rate γ for the cases $n\Omega_{\rm ce} < \omega_{\rm uh} < n\Omega_{\rm ce} + \omega_{\rm lh}$, where n=4, 5, 6, 7. It can be seen that the growth rate increases with the harmonic number. For a higher harmonic number, the instability develops is over a broader range in $\omega_{\rm uh}$.

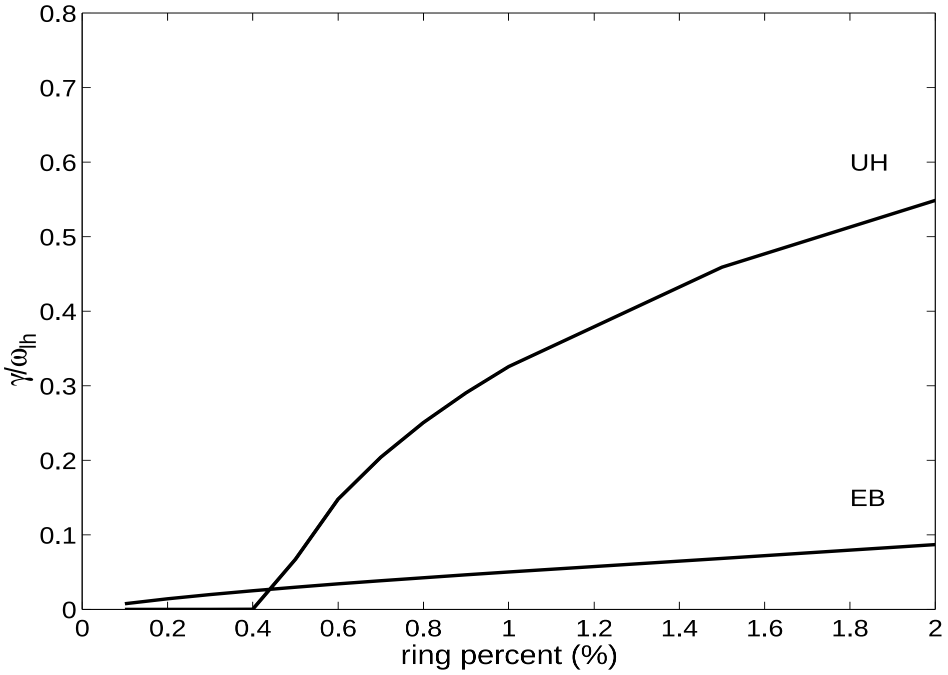

Figure 5.10: Plot for the growth rate for $\omega_{\text{uh}} = 4\Omega_{\text{ce}} + 0.2\omega_{\text{lh}}$, $\alpha = 0.5$, $r_{\text{temp}} = 576$, $\theta = 0.05°$, and $0.1\% < r_{\text{percent}} < 2\%$.

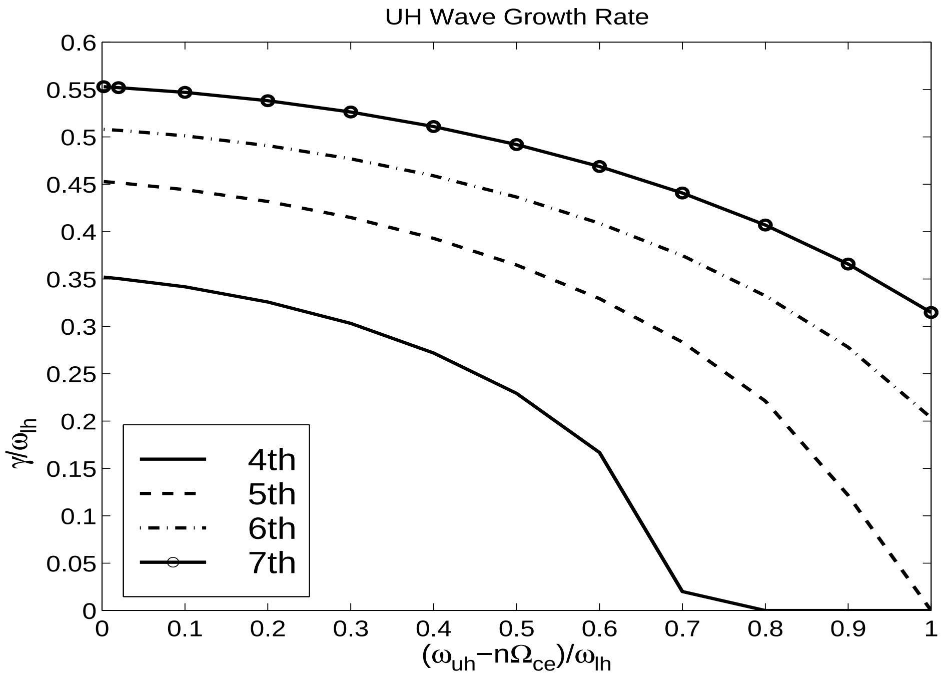

Figure 5.11: Plot for the growth rate for $\alpha = 0.5$, $r_{\text{temp}} = 576$, $\theta = 0.05°$, $r_{\text{percent}} = 1\%$, and $n\Omega_{\text{ce}} < \omega_{\text{uh}} < n\Omega_{\text{ce}} + \omega_{\text{lh}}$, where n = 4,5,6,7.

5.9 A comparison with the four-wave parametric process

The four-wave parametric process studied in the previous two chapters has long been thought as a possible generation mechanism for the BUM spectral feature. Our study also indicates that it provides a self-consistent explanation of the asymmetric spectrum. On the other hand, the velocity space ring-plasma instability is a relatively new theory that needs more intensive study. This chapter is an attempt in this direction. We studied this instability with a number of plasma parameters, which is much more detailed than presented by *Grach* [1999]. Our preliminary results suggest that this theory may be able to explain some of the important features. This section is devoted to providing an in-depth comparison of these two mechanisms and their possible relationship.

A plot of the growth rate versus the frequency such as Figure (5.5) can be used to study the frequency bandwidth of the instabilities. In the SEE experiments, instabilities develop over a finite angular region. Figure (5.8) and Figure (3.4) show the angular region for the velocity space ring-plasma instability and the four-wave decay instability, respectively. Thus, the relation of the growth rate and the frequency can be plotted over the angular region to conduct a better qualitative comparison with the experimental spectra. In Figure (5.12) we show the relation of the normalized (by the maximum growth rate) growth rate and the frequency for the ring-plasma instability. A similar plot for the four-wave instability is shown in Figure (5.13). It should be noted that the maximum growth rates are different in these two instabilities and the normalization is intended to provide a quantitative comparison in terms of the bandwidth. By comparing the bandwidth which gives the same logarithmic range for the normalized growth rate it can be seen that the ring instability has a broader frequency bandwidth ($4.0\omega_{\text{lh}}$) over the region of the upper hybrid waves than the four-wave process ($2.5\omega_{\text{lh}}$). More importantly, as the angle increases, the ring instability has a broader bandwidth. On the other hand, the bandwidth initially becomes broader with an increased angle for the four-wave process. However, as the angle continues to increase, the bandwidth becomes much narrower when $\theta = 8.00^\circ$. Thus, in agreement with *Shvarts and Grach* [1997], overall the ring instability tends to produce a broader bandwidth spectrum as the frequency moves away from the electron cyclotron frequency.

The most important difference of the two mechanisms is their explanation of the asymmetry in the BUM spectrum. For the velocity space ring-plasma instability, the reason is the difference in the linear growth rates. It is found that the upper hybrid wave has a faster rate than the electron Bernstein wave in the appropriate parametric regime. The possible formation of such a velocity space ring-plasma driven by a pump wave is explained by *Grach* [1999]. The energy is transformed from the pump wave

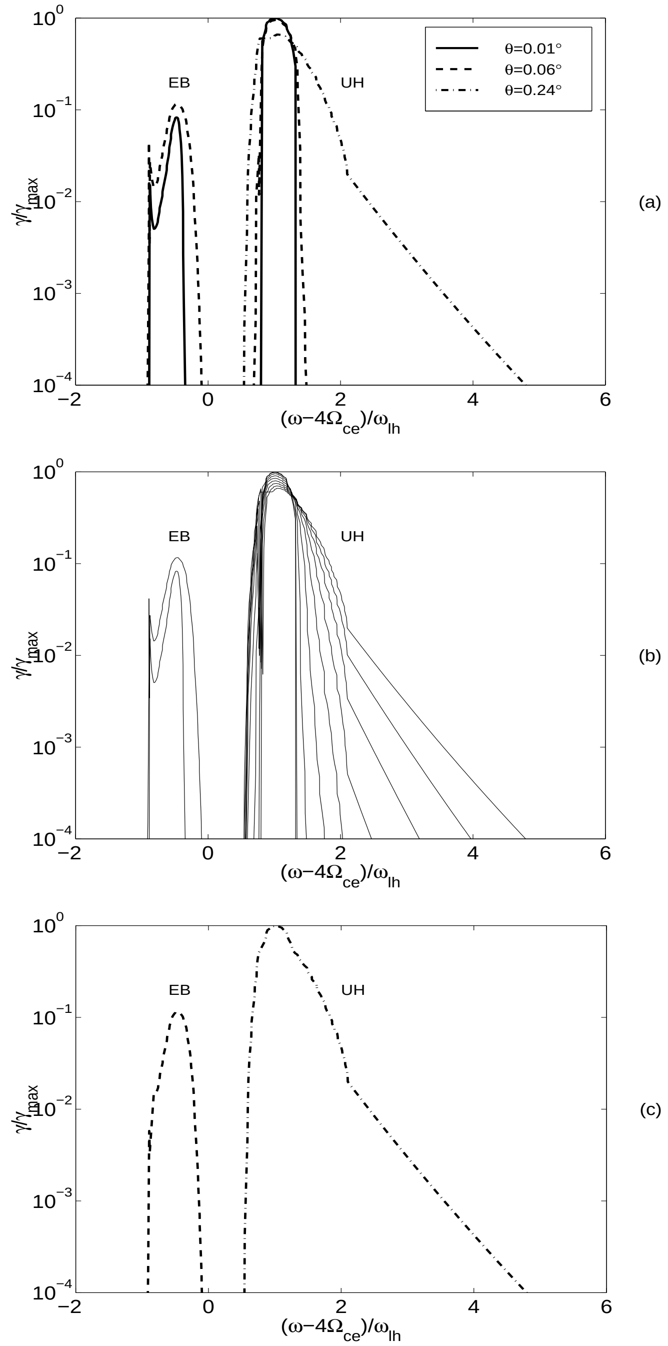

Figure 5.12: Plot for the normalized growth rate $\gamma/\gamma_{\rm max}$ versus frequency $(\omega - 4\Omega_{\rm ce})/\omega_{\rm lh}$ for ring-plasma instability for the case $\omega_{\rm uh} = 4\Omega_{\rm ce} + 0.2\omega_{\rm lh}$, $r_{\rm percent} = 1\%$, $\alpha = 0.5$, $r_{\rm temp} = 576$ and $\theta = 0.01°$, $0.03°$, $0.06°$, $0.09°$, $0.12°$, $0.15°$, $0.18°$, $0.21°$, $0.24°$. The cases for $\theta = 0.01°$, $0.06°$, $0.24°$ are shown in (a), all are shown in (b), and the envelopes, which are more relevant for comparison to experiments, are shown in (c). Note that $\gamma_{max}/\omega_{\rm lh} = 0.336$.

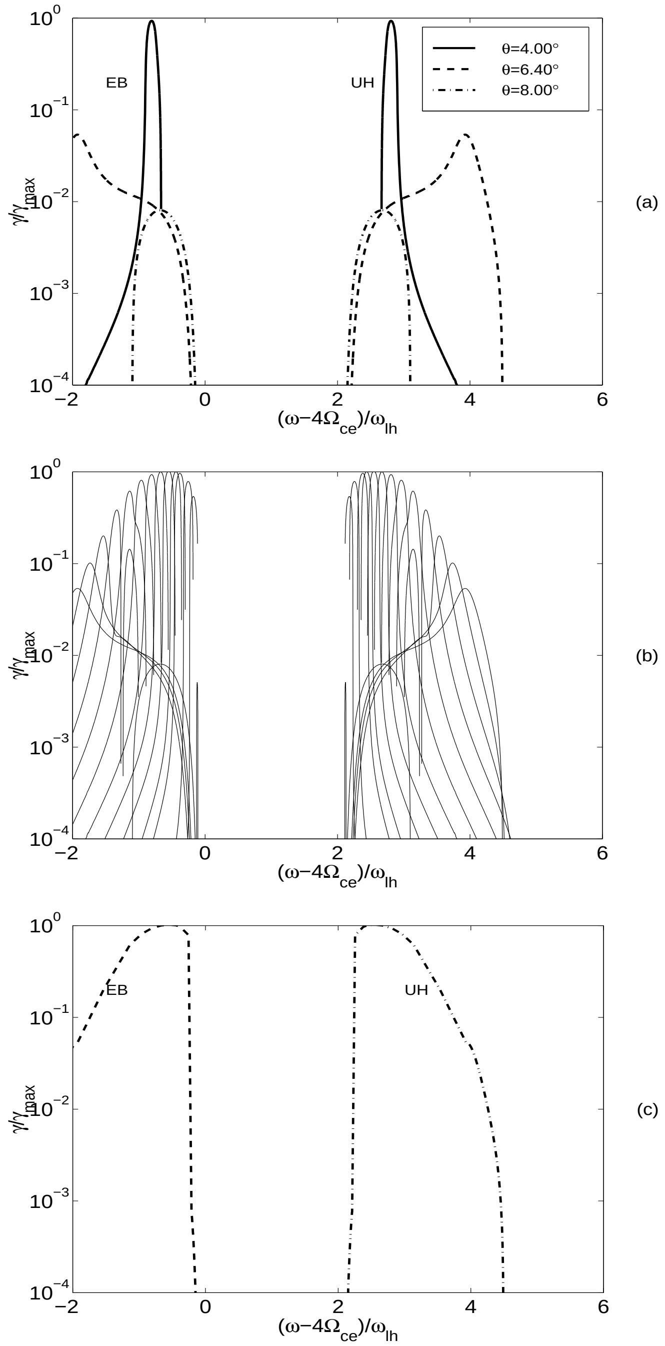

Figure 5.13: Plot for the normalized growth rate $\gamma/\gamma_{\rm max}$ versus frequency $(\omega - 4\Omega_{\rm ce})/\omega_{\rm lh}$ for four-wave decay instability for the case $\omega_{\rm uh} = 4\Omega_{\rm ce}+3\omega_{\rm lh}$, $v_{\rm osc}/v_{\rm te} = 0.35$ and $\theta = 1.28°$, $1.6°$, $2.0°$, $2.56°$, $2.8°$, $3.2°$, $3.6°$, $4.0°$, $4.4°$, $4.8°$, $5.2°$, $5.6°$, $6.0°$, $6.4°$, $8.0°$. The cases for $\theta = 4.0°$, $6.4°$, $8.0°$ are shown in (a), all are shown in (b), and the envelopes, which are more relevant for comparison to experiments, are shown in (c). Note that $\gamma_{max}/\omega_{\rm lh} = 0.07$.

to the heated electrons as the instability grows. The continuous energy flux from the pump wave maintains this velocity space instabilities and thus the ring instability can grow at a steady rate. In the four-wave process, the instability grows at the same rate initially for both the upper hybrid and electron Bernstein waves. However, after the saturation of the initial linear growth, the elevated electron temperature enhances the cyclotron damping and leads to the asymmetric spectrum. As to the spectral behavior, for the ring instability, the asymmetry shall appear from the beginning stage of the growth and become more prominent with a larger growth rate in the upper hybrid waves than the electron Bernstein waves. For the four-wave process, the two sidebands grow at a comparable rate initially. After saturation, the lower sideband is cyclotron-damped so the asymmetry shall appear at a late stage.

The two mechanisms also behave differently with respect to the changes in a number of parameters. First, their growth rates maximize at different propagation angles. From Figure (5.9), we observe that the ring instability has a maximum growth rate for the upper hybrid wave when $\theta = 0^\circ$, i.e., the wave propagates at an angle perpendicular to the magnetic field. Thus the BUM spectrum should be more prominent in that direction. Figure (3.2) suggests that the four-wave process maximizes its growth rate at $\theta_{\mathrm{max}} \simeq 3.0\sqrt{m_{\mathrm{e}}/m_{\mathrm{i}}}$. Second, the ring-plasma instability has a narrower range for a substantial growth rate. Figure (5.7) shows that the UH wave growth rate drops very rapidly when the upper hybrid wave moves away from the electron cyclotron frequency and becomes very small once $\omega_{\mathrm{uh}} = 4\Omega_{\mathrm{ce}} + 0.7\omega_{\mathrm{lh}}$. Thus the BUM spectrum will only appear in a close region of $n\Omega_{\mathrm{ce}}$. The four-wave instability has a broader frequency range as indicated in Figure (3.5). The growth rate decreases at a much slower pace, especially for low harmonic numbers. Third, their growth rates have a different trend when the electron temperature is increased. Figure (5.6) indicates that an increasing electron temperature leads to an increase in the growth rate in the upper hybrid wave region. On the other hand, the growth rate of the four-wave process decreases substantially with an increasing electron temperature. So it is possible that the four-wave process is dominant in the early linear growth period. As the electron temperature increases the ring-plasma instability becomes more significant in the late stages.

Despite all the differences above, two theories have one important behavior in common. They both involve significant acceleration of electrons in the direction perpendicular to $B_{0\mathrm{z}}$. In the four-wave process, the electrons are heated by the wave-particle interactions in the direction perpendicular to the magnetic field. Figure (4.6) indicates that tail heating is observed as the velocity distribution function becomes broader. Note that such a distribution function comprising suprathermal particles with $\partial f/\partial v_\perp > 0$ is the pre-condition for the velocity space ring-plasma instability. Thus these two mechanisms could actually co-exist and both contribute to the asymmetric upshifted SEE spectrum.

5.10 Summary

In this chapter we have studied the velocity space ring-plasma instability using a more general model than the one discussed by *Grach* [1999]. The ring instability is found to have a larger growth rate for the upper hybrid waves than that of the electron Bernstein waves. The asymmetric SEE spectrum may be explained by the difference in the growth rate. The ring-plasma instability is studied under various plasma parameter conditions. Some results have found good agreement with *Grach* [1999] as well as the SEE experiments. A detailed comparison with the four-wave parametric process is presented in section 5.9 where both the differences and the possible relations are discussed. While they have a number of different behaviors with respect to the variation of plasma parameters, the fact that both involve significant electron acceleration in the direction perpendicular to the magnetic field suggests they could both contribute to the formation of the asymmetric upshifted spectrum. Comparing Figure (3.5) to Figure (5.11) it can be seen that the growth rate decreases at a much faster rate for the ring-plasma instability than the four-wave process when the upper hybrid frequency moves away from the electron cyclotron frequency. In the previous section, we predict that the BUM spectrum produced by the ring-plasma instability only appears in a close region of the cyclotron harmonic frequency $n\Omega_{\text{ce}}$. So it may be possible that the ring-plasma instability produces the BUM_1 feature which was found only at frequencies in close proximity to the cyclotron frequency in the SEE experiments [*Frolov et al.* 1997, 1998]. However, further studies need to be performed to investigate their possible relationship. For example, it needs to be explained why the BUM_1 feature may exist for frequencies slightly below $n\Omega_{\text{ce}}$.

Chapter 6

Conclusions and Future Work

6.1 Summary and contributions

In this work, the instability processes thought to be responsible to the broad upshifted maximum spectra in the SEE experiments are discussed and analyzed using theoretical and numerical simulation models. The instabilities considered include the four-wave decay process and the velocity space ring-plasma instability. The results we presented are encouraging for having the potential of complementing the experimental observations and the theoretical analysis.

Chapter 1 provided a detailed study of the extant literature on the broad upshifted spectrum in SEE experiments. As one of the most prominent upshifted feature in the SEE spectrum, the BUM has been the subject of intensive research in ionospheric modification experiments. The proposed generation mechanisms for the BUM were reviewed and it was found that detailed studies were necessary to explore their full behaviors.

In Chapter 2 the fundamentals of plasma theory were reviewed followed by discussion of some of the important SEE spectral features including the BUM. A generation mechanism for the SEE was then presented with an explanation of the feasibility of using a particle-in-cell simulation model to conduct our investigations.

Chapter 3 studied the theoretical model of the four-wave decay process under various pump-wave parameters. The dispersion relations for the upper hybrid and the electron Bernstein waves were solved. The effects of varying the cyclotron harmonic number, the frequency offset, the pump amplitude, and the temperature ratio $T_\mathrm{e}/T_\mathrm{i}$ were considered.

A periodic one space dimension and three velocity dimension electrostatic particle-in-cell simulation model was used in Chapter 4 to investigate the full nonlinear evolution of the four-wave decay process. The time evolution of the electric field power spectrum, the electron phase space, the parallel and perpendicular electron velocity distribution functions, and the electron density was studied. The early stage of the development of the process in nonlinear numerical simulations agreed well with the theoretical prediction. A self-consistent description of the evolution of the asymmetric spectrum was presented. The four-wave decay process was found to be a good explanation for the BUM_2 feature. The effects of varying the harmonic number and the pump frequency were also considered. It was found that the effects of increasing the harmonic number n on the BUM feature to be similar to those of decreasing the frequency offset. As n was increased or the frequency offset was decreased, the sidebands grew at a larger rate and reached a higher saturation level, and more electron heating was involved. Moreover, the upshifted spectral peak moved closer to the pump frequency with a larger amplitude.

The velocity space ring-plasma instability was studied in Chapter 5 using a theoretical model. The ring instability was found to have a larger growth rate for the upper hybrid waves than that of the electron Bernstein waves. The asymmetric SEE spectrum might be explained by the difference in the growth rate. The ring-plasma instability was studied under various plasma parameter conditions. A detailed comparison with the four-wave parametric process was presented with a discussion of the differences and the possible relations. It was found that possibly the ring-plasma instability produces the BUM_1 feature which was found only at frequencies in close proximity to the cyclotron frequency in the SEE experiments.

This research has made the following original contributions.

1. By using both theoretical predictions and numerical simulations to study the four-wave decay process, it is found that the early linear stages of the development of this process in numerical simulations agree well with theoretical predictions (Section 4.2).

2. Using electrostatic PIC simulations the full nonlinear evolution on the characteristics of the saturated frequency spectrum has been studied in detail for the first time. This spectrum exhibits many of the important characteristics of the observed experimental spectra. In particular, it exhibits the asymmetric upshifted structure which has not been adequately or self-consistently described by past theoretical models. Our results indicate a likely self-consistent description of the evolution of this spectrum (Section 4.2).

3. The four wave decay process has been studied in greater detail here. A number of important plasma and pump wave parameters have been varied to study their

effects on the evolution of the BUM feature. In particular, the frequency offset and the harmonic number have been varied to explore their effects on the four-wave instability process. The theoretical analysis of the growth rate and the numerical simulations shows that the four-wave process is a good explanation for the generation of the BUM_2 component (Chapters 3 and 4).

4. We have studied the velocity space ring-plasma instability, which was more recently proposed as a generation mechanism for the BUM spectra, using a new theoretical model. The linear growth rate is found to be larger for the upper hybrid waves, which explains the asymmetric upshifted SEE spectrum (Chapter 5).

5. A detailed study of the velocity space ring-plasma instability has been conducted using various plasma parameters. It is predicted that the BUM shall be more prominent with a hotter ring, at the direction perpendicular to the magnetic field, or when ω_0 approaches $n\Omega_{ce}$ (Chapter 5).

6. A detailed comparison of the velocity space ring-plasma instability and the four-wave parametric process is presented where both the differences and the possible relations are discussed. The fact that both involve significant electron acceleration in the direction perpendicular to the magnetic field suggests they could both contribute to the formation of the asymmetric upshifted spectrum (Section 5.9). It was found that possibly the ring-plasma instability produces the BUM_1 feature which was found only at frequencies in close proximity to the cyclotron frequency in the SEE experiments (Section 5.10).

6.2 Related publications by the author

Several publications related to this research have been written by the author. These include two journal papers, one peer-reviewed conference paper, and two poster papers. Two journal papers, related to the theoretical and numerical simulation investigation of parametric processes associated with up-shifted ionospheric stimulated radiation using the four-wave process, were published in *Physics Scripta* [*Scales and Xi*, 2000] and *Journal of Geophysical Research* [*Xi and Scales*, 2001]. One peer-reviewed conference paper was presented at the *National Radio Science Meeting* (URSI) in January 2000. Two poster papers were presented at the *RF Ionospheric Interactions Workshop* in April 1998 and April 1999. Additionally a paper is in preparation for a detailed study on the velocity space ring-plasma instability and its comparison with the four-wave process.

6.3 Future work

We have presented in this work parametric studies of the four-wave decay process using theoretical and numerical models. The effects of pump frequency, harmonic number and propagation angle have been considered. Future work might consider the effects of pump power level, and the self-conditioning and pre-conditioning effects [*Wagner et al.*, 1999].

Experimental observations [*Frolov et al.* 1997, 1998] suggest that there are actually two components of the BUM, namely, the BUM_1, and the BUM_2. BUM_1 is found only at pump frequencies in close proximity to the gyroharmonic, while BUM_2 is present more generally over a range of pump frequencies in the vicinity of the gyroharmonic. These two components are possibly caused by different physical processes and thus need to be treated separately. An important characteristic of the BUM_1 feature is that it may exist for pump frequencies ω_0 slightly below the cyclotron harmonic frequency $n\Omega_{\mathrm{ce}}$. In this work we have mainly discussed the possible roles of the four-wave decay instability and the velocity ring-plasma instability in the production and moderation of the BUM_2 feature. The mechanism for the generation of the BUM_1 could be the subject of future investigation. It should be noted that the BUM_1 feature could be related to the ring-plasma instability.

The velocity-space ring-plasma instability has been studied using a theoretical model. A numerical model might be developed to consider the development of both the four wave decay process and the velocity space ring-plasma instability simultaneously. Such a model should be useful to explore their possible role in the production of the BUM_1 and BUM_2 spectral features. Possibly we could consider using the on-off pump pattern [*Wagner et al.*, 1999]. In other words, the simulation could numerically turn on the pump to observe the development of the four wave decay process. Once the electrons were substantially heated at the perpendicular direction, the pump could be turned off to study the development of the velocity space ring-plasma instability, The pump pattern and the pump-plasma parameters would have to be carefully chosen to be able to observe a meaningful period for both instabilities.

Appendix A

Electron Susceptibility for Velocity Space Ring Distribution

In this appendix, it is required to express the susceptibility for a velocity-space ring distribution.

For an isotropic Maxwellian distribution, the electron susceptibility is given by [*Ichimaru*, 1973]:

$$\chi_{\rm e} = \frac{k_{\rm e}^2}{k^2}\left\{1 + \sum_{\rm n=-\infty}^{\infty} \frac{\omega}{\omega - n\Omega_{\rm ce}}\left[W\left(\frac{\omega - n\Omega_{\rm ce}}{k_{\|}(T_{\rm e}/m_{\rm e})^{1/2}}\right) - 1\right]\Lambda_{\rm n}(\beta_{\rm e})\right\} \tag{A.1}$$

where $\Omega_{\rm ce}$ is the cyclotron frequency, $\beta_{\rm e} = k_{\perp}^2\rho_{\rm e}^2/2$, $\rho_{\rm e}$ is the gyroradius, $\Lambda_{\rm n}(\beta_{\rm e}) = I_{\rm n}(\beta_{\rm e})\exp(-\beta_{\rm e})$, $I_{\rm n}$ is the modified Bessel function of the first kind of order n, and $k_{\|}(k_{\perp})$ is the component of k parallel (perpendicular) to B_0. Note that the W function has the following relation with the Z function (the plasma dispersion function or the Fried Conte function).

$$W(\sqrt{2}\zeta) = 1 + \zeta Z(\zeta) \tag{A.2}$$

Thus to express $\chi_{\rm e}$ in terms of Z function (which is more commonly used) as opposed to W

$$\begin{aligned}
\chi_{\rm e} &= \frac{k_{\rm e}^2}{k^2}\left\{1 + \frac{\omega}{k_{\|}v_{\rm te}}\sum_{\rm n=-\infty}^{\infty} Z\left(\frac{\omega - n\Omega_{\rm ce}}{k_{\|}v_{\rm te}}\right)\Lambda_{\rm n}(\beta_{\rm e})\right\} \\
&= \frac{1}{k^2\lambda_{\rm De}^2}\left\{1 + \frac{\omega/\Omega_{\rm ce}}{k_{\|}\rho_{\rm e}}\sum_{\rm n=-\infty}^{\infty} Z\left(\frac{\omega/\Omega_{\rm ce} - n}{k_{\|}\rho_{\rm e}}\right)\Lambda_{n}(\beta_{\rm e})\right\} \\
&= \frac{1}{k^2\lambda_{\rm De}^2}\left\{1 + \zeta_{\rm e,0}\sum_{\rm n=-\infty}^{\infty} Z(\zeta_{\rm e,n})\Lambda_{\rm n}(\beta_{\rm e})\right\}
\end{aligned} \tag{A.3}$$

where $v_{\mathrm{te}} = \sqrt{2T_{\mathrm{e}}/m_{\mathrm{e}}}$, $\rho_{\mathrm{e}} = v_{\mathrm{te}}/\Omega_{\mathrm{ce}}$, $k_{\mathrm{e}} = 1/\lambda_{\mathrm{De}}$, and $\zeta_{\mathrm{e,n}} = (\omega/\Omega_{\mathrm{ce}} - n)/(k_{\|}\rho_{\mathrm{e}})$ (n is an integer).

The susceptibility for a hot ring velocity space distribution can be expressed in terms of the susceptibility for an isotropic and anisotropic Maxwellian distribution as follows (Appendix B)

$$\chi_{\mathrm{e,ring}} = \frac{1}{1-\alpha}\chi_{\mathrm{e,iso}} - \frac{\alpha}{1-\alpha}\chi_{\mathrm{e,ani}} \tag{A.4}$$

In a hot ring distribution, the susceptibility of the isotropic distribution component is assuming $T_{\mathrm{e}} = T_{eh}$ in (A.3)

$$\chi_{\mathrm{e,iso}} = \frac{1}{k^2\lambda_{\mathrm{Deh}}^2}\left\{1 + \zeta_{\mathrm{eh,0}}\sum_{\mathrm{n}=-\infty}^{\infty} Z(\zeta_{\mathrm{eh,n}})\Lambda_{\mathrm{n}}(\beta_{\mathrm{eh}})\right\} \tag{A.5}$$

For the anisotropic distribution component, the electron susceptibility is given by [*Ichimaru*, 1973]

$$\chi_{\mathrm{e,ani}} = \frac{k_{\mathrm{eh}}^2}{k^2}\left\{1 + \sum_{\mathrm{n}=-\infty}^{\infty}\frac{T_{\mathrm{eh}}}{T_{\mathrm{ec}}}\frac{n\Omega_{\mathrm{ceh}}}{\omega - n\Omega_{\mathrm{ceh}}}\left[W\left(\frac{\omega - n\Omega_{\mathrm{ceh}}}{k_{\|}(T_{\mathrm{eh}}/m_{\mathrm{e}})^{1/2}}\right) - 1\right]\Lambda_{\mathrm{n}}(\beta_{\mathrm{ec}})\right\} \tag{A.6}$$

Similarly to (A.3), we can derive this in terms of Z function as opposed to W

$$\chi_{\mathrm{e,ani}} = \frac{1}{k^2\lambda_{\mathrm{Deh}}^2}\left\{1 + \zeta_{\mathrm{eh,0}}\sum_{\mathrm{n}=-\infty}^{\infty} Z(\zeta_{\mathrm{eh,n}})\Lambda_{\mathrm{n}}(\beta_{\mathrm{ec}}) + \frac{(T_{\mathrm{eh}}/T_{\mathrm{ec}} - 1)}{k_{\|}\rho_{\mathrm{eh}}}\sum_{\mathrm{n}=-\infty}^{\infty} nZ(\zeta_{\mathrm{eh,n}})\Lambda_{\mathrm{n}}(\beta_{\mathrm{ec}})\right\} \tag{A.7}$$

Define the ring factor as $\alpha = T_{\mathrm{ec}}/T_{\mathrm{eh}}$. Note that in the hot ring distribution, the hot ring temperature T_{er} is the same as the hot temperature T_{eh} in the anisotropic distribution. Substituting (A.5) and (A.7) into (A.4), we get the final expression for the electron susceptibility for a velocity-space ring distribution discussed in Chapter 5.

$$\begin{aligned}\chi_{\mathrm{er}}(\omega, k) = \frac{1}{k^2\lambda_{\mathrm{Der}}^2}\Bigg\{1 &+ \frac{1}{1-\alpha}\zeta_{\mathrm{er,0}}\sum_{\mathrm{n}=-\infty}^{\infty}\Lambda_{\mathrm{n}}(\beta_{\mathrm{er}})Z(\zeta_{\mathrm{er,n}}) - \frac{\alpha}{1-\alpha}\zeta_{\mathrm{er,0}}\sum_{\mathrm{n}=-\infty}^{\infty}\Lambda_{\mathrm{n}}(\alpha\beta_{\mathrm{er}})Z(\zeta_{\mathrm{er,n}}) \\ &- \frac{1}{\omega/\Omega_{\mathrm{cer}}}\zeta_{\mathrm{er,0}}\sum_{\mathrm{n}=-\infty}^{\infty} n\Lambda_{\mathrm{n}}(\alpha\beta_{\mathrm{er}})Z(\zeta_{\mathrm{er,n}})\Bigg\}\end{aligned} \tag{A.8}$$

Appendix B

Velocity-space Ring Distribution Function

In this appendix, it is required to show, as stated in Appendix A, that

$$\chi_{\mathrm{e,ring}} = \frac{1}{1-\alpha}\chi_{\mathrm{e,iso}} - \frac{\alpha}{1-\alpha}\chi_{\mathrm{e,ani}} \tag{B.1}$$

This is equivalent to

$$f_{\mathrm{ring}}(v_\perp, v_\parallel) = \frac{1}{1-\alpha} f_{\mathrm{iso}}(v_\perp, v_\parallel) - \frac{\alpha}{1-\alpha} f_{\mathrm{ani}}(v_\perp, v_\parallel) \tag{B.2}$$

The velocity distribution functions for the isotropic, anisotropic, and ring distributions are

$$\begin{aligned}
f_{\mathrm{iso}}(v_\perp, v_\parallel) &= \frac{1}{\pi^{3/2} v_{\mathrm{th}}^3} \exp\left(\frac{-v_\parallel^2 - v_\perp^2}{v_{\mathrm{th}}^2}\right) && \text{(B.3)}\\
f_{\mathrm{ani}}(v_\perp, v_\parallel) &= \frac{1}{\pi^{3/2} v_{\mathrm{th}}} \frac{1}{v_{\mathrm{tc}}^2} \exp\left(\frac{-v_\parallel^2}{v_{\mathrm{th}}^2}\right) \exp\left(\frac{-v_\perp^2}{v_{\mathrm{tc}}^2}\right) && \text{(B.4)}\\
f_{\mathrm{ring}}(v_\perp, v_\parallel) &= \frac{1}{\pi^{3/2} v_{\mathrm{th}}} \frac{1}{(v_{\mathrm{th}}^2 - v_{\mathrm{tc}}^2)} \exp\left(\frac{-v_\parallel^2}{v_{\mathrm{th}}^2}\right) \left[\exp\left(\frac{-v_\perp^2}{v_{\mathrm{th}}^2}\right) - \exp\left(\frac{-v_\perp^2}{\alpha v_{\mathrm{th}}^2}\right)\right] && \text{(B.5)}
\end{aligned}$$

Considering that $\alpha = T_{\mathrm{ec}}/T_{\mathrm{eh}} = v_{\mathrm{tc}}^2/v_{\mathrm{th}}^2$, it can be easily verified they satisfy the relationship in equation (B.2).

The isotropic and anisotropic distribution functions given in (B.3) and (B.4) are normalized. In other words,

$$\int_0^{2\pi}\int_{-\infty}^{\infty}\int_0^{\infty} f_{\text{iso}}(v_\perp, v_\parallel)v_\perp dv_\perp dv_\parallel d\phi = 1 \tag{B.6}$$

$$\int_0^{2\pi}\int_{-\infty}^{\infty}\int_0^{\infty} f_{\text{ani}}(v_\perp, v_\parallel)v_\perp dv_\perp dv_\parallel d\phi = 1 \tag{B.7}$$

Thus from (B.2) we can have

$$\begin{aligned}
& \int_0^{2\pi}\int_{-\infty}^{\infty}\int_0^{\infty} f_{\text{ring}}(v_\perp, v_\parallel)v_\perp dv_\perp dv_\parallel d\phi \\
= & \int_0^{2\pi}\int_{-\infty}^{\infty}\int_0^{\infty} \left(\frac{1}{1-\alpha} f_{\text{iso}}(v_\perp, v_\parallel) - \frac{\alpha}{1-\alpha} f_{\text{ani}}(v_\perp, v_\parallel)\right) v_\perp dv_\perp dv_\parallel d\phi \\
= & \frac{1}{1-\alpha} - \frac{\alpha}{1-\alpha} \\
= & 1
\end{aligned} \tag{B.8}$$

This indicates that the ring distribution function given by (B.2) is normalized by choosing a proper set of coefficients.

Appendix C

1-D Particle-in-cell Electrostatic Plasma Simulation

In this appendix, we briefly discuss the one-dimensional particle-in-cell electrostatic plasma simulation program, generally known as ES1 ([*Birdsall and Langdon*, 1991]). One spatial dimension (x) is assumed and in the original version of ES1, two other velocities (v_x and v_y) are used. It should be noted that in our simulation of the four-wave decay process three velocities (v_x, v_y and v_z) have been used. But simplicity we only show the mathematical details using two velocities in this appendix. The whole plasma length (l) is equally divided into a number of grid cells (ng) which is required to be an integer power of two since FFT techniques are used. Thus, there are $ng + 1$ grid points. We generally use the index i to denote particles and the index j to denote grid cells or grid points. Figure (C.1) gives a view how the 1-D geometry is divided. The parameters dx is obviously equal to l/ng.

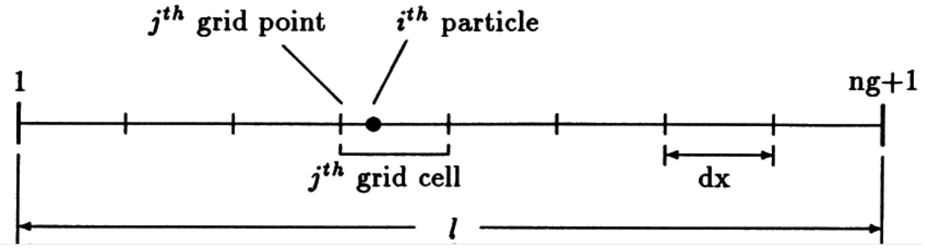

Figure C.1: Discretization of plasma length and naming of grids and particles in ES1.

The algorithm of ES1 is rather simple, as shown in Figure (C.2). The computation cycle consists of three major subroutines (MOVE, ACCEL, and FIELD) to accomplish the jobs in each box. After each cycle, the program advances to the next time step.

When the pre-defined total number of time steps (nt) is reached, the program ends and plots simulation histories for diagnostic purposes.

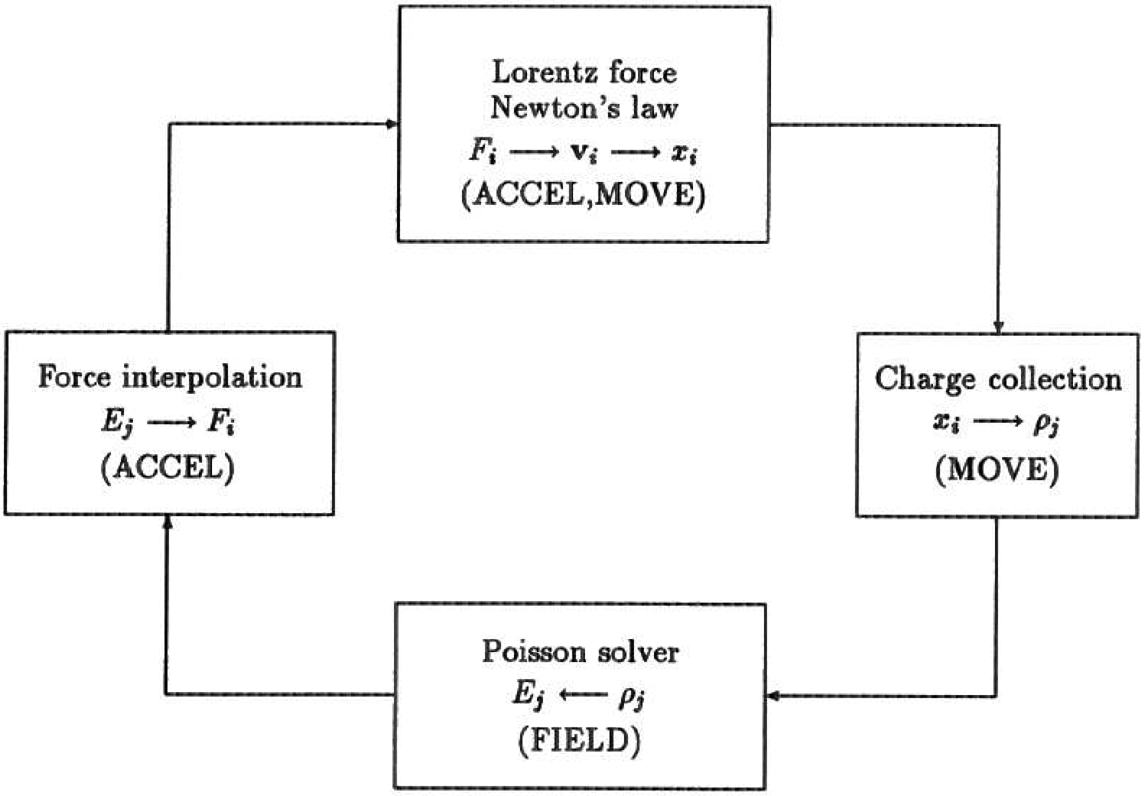

Figure C.2: A typical cycle, one time step, in a particle simulation. The particles are numbered i = 1, 2, ..., NP; the grid indices are j.

Three equations, namely Newton's law, Lorentz force equation, and Poisson's Equation, are used in the computation loop.

- Newton's second law : $\mathbf{F} = \mathrm{m}\frac{\mathrm{d}\mathbf{v}}{\mathrm{dt}}$, $\mathbf{v} = \frac{\mathrm{dx}}{\mathrm{dt}}$
- Lorentz force equation : $\mathbf{F} = \mathrm{q}(\mathbf{E} + \mathbf{v} \times \mathbf{B})$
- Poisson's Equation : $\bigtriangledown^2\phi = -\frac{\rho}{\epsilon_0}$

Of course, we only keep the spatial dimension x in ES1. However, the velocities other than x-direction certainly have contribution to the force acting upon particles through the Lorentz force equation. Therefore, we have to keep more than one velocity when the background magnetic field is nonzero. The first two equations are solved numerically using the center difference method, while the Poisson's equation is solved by fast Fourier Transform (FFT). All of them will be discussed in more detail in the following sections.

C.1 Integration of the equations of motion

The equations of motion are composed of Newton's second law and Lorentz force equation. In Newton's second law, if we want to get a numerical solution to the position x, we have to integrate twice. Finite-difference methods are used in ES1 to calculate the velocities and position due to its simplicity and acceptable accuracy. Using the leap-frog method, as shown in Figure (C.3), these equations are replaced by

$$m\frac{\mathbf{v}_{\text{new}} - \mathbf{v}_{\text{old}}}{\Delta \text{t}} = \mathbf{F}_{\text{old}} \tag{C.1}$$

$$\frac{\text{x}_{\text{new}} - \text{x}_{\text{old}}}{\Delta \text{t}} = \text{v}_{\text{x,new}} \tag{C.2}$$

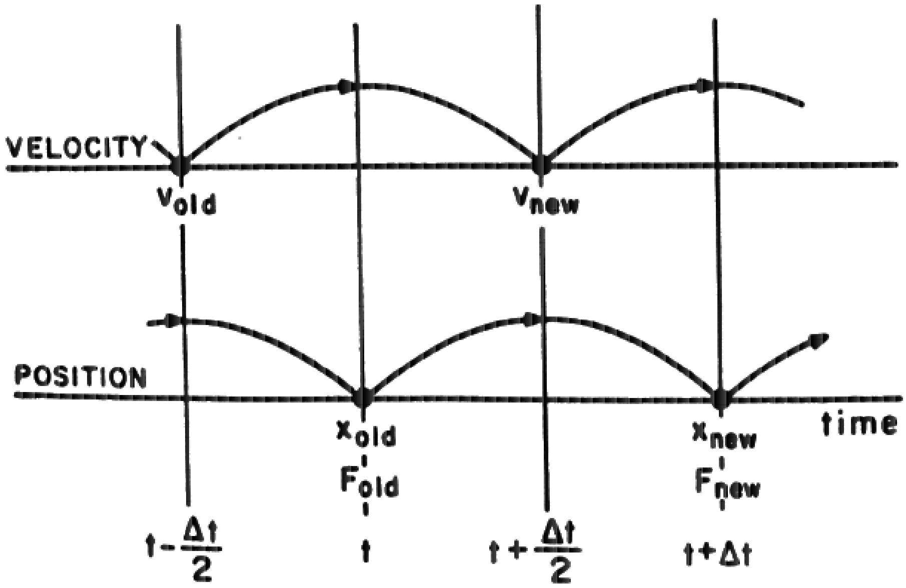

Figure C.3: Sketch of leap-frog integration method showing time-centering of force **F** while advancing v, and of v while advancing x.

The leap-frog method has been found very accurate. When $\omega_{pe}\Delta t \leq 2$, where ω_{pe} is the plasma frequency, there is no amplitude error in the simulation of high-frequency plasma oscillations.

When the magnetic field is present in the simulation, the computation of the gyromotion of particles needs a particular numerical scheme to be compatible with the linear motion. This scheme is known as the Boris mover which uses two halfaccelerations and one rotation in between. The overall motion of a particle in a time step is,

1. First half-acceleration:

$$\begin{aligned} v_x(t^{'}) &= v_x(t-\frac{\Delta t}{2})+\frac{q}{m}E_x(t)\frac{\Delta t}{2} \\ v_y(t^{'}) &= v_y(t-\frac{\Delta t}{2}) \end{aligned} \tag{C.3}$$

2. Rotation:

$$\begin{pmatrix} v_x(t^{"}) \\ v_y(t^{"}) \end{pmatrix} = \begin{pmatrix} cos(\Omega\Delta t) & sin(\Omega\Delta t) \\ -sin(\Omega\Delta t) & cos(\Omega\Delta t) \end{pmatrix} \begin{pmatrix} v_x(t^{'}) \\ v_y(t^{'}) \end{pmatrix} \tag{C.4}$$

3. Second half-acceleration:

$$\begin{aligned} v_x(t+\frac{\Delta t}{2}) &= v_x(t^{"})+\frac{q}{m}E_x(t)\frac{\Delta t}{2} \\ v_y(t+\frac{\Delta t}{2}) &= v_y(t^{"}) \end{aligned} \tag{C.5}$$

where $t^{'}$ and $t^{"}$ are dummy variables. The angle of rotation, measured with respect to v_x-direction in counterclockwise sense, is $\Delta\theta = -\Omega\Delta t$. Note that the cyclotron frequency Ω carries the signs of q and B_0. The leap-frog method and Boris mover are implemented in the subroutines MOVE and ACCEL respectively. In our ES1 simulation for the four-wave process, the Boris scheme is extended to a more complicated form with three velocities.

One complication arises at t=0 when the initial conditions, $x(0)$ and $\mathbf{v}(0)$, are given at the same time. The main loop runs with x leading $\mathbf{v}$ by $\Delta t/2$. Hence at the start, $\mathbf{v}(0)$ is moved backward to $\mathbf{v}(-\Delta t/2)$ by running the Boris scheme backward. This is done by the subroutine SETV.

C.2 Poisson's Equation

In ES1 program, the fast Fourier Transform (FFT) is used to solve the Poisson's Equation for its computational efficiency for large number grid cells. The general algorithm of Poisson solver using FFT is,

$$\rho(x) \underset{FFT}{\longrightarrow} \bar{\rho}(k) \underset{k^{-2}}{\longrightarrow} \bar{\phi}(k) \underset{IFFT}{\longrightarrow} \phi(x) \underset{\nabla\phi}{\longrightarrow} E_x(x) \tag{C.6}$$

where $\bar{\rho}(k)$ and $\bar{\phi}(k)$ are FFT of $\rho(x)$ and $\phi(x)$ respectively. In the transform domain, the potential is easily obtained by,

$$\bar{\phi}(k) = \frac{\bar{\rho}(k)}{\epsilon_0 k^2} \tag{C.7}$$

Then using inverse fast Fourier Transform (IFFT), we can get back the potential in x. By the center difference method, the electric field $E_x(x)$ is obtained.

C.3 Particle and force weighting

It is necessary to calculate the charge density on the discrete grid points from the continuous particle positions and (after the fields are obtained), to calculate the force at the particles from the fields on the grid points. These calculations are called weighting, which establishes a connection between grid and particle quantities. Usually it is desirable to use the same weighting in both density and force calculations in order to avoid a self-force.

A first-order weighting as shown in Figure (C.4) is used in our ES1 code. It smoothes the density and field fluctuations, which is less noisy than the zero-order, but requires additional computation in accessing two grid points for each particle, twice per step. The weighting is actually a linear interpolation. The charge of a particle is proportionally divided to its nearest grid points, Mathematically, if a particle is situated in the j^{th} grid cell, then the charge assignments to the j^{th} and $(j+1)^{th}$ grid points are,

$$q_j = q\left(1 - \frac{x_i - X_j}{\Delta x}\right) = q\frac{X_{j+1} - x_i}{\Delta x} \tag{C.8}$$

$$q_{j+1} = q\frac{x_i - X_j}{\Delta x} \tag{C.9}$$

where $X_j = (j-1)\Delta x$ is the position of the j^{th} grid point. Note that the sum of q_j and q_{j+1} equals the particle charge q. The field weighting operates in the same manner. This is,

$$E(x_i) = \frac{X_{j+1} - x_i}{\Delta x}E_j + \frac{x_i - X_j}{\Delta x}E_{j+1} \tag{C.10}$$

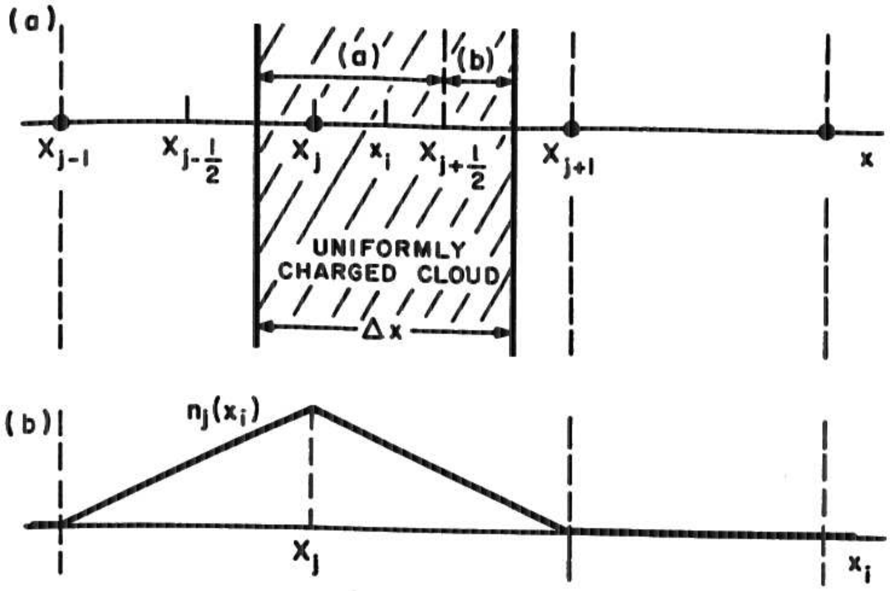

Figure C.4: Schematic diagram for first-order particle weighting. The nominal finite-size charged particle is one cell wide with center at x_i.

Appendix D

Program Listing

This FORTRAN program listing solves dispersion relation for ring-plasma instabilities perpendicular to a magnetic field numerically. It was used in various forms in Chapter 5.

```
c=========================================================================c
c                                                                         c
c OBJECTIVE  : Solves dispersion relation for ring-plasma velocity-space  c
c              instabilities perpendicular to a magnetic field            c
c                                                                         c
c NOTES      : 1. Subtracted Maxwellians are used to construct the ring.c
c                2. Cyclotron frequency normalized to 1.                  c
c                                                                         c
c VARIABLES  :                                                            c
c                                                                         c
c wuh           -- upper hybrid frequency                                 c
c rpercent      -- percent of ring to background electron density         c
c rtemp         -- ratio of ring to background electron temperature       c
c alpha         -- ratio of cool to hot ring electron temperature (<1)    c
c theta         -- propagation angle from perpendicular to B              c
c w             -- frequency (complex)                                    c
c wr            -- real part of w                                         c
c gamma, gammas -- growth rate (imaginary part of w) and sorted version   c
c kp,kz,kmag    -- perpendicular,parallel component and magnitude of k    c
c                                                                         c
c=========================================================================c

      complex*16 w, dw, f, df
      complex*16 we1, we2, wl, wh, dwo
      complex*16 fl, fh, dfl, dfh
      complex ws, dws ,st(4001)
      real kp(4001),kmag(4001),kz, kp2, kmax, kmin,step,kk,start
      real wr(4001), gamma(4001), wrs(4001),
     .gammas(4001),temp1,temp2
```

```
      common /plasma/ wpeb,wpi
      common /ring/ wper,rtemp,alpha
      real memi, mime,number

      integer iargc, nkay
      real wuh, rpercent, rtemp, alpha, theta
      character*14 commandLine
      character*15 filename

      print *, '======================================================='
      print *, '=                                                     ='
      print *, '=             INPUT PARAMETERS IN ORDER               ='
      print *, '=                                                     ='
      print *, '=   wuh      : normalized upper hybrid frequency      ='
      print *, '=   rpercent : ring density percent                   ='
      print *, '=   rtemp    : normalized hot ring component temp     ='
      print *, '=   alpha    : normalized cool ring component temp    ='
      print *, '=   theta    : Angle between k and kp                 ='
      print *, '=                                                     ='
      print *, '======================================================='

c=====================================================================c
c                                                                     c
c     TYPICAL INPUT PARAMETERS (4th harmonic)                         c
c                                                                     c
c  for krho = .5                                                      c
c                                                                     c
c  wuh= 4.01, rpercent = .01, rtemp = 576, alpha = .5, theta= 0.0001  c
c                                                                     c
c  wuh= 4.01, rpercent = .01, rtemp = 576, alpha = .5, theta= 0.01    c
c                                                                     c
c=====================================================================c

      numargs = iargc()
      write(6,*) 'number of input parameters is : ', numargs

      call getarg(1,commandLine)
      read (commandLine,*) wuh
      call getarg(2,commandLine)
      read (commandLine,*) rpercent
      call getarg(3,commandLine)
      read (commandLine,*) rtemp
      call getarg(4,commandLine)
      read (commandLine,*) alpha
      call getarg(5,commandLine)
      read (commandLine,*) theta
      call getarg(6,commandLine)
      read (commandLine,*) nkay
      call getarg(7,filename)
```

```
      write(6,*) 'wuh : ', wuh, ' rpercent : ', rpercent
      write(6,*) 'rtemp : ', rtemp, 'alpha : ', alpha
      write(6,*) 'theta : ', theta , ' naky : ', naky
      write(6,*) 'filename : ', filename

      mime=400
      kmin=0.002
      kmax=1.0
      start=0.1
      step=0.001

      open( UNIT = 22, FILE = filename, STATUS='NEW')

c     Maximum number of iteration
      maxit = 20
c     Number of bisection
      nbisect=10

c     Number of k parameter

c      nkay =2000

c      print *, 'Input nkay :'
c      read(6,*) nkay

      wacc = 1.e-9
c     Initial value of maximum growth rate
      gmax = 0.0

c
c     Calculate gamma for all kprho in the desired range, typical (0.0,1.0)
c

c      print *, '******************************************************'

c      print *,'Enter the range for the bisection,  mime and vosc: '
c      read(6,*) range,mime,vosc

      range=4

      kk=1
      memi  = 1./mime
      wpe = sqrt(wuh**2-1)
      wpi   = wpe*sqrt(memi)
      wlh   = sqrt(memi)
      ppercent = 1. - rpercent
      wpeb = sqrt(ppercent)*wpe
      wper = sqrt(rpercent)*wpe

c Bernstein range for 4th harmonic
```

```
c      we1 = (3.500,1e-6)
c      we2 = (3.999,1e-6)

c Works better for large angle
c      we1 = (3.5000,1e-4)
c      we2 = (3.9999,1e-4)

c Upper hybrid range for 4th harmonic

      we1 = (4.001,1e-6)
      we2 = (4.500,1e-6)

 555  do 1 i=1,nkay

      j = nkay+1-i

      kp(j)   = (i-1)*(kmin-kmax)/(nkay-1) + kmax
      kz      = kp(j)*tan(theta*3.141592654/180)
      kp2     = kp(j)**2
      kmag(j) = sqrt(kp2+kz**2)
      vmagn   = kmag(j)

c==================================================================c
c                                                                  c
c    ITERATION SCHEME -- Use bisection to get started off from     c
c                        kmax, then use Newton Raphson             c
c                                                                  c
c==================================================================c

      if (i.le.range) then

      call disp(we1,kp2,kz,fl,dfl)
      call disp(we2,kp2,kz,fh,dfh)
      flr = dreal(fl)
      fhr = dreal(fh)

      if((flr.gt.0.0.and.fhr.gt.0.0).or.(flr.lt.0.0.and.fhr.lt.0.0))
     .then
      print *, 'No root is bracketed !   ', 'k=', kmag(nkay+1-i)
      print *, 'we1=', we1, 'we2=', we2
      print *, 'fl=', fl, 'fh=', fh
      pause

      goto 1000

      endif

      if(flr.lt.0.0) then
      wl=we1
      wh=we2
```

```
      else
      wh=we1
      wl=we2
      endif


      w=0.5d0*(we1+we2)
      dwo=wh-wl
      dw=dwo

      endif

      if (i.gt.range) w=ws
      call disp(w,kp2,kz,f,df)

      if(i.le.range) then

      do 11 k=1,maxit

      if(k.le.nbisect) then
      dwo=dw
      dw=0.5d0*(wh-wl)
      w = wl + dw
      else
      dwo=dw
      dw = f/df
      w = w - dw
      endif

      ws=w
      dws=dw

      if(aimag(ws).gt.dimag(we2)) then
      goto 1000
      endif

      if(cabs(dws).lt.1.e-6*cabs(ws)) go to 3
      call disp(w,kp2,kz,f,df)

      if(dreal(f).lt.0.0) then
      wl=w
      else
      wh=w
      endif

 11   continue

      endif

      if(i.gt.range) then
```

```
      do 511 k=1,maxit

      dwo=dw
      dw = f/df
      w = w - dw
      ws=w
      dws=dw

      if(cabs(dws).lt.1.e-6*cabs(ws)) go to 3
      call disp(w,kp2,kz,f,df)

 511   continue

      endif

 3    wrmax= amax1(wrmax,real(ws))
      gmax = amax1(gmax,aimag(ws))

      wr(j)    = real(ws)

c      print *, 'i=',i,'  wr(i)=',wr(i),'  kp(i)=',kp(i)
c      pause

 1    gamma(j) = aimag(ws)

c==================================================================c
c                                                                  c
c             This is the initial guess estimation                 c
c                                                                  c
c==================================================================c

 1000 if(i.lt.15) then

      if(kmin.gt.kmax) then
      kmin=kmin-step
      endif

      if(kmin.lt.kmax) then
      if(kk.eq.1) then
      kmin=start
      kk=2
      endif
      kmin=kmin+step
      kk=kk+1
      endif

      goto 555

      endif
```

```
      if(kmax.gt.kmin) then
      xmax=kmax
      xmin=kmin
      else
      xmax=kmin
      xmin=kmax
      endif

      i=i-1

c==============================================================c
c                                                              c
c  Calculate the frequencies of down-shifted Bernstein waves   c
c  and up-shifted upper hybrid waves                           c
c                                                              c
c==============================================================c

      do 133 i=1,nkay-1
      gamma(i)=gamma(i)/wlh
      wr(i)=wr(i)/wlh
      wrs(i)=wr(i)
 133  gammas(i)=gamma(i)


c========================== Sort the arrays here ==================c

      do 166  i=1,nkay-2

      temp1=wrs(i)
      temp2=gammas(i)

      do 166  j=i+1,nkay-1

      if(wrs(j).lt.temp1) then

      temp1=wrs(j)
      wrs(j)=wrs(i)
      wrs(i)=temp1

      temp2=gammas(j)
      gammas(j)=gammas(i)
      gammas(i)=temp2

      endif

 166  continue

      write(22,*) '% wuh = ',wuh,' rpercent = ',rpercent,
     .            ' rtemp = ',rtemp
```

```
      write(22,*) '% alpha = ',alpha,' theta = ',theta
      write(22,*) '% we1 = ', we1
      write(22,*) '% we2 = ', we2
      write(22,*) '% gmax/wlh = ', gmax/wlh

      do 666 is=1,nkay-1
 666  write(22,*) kmag(is), wr(is), gamma(is), wrs(is)

      scale=sqrt(1+mime*sin(theta*3.14159/180)**2)

c==================================================================c
c                                                                  c
c              Plot results with NCAR graphics                     c
c                                                                  c
c==================================================================c

      call OPNGKS

      call agsetf('X/MAXIMUM.',  xmax)
      call agsetf('X/MINIMUM.',   0.0)
      call agsetf('Y/MAXIMUM.',  90.0)
      call agsetf('Y/MINIMUM.',  70.0)
      call anotat('kmag*rho$','wr/wlh$',0,0,0,0)
      call ezxy(kmag,wr,i-1,'Real Frequency$')

      call agsetf('X/MAXIMUM.',  xmax)
      call agsetf('X/MINIMUM.',  0.0)
c      call agsetf('Y/MAXIMUM.',   gmax/wlh*1.4)
      call agsetf('Y/MAXIMUM.',   0.500)
      call agsetf('Y/MINIMUM.',   0.000)
      call anotat('kmag*rho$','gamma$',0,0,0,0)
      call ezxy(kmag,gamma,i-1,'Growth Rate$')

      call agsetf('X/MAXIMUM.',  scale*90.0)
      call agsetf('X/MINIMUM.',  scale*70.0)
c      call agsetf('Y/MAXIMUM.',   gmax/wlh*1.4)
      call agsetf('Y/MAXIMUM.',   0.500)
      call agsetf('Y/MINIMUM.',   0.000)
      call anotat('wr/wlh$','gamma$',0,0,0,0)
      call ezxy(wrs,gammas,i-1,'Growth Rate$')

 313  continue

      call CLSGKS

c==================================================================c
c                                                                  c
c                        RESULT OUTPUT                             c
c                                                                  c
c==================================================================c
```

```
      print *, ' '
      print *, ' '
      print *, '====================== Result ===================='
      print *, i, ' points calculated'
      print *, 'Maximum Growth Rate is = ', gmax/wlh
      print *, 'Maximum wr is = ', wrmax
      print *, 'kmin=',xmin,'  kmax=',xmax,'theta= ',theta
      stop
      end
c
c=====================================================================c
c
      subroutine disp(w,kp2,kz,f,df)
c
c  Calculates the dispersion function (f) and its derivative (df)
c
c=====================================================================c
c
      complex*16 w
      complex*16 ew,dew
      complex*16 f, df
      real kp2, kz

      call eps (w,kp2,kz,ew,dew)

      f =  ew
      df = dew

      return
      end
c
c=====================================================================c
c
      subroutine eps(w,kp2,kz,e,de)
c
c  Calculates the full dielectric response (and its frequency derivative)
c  from electron and ion susceptibilities assuming an electron ring
c  velocity distribution component as well as a Maxwellian background
c  electron component. The ring electron distribution is constructed
c  from subtracted anisotropic Maxwellian distributions. The dielectric
c  response is given by e = 1 + xie +xieh + xiec + xii.
c
c=====================================================================c
c
      complex*16 w
      complex*16 e, de, xie, dxie, xii, dxii
      complex*16 xieh, dxieh, xiec, dxiec
      complex*16 rc(2,2)
      real kp2,kz,km,kzh,kmh,kzc,kmc
      common /plasma/ wpeb,wpi
```

```
      common /ring/ wper,rtemp,alpha

      complex*16 B(8),C(8)
      complex*16 v,v1,v2,SUM,SUM1,SUM2,SUMder,SUMder1,SUMder2
      complex*16 Ye , Zm , Zder
      complex*16 Yeh, Zmh, Zderh
      complex*16 Yec, Zmc1, Zmc2, Zderc1, Zderc2

C RESIDUES FOR PADE APPROXIMANT
      DATA B/(-1.734012457471826d-2,-4.630639291680322d-2),
     B       (-1.734012457471826d-2, 4.630639291680322d-2),
     B       (-7.399169923225014d-1, 8.395179978099844d-1),
     B       (-7.399169923225014d-1,-8.395179978099844d-1),
     B       ( 5.840628642184073d0 , 9.536009057643667d-1),
     B       ( 5.840628642184073d0 ,-9.536009057643667d-1),
     B       (-5.583371525286853d0 ,-1.120854319126599 d1),
     B       (-5.583371525286853d0 , 1.120854319126599 d1)/,
C POLES FOR PADE APPROXIMANT
     C    C/ ( 2.237687789201900d0 ,  -1.625940856173727d0),
     C       (-2.237687789201900d0 ,  -1.625940856173727d0),
     C       ( 1.465234126106004d0 ,  -1.789620129162444d0),
     C       (-1.465234126106004d0 ,  -1.789620129162444d0),
     C       ( .8392539817232638d0 ,  -1.891995045765206d0),
     C       (-.8392539817232638d0 ,  -1.891995045765206d0),
     C       ( .2739362226285564d0 ,  -1.941786875844713d0),
     C       (-.2739362226285564d0 ,  -1.941786875844713d0)/

      rrtemp = sqrt(rtemp)
      a1 = 1.0d0/(1.0d0-alpha)
      a2 = alpha*a1
      anis = 1.0d0/a2

c==================================================================c

c     background electrons

      km    =    sqrt(kp2+kz**2)
      be    =    0.5d0*kp2
      Zm    =   (0.0d0,0.0d0)
      Zder  =   (0.0d0,0.0d0)

c     hot ring electrons

      kzh    =   kz*rrtemp
      kmh    =   km*rrtemp
      beh    =   be* rtemp
      Zmh    =   (0.0d0,0.0d0)
      Zderh  =   (0.0d0,0.0d0)

c     cool ring electrons
```

```
      kzc    =   kzh
      kmc    =   kmh
      bec    =   beh*alpha
      Zmc1   =   (0.0d0,0.0d0)
      Zmc2   =   (0.0d0,0.0d0)
      Zderc1 =   (0.0d0,0.0d0)
      Zderc2 =   (0.0d0,0.0d0)

c
c    Construct infinite Bessel function sums in susceptibilities
c

      DO 1 I=1,8

c     BACKGROUND ELECTRONS

      Ye     = w - C(I)*kz
      v      = B(I)*kz*be/Ye**2
      call ryla(Ye,be,rc)
      SUM    = v*(rc(1,1) + Ye/be)
      Zm     = SUM + Zm
      SUMder = v*(rc(2,1)/Ye + 1.0d0/be - 2.0d0*(rc(1,1)/Ye + 1.0d0/be))
      Zder   = SUMder  +   Zder

c     HOT RING ELECTRONS

      Yeh    = w - C(I)*kzh
      v      = B(I)*kzh*beh/Yeh**2
      call ryla(Yeh,beh,rc)
      SUM    = v*(rc(1,1) + Yeh/beh)
      Zmh    = SUM + Zmh
      SUMder = v*(rc(2,1)/Yeh + 1.0d0/beh - 2.0d0*(rc(1,1)/Yeh +
     .1.0d0/beh))
      Zderh  = SUMder + Zderh

c     COOL RING ELECTRONS

      Yec     = w - C(I)*kzc
      v1      = B(I)*kzc*bec/Yec**2
      v2      = B(I)*kzc*bec/Yec
      call ryla(Yec,bec,rc)
      SUM1    = v1*(rc(1,1) + Yec/bec)
      SUM2    = v2*rc(1,1)
      Zmc1    = SUM1 + Zmc1
      Zmc2    = SUM2 + Zmc2
      SUMder1 = v1*(rc(2,1)/Yec + 1.0d0/bec - 2.0d0*(rc(1,1)/Yec +
     .1.0d0/bec))
      SUMder2 = v2*(rc(2,1)/Yec - rc(1,1)/Yec)
      Zderc1  = SUMder1 + Zderc1
```

```
      Zderc2  = SUMder2 + Zderc2

 1    CONTINUE

c
c     Construct final susceptibilities
c

c     BACKGROUND ELECTRONS

      xie = 2.0d0*(wpeb/km)**2*(1.0d0+(w/kz)*Zm)
      dxie = 2.0d0*(wpeb/km)**2*(w*Zder+Zm)/kz

c     HOT RING ELECTRONS

      xieh = 2.0d0*(wper/kmh)**2*(1.0d0+(w/kzh)*Zmh)
      dxieh = 2.0d0*(wper/kmh)**2*(w*Zderh+Zmh)/kzh

c     COOL RING ELECTRONS

      xiec = 2.0d0*(wper/kmc)**2*(1.0d0+(w/kzc)*Zmc1+(anis/kzc)*Zmc2)
      dxiec = 2.0d0*(wper/kmc)**2*(w*Zderc1+Zmc1+anis*Zderc2)/kzc

c
c  Construct final dielectric function and derivative
c

      e  = 1.0d0 +  xie + a1* xieh - a2* xiec
      de = dxie + a1*dxieh - a2*dxiec

      return
      end

C
CCCCCCCCCCCCCCCCCCCCCCCCCCCCCCCCCCCCCCCCCCCCCCCCCCCCCCCCCCCCCCCCCCCCCCCC
C
      SUBROUTINE RYLA(Y,AL,RC)
C
C SUBROUTINE RYLA CALCULATES THE INFINITE BESSEL SUM TERMS IN HOT
C MAGNETIZED PLASMA DISPERSION RELATIONS. THE NUMERICAL CALCULATION
C TECHNIC DEPENDS ON THE KRHO REGIME.
C
CCCCCCCCCCCCCCCCCCCCCCCCCCCCCCCCCCCCCCCCCCCCCCCCCCCCCCCCCCCCCCCCCCCCCCC
C
      complex*16 Y,RC(2,2)
C
C           ****  CHOOSE HETHOD OF EVALUATION ****
C
      IF(AL.LT.4.) GOTO 1
      AY=CDABS(Y)
```

```
      IF(AY**2.GT.75.*AL) GOTO 1
      IF(AY.GT.40.+AL/3) GOTO 1
      IF(3.*(AL-10.).GT.AY.AND.AY**2.LT.15.*AL) GOTO 3
C
C          ******** NUMERICAL INTEGRATION ********
C
      CALL RINT(Y,AL,RC)
      RETURN
C
C        ******** TAYLOR SERIES ********
C
    1 CALL RTAY(Y,AL,RC)
      RETURN
C
C         ******** ASYMPTOTIC SERIES ********
C
    3 CALL RASY(Y,AL,RC)
      RETURN
      END
C
CCCCCCCCCCCCCCCCCCCCCCCCCCCCCCCCCCCCCCCCCCCCCCCCCCCCCCCCCCCCCCCCCCCCCCCCC
C
      SUBROUTINE RASY(Y,AL,RC)
C
C USE ASYMPTOTIC SERIES FOR SUFFICIENTLY LARGE KRHO
C
CCCCCCCCCCCCCCCCCCCCCCCCCCCCCCCCCCCCCCCCCCCCCCCCCCCCCCCCCCCCCCCCCCCCCCCC
C
      complex*16 Y,Y2,COT,P,PY,PP,PPY,PN,PYN,QN,QYN,RC(2,2)

      PI=3.14159265358979
      Y2=Y*Y
      COT=COS(PI*Y)/SIN(PI*Y)
*                 1.E99 IS TOO BIG FOR S/370 HARDWARE. SET TO LARGEST
*                 POSSIBLE FOR IBM MACHINES
*     C=1.E99
      C = 7.2E35
      PN=-Y/AL
      PYN=PN
      A=1./(AL*SQRT(2.*PI*AL))
      QN=PI*Y2*COT*A
      QYN=QN*(2.-Y*PI*COT)-Y*PI**2*Y2*A
C
      P=PN+QN
      PY=PYN+QYN
      PP=-PN-1.5*QN
      PPY=-PYN-1.5*QYN
      AY=CDABS(Y)+2.
C
      DO 4 N=1,100
```

```
      M=N-1
      PYN=(PYN*(M*M-Y2)-2.*Y2*PN)/((2*M+1)*AL)
      PN =PN*(M*M-Y2)/((2*M+1)*AL)
      QYN=(QYN*((M+.5)**2-Y2)-2.*Y2*QN)/(2.*N*AL)
      QN =QN*((M+.5)**2-Y2)/(2.*N*AL)
      IF(M.LT.AY) GOTO 3
      C=N*(CDABS(PN)+CDABS(QN))
      IF(C.LE.1.E-7*ABS(PP)) GOTO 5
      IF(C.GE.T) GOTO 5
    3 P  =P  + PN  + QN
      PY =PY + PYN + QYN
      PP =PP -(N + 1.)*PN -(N +1.5)*QN
      PPY=PPY-(N + 1.)*PYN-(N +1.5)*QYN
    4 T=C
C
    5 RC(1,1)=P + PN + QN
      RC(2,1)=PY+ PYN+ QYN
      RC(1,2)=PP+P
      RC(2,2)=PPY+PY
      RETURN
      END
C
CCCCCCCCCCCCCCCCCCCCCCCCCCCCCCCCCCCCCCCCCCCCCCCCCCCCCCCCCCCCCCCCCCCCCCCC
C
      SUBROUTINE RINT(YY,AL,RC)
C
C USE NUMERICAL INTEGRATION FOR KRHO ON THE ORDER OF 1
C
CCCCCCCCCCCCCCCCCCCCCCCCCCCCCCCCCCCCCCCCCCCCCCCCCCCCCCCCCCCCCCCCCCCCCCCC
C
      complex*16 RC(2,2),Y,YY,COT,D,EXF,F,H,O,P,R,RY,RP,RPY,S
      real*8 A(16), W(16)
C       ABSCISSAS FOR GAUSSIAN INTEGRATION
      DATA A/               -.989400934991649d0,-.944575023073232d0,
     D -.865631202387831d0, -.755404408355003d0,-.617876244402643d0,
     D -.458016777657227d0, -.281603550779258d0,-.095012509837637d0,
     D                       .989400934991649d0, .944575023073232d0,
     D  .865631202387831d0,  .755404408355003d0, .617876244402643d0,
     D  .458016777657227d0,  .281603550779258d0, .095012509837637d0/,
     D   W /                 .027152459411754d0, .062253523938647d0,
     D  .095158511682492d0,  .124628971255533d0, .149595988816576d0,
     D  .169156519395002d0,  .182603415044923d0, .189450610455068d0,
     D                       .027152459411754d0, .062253523938647d0,
     D  .095158511682492d0,  .124628971255533d0, .149595988816576d0,
     D  .169156519395002d0,  .182603415044923d0, .189450610455068d0/,
     D PI/3.14159265358979d0/
C
      CALL ZEROC2( RC, 1, 2, 1, 2 )
      IF(REAL(YY).LT.0.) THEN
         Y=-YY
```

```
         SIG=-1.
      ELSE
         Y=YY
         SIG=1.
      END IF
      YA=DIMAG(Y)
      YR=REAL(Y)
      UL=PI-2.8*Y/(36.+Y)
      COT=COS(PI*Y)/SIN(PI*Y)
      D=PI*(1.+COT**2)
      C=YR/AL
      XO=LOG(C+SQRT(1.+C**2))
C
      DO 10 I=1,16
      X=UL/2.*(1.+A(I))
      Z=SIN(X)
      C=COS(X)
      G=YR/AL*X/Z
      T=SQRT(1.+G**2)
      B=LOG(G+T)
      G=(1./X-C/Z)*G/T
      T=AL*(T*C-1.)
      Z=EXP(X*YA)
      C=.5*(Z+1./Z)
      S=(0.,.5)*(Z-1./Z)
      F=COT+G
      H=1.-G*COT
      EXF=EXP(T-Y*B)
      O=B*C+X*S
      P=X*C-B*S
      XY=X*YR
      R=(F*C+H*S)*EXF
      RY=(F*O-H*P+D*(C-G*S))*EXF
      RP=((F*T-H*XY)*C+(H*T+F*XY)*S)*EXF
      RPY=(F*(T*O-XY*P)-H*(T*P+XY*O)+((T+XY*G)*C-(G*T-XY)*S)*D)*EXF
C
      X=XO/2.*(1.+A(I))
      Z=EXP(X)
      C=(Z+1./Z)/2.-1.
      P=EXP(AL*C-Y*X)
      RC(1,1)=RC(1,1)+W(I)*(UL*R+XO*P)
      RC(2,1)=RC(2,1)-W(I)*(UL*RY+XO*X*P)
      RC(1,2)=RC(1,2)+W(I)*(UL*RP+XO*AL*C*P)
      RC(2,2)=RC(2,2)-W(I)*(UL*RPY+XO*AL*X*C*P)
   10 CONTINUE
C
      O=Y/AL
      P=Y**2/2.
      RC(1,1)=O*(Y*RC(1,1)/2.-1.)*SIG
      RC(2,1)=2.*RC(1,1)+O*(P*RC(2,1)+1.)*SIG
```

```
      RC(1,2)=Y*O*RC(1,2)/2.*SIG
      RC(2,2)=2.*RC(1,2)+O*P*RC(2,2)*SIG
      END
C
CCCCCCCCCCCCCCCCCCCCCCCCCCCCCCCCCCCCCCCCCCCCCCCCCCCCCCCCCCCCCCCCCCCCC
C
      SUBROUTINE RTAY(Y,AL,RC)
C
C USE TAYLOR SERIES FOR SUFFICIENTLY SMALL KRHO
C
CCCCCCCCCCCCCCCCCCCCCCCCCCCCCCCCCCCCCCCCCCCCCCCCCCCCCCCCCCCCCCCCCCCCC
C
      complex*16 Y,Y2,RC(2,2),PN,PYN,COT

      Y2=Y*Y
   10 PN=Y/(Y2-1.)
      PYN=-Y*(Y2+1.)/(Y2-1.)**2
      RC(1,1)=PN
      RC(1,2)=PN
      RC(2,1)=PYN
      RC(2,2)=PYN
C
      DO 1 I=2,100
      COT=(2*I-1)/(Y2-I**2)*AL
      PYN=COT*(PYN-2.*Y2/(Y2-I**2)*PN)
      PN=COT*PN
      RC(1,1)=RC(1,1)+PN
      RC(2,1)=RC(2,1)+PYN
      RC(1,2)=RC(1,2)+I*PN
      RC(2,2)=RC(2,2)+I*PYN
      T=CDABS(PN)*1.E8
      IF(T.LT.CDABS(RC(1,1))) GOTO 2
    1 CONTINUE
    2 CONTINUE
      END
C
CCCCCCCCCCCCCCCCCCCCCCCCCCCCCCCCCCCCCCCCCCCCCCCCCCCCCCCCCCCCCCCCCCCCCCC
C
      SUBROUTINE ZEROC2( ARRAY, LBD1, UBD1, LBD2, UBD2 )
C
C SIMPLE ROUTINE FOR ZEROING COMPLEX ARRAYS
C
CCCCCCCCCCCCCCCCCCCCCCCCCCCCCCCCCCCCCCCCCCCCCCCCCCCCCCCCCCCCCCCCCCCCCC
C
*     .... ARGUMENTS
      INTEGER LBD1, UBD1, LBD2, UBD2
      complex*16 ARRAY( LBD1 : UBD1,  LBD2 : UBD2 )
*     .... VARIABLES
      INTEGER I1, I2
      DO 20 I2 = LBD2, UBD2
```

```
         DO 10 I1 = LBD1, UBD1
            ARRAY( I1, I2 ) = ( 0.0D0, 0.0D0 )
   10    CONTINUE
   20 CONTINUE
      END
```

References

Antani, S. N., N. N. Rao, and D. J. Kaup, Direct conversion of ordinary mode into upper hybrid waves by density irregularities in the ionosphere, *Geophys. Res. Lett., 18*, 2285-2288, 1991.

Birdsall, C. K., and A. B. Langdon, *Plasma Physics via Computer Simulation,* Adam Hilger, New York, 1991.

Bud'ko, N. I., and V. V. Vas'kov, Four-wave decay of a powerful radio wave under multiple electronic gyroresonance conditions, *Geomagn. Aeron.,* Engl. Transl., *32*, 63-70, 1992.

Chen, Francis F., *Introduction to Plasma Physics and Controlled Fusion*, Volume 1, Plenum Press, New York, 1984.

Collin, Robert E., *Antennas and Radio Wave Propagation*, McGraw-Hill, New York, 1985.

Dysthe, K. B., E. Mjϕlhus, H.L. P$\acute{e}$cseli and K. Rypdal, Thermal cavitons. *Phys. Scripta, T2*, 548-559, 1982.

Frolov, V. L., S. M. Grach, L. M. Erukhimov, G. P. Komrakov, E. N. Sergeev, B. Thidé, and T. Carozzi, Peculiarities in the evolution of the BUM of stimulated radio emission of the ionosphere, *Radiophys. Quant. Electron.*, Engl. Transl., *39*(3), 241-254, 1996.

Frolov, V. L., L. M. Erukhimov, L. M. Erukhimov, E. N. Sergeev, B. Thidé, P. A. Bernhart, L. S. Wagner, J. A. Goldstein, and C. A. Selcher, On effect of enhancement of BUM coming to light by additional pulse heating of ionospheric plasma, *Radiophys. Quant. Electron.*, Engl. Transl., *40*(5), 371-386, 1997.

Frolov, V. L., L. M. Ekukhimov, L. M. Kagan, G. P. Komrakov, E. N. Sergeev, and P. Stubbe, Two-component nature of the broad upshifted maximum in stimulated electromagnetic emission spectra, *Phys. Rev. Lett., 181*(8), 1630-1633, 1998.

Goodman, S., B. Thidé, and L. Erukhimov, A combined parametric and conversion mechanism for upshifted electromagnetic emissions, *Geophys. Res. Lett.*, *20,* 735-738, 1993.

Goodman, S., H. Usui, and H. Matsumoto, Particle-in-cell simulations of electromagnetic emissions from plasma turbulence, *Phys. Plasma, 1*(6), 1765-1767, 1994.

Grach, S. M., On kinetic effects in the ionospheric *F*-region modified by powerful radio waves, *Radiophys. Quant. Electron.*, Engl. Transl., *42*(7), 572-588, 1999.

Honary, F., A. J. Stocker, T. R. Robinson, and T. B. Jones, Ionospheric plasma response to HF radio waves operating at frequencies close to the third harmonics of the electron gyrofrequency, *J. Geophys. Res., 100,* 21,489-21,501, 1995.

Huang, J., and S. P. Kuo, A theoretical model for the broad upshifted maximum in stimulated electromagnetic emission spectrum, *J. Geophys. Res., 99,* 19,569-19,576, 1994.

Huang, J. and S. P. Kuo, A generation mechanism for the Downshifted Peak in stimulated electromagnetic emission spectrum, *J. Geophys. Res., 100*, 21,433-21,438, 1995.

Hussein, A. A., and W. A. Scales, Simulation studies of parametric decay instability processes associated with ionospheric stimulated radiation, *Radio Sci., 32*, 2099-2107, 1997.

Hussein, A. A., W. A. Scales, and J. Huang, Theoretical and simulational studies of broad upshifted sidebands generation in the ionospheric stimulated radiation, *Geophys. Res. Lett., 25*, 955-958, 1998.

Ichimaru, S., *Basic Principles of Plasma Physics,* W. A. Benjamin, Inc., 1973.

Kuo, S. P. and B. R. Cheo, Parametric excitation of coupled plasma waves, *Phys. Fluids, 21,* 1753-1757. 1978.

Lee J. K. and C. K. Birdsall,, Velocity space ring-plasma instability, magnetized, Part I: Theory, *Phys. Fluids, 22*, 1306-1314, 1979.

Lee J. K. and C. K. Birdsall,, Velocity space ring-plasma instability, magnetized, Part II: Simulation, *Phys. Fluids, 22*, 1315-1322, 1979.

Lee M. C. and S. P. Kuo, Excitation of upper-hybrid waves by a thermal parametric instability, *J. Plamsa Phys.*, *30*, 463-478, 1983.

Leyser, T. B., B. Thidé, H. Derblom, Å. Hedberg, and B. Lundborg, Stimulated electromagnetic emission near electron cyclotron harmonics in the ionosphere, *Phys. Rev. Lett., 63,* 1145-1147, 1989.

Leyser, T. B., B. Thidé, H. Derblom, Å. Hedberg, B. Lundborg, P. Stubbe, and H. Kopka, Dependence of stimulated electromagnetic emission on the ionosphere and the pump wave, *J. Geophys. Res., 95,* 17,233-17,244, 1990.

Leyser, T. B., B. Thidé, M. Waldenvik, S. Goodman, V. L. Frolov, S. M. Grach, A. N. Karashtin, G. P. Komrakov, and D. S. Kotik, Spectral structure of stimulated electromagnetic emission between cyclotron harmonics, *J. Geophys. Res., 98*, 17,597-17,606, 1993.

Mjølhus, E., A. Hanssen, and D.F. DuBois, Radiation from electromagnetically driven Langmuir turbulence, *J. Geophys. Res., 100*, 17,527-17,541, 1995.

Murtaza, G. and P. K Shukla, Nonlinear generation of electromagnetic waves in a magnetoplasma, *J. Plasma Phys., 31,* 423-436, 1984.

Robinson, T. R., F. Honary, A. J. Stocker, T. B. Jones, and P. Stubbe, First EISCAT observations of the modification of *F*-region electron temperatures during RF heating at harmonics of the electron gyro frequency, *J. Atmos. Terr. Phys., 58*, 385-395, 1996.

Rönnmark, K., Computation of dielectric tensor of a Maxwellian plasma, *Plasma Phys., 25*, 699-701, 1983.

Scales, W. A., K. T. Cheng, and S. Srivastava, Simulation studies of processes associated with stimulated electromagnetic emission in the ionosphere, *J. Atmos. Terr. Phys., 59*, 2373-2381, 1997.

Scales, W. A. and H. Xi, Theoretical and numerical simulation investigation of parametric processes associated with up-shifted ionospheric stimulated radiation, *Phys. Scr., T84*, 184-187, 2000.

Sergeev, E. N., V. L. Frolov, G. P. Komrakov, B. Thidé, and T. Carozzi, Temporal evolution of HF-excited plasma waves, measured at differentpump frequencies by stimulated electromagnetic emission (SEE), *J. Atmos. Terr. Phys., 59*(18), 2383-2400, 1997.

Shvarts, M. M. and S. M. Grach, Iteraction of upper and lower hybrid waces and generation of the downshifted maximum feature of stimulated electromagnetic emissions. *J. Atmos. Terr. Phys., 59*, 2421-2429, 1997.

Stenflo, L., Stimulated scattering of large-amplitude waves in the ionosphere, *Phys. Scr., T30*, 166-169, 1990.

Stenflo, L. and P.K. Shukla, Generation of radiation by upper-hybrid waves in non-uniform plasmas, *Planet. Space Sci., 40,* 473-476, 1992.

Stubbe, P., H. Kopka, B. Thidé, and H. Derblom, Stimulated electromagnetic emission: A new technique to study the parametric decay instability in the ionosphere, *J. Geophys. Res., 89,* 7523-7536, 1984.

Stubbe, P., and H. Kopka, Stimulated electromagnetic emission in a magnetized plasma: a new symmetric spectral feature, *Phys. Rev. Lett., 65*, 183-186. 1990.

Stubbe, P., A. J. Stocker, F. Honary, T. R. Robinson, and T. B. Jones, Stimulated electromagnetic emissions and anomalous hf wave absorption near electron gyroharmonics, *J. Geophys. Res., 99,* 6233-6246, 1994.

Thidé, B., H. Kopka, and P. Stubbe, Observations of stimulated scattering of a strong high-frequency radio wave in the ionosphere, *Phys. Rev. Lett., 49,* 1561-1564, 1982.

Tripathi, V. K., and C. S. Liu, *O*-mode decay and upshifted electromagnetic emissions near cyclotron harmonics in the ionosphere, *J. Geophys. Res., 98*, 1719-1723, 1993.

Wagner, L. S., P. A. Bernhardt, J. A. Goldstein, C. A. Selcher, V. L. Frolov, and E. N. Sergeev, Effect of ionospheric self-conditioning and preconditioning on the broad upshifted maximum component of stimulated electromagnetic emission, *J. Geophys. Res., 104*, 2573-2590, 1999.

Wang, J. G., D. L. Newman, and M. V. Goldman, Vlasov simulation of electron heating by Langmuir turbulence near the critical altitude in the radiation-modified ionosphere, *J. Atmos. Terr. Phys., 59*(18), 2461-2474, 1997.

Xi, H. and W. A. Sclaes, Numerical simulation studies on the broad upshifted maximum of ionospheric stimulated electromagnetic emission, *J. Geophys. Res., 106*, 12,787-12,801, 2001.

Yoon, P. H., A. T. Weatherwax, T. J. Rosenberg and J. LaBelle, Lower ionospheric cyclotron maser theory: A possible source of $2f_{ce}$ and $3f_{ce}$ auroral radio emissions, *J. Geophys. Res., 101*, 27,015-27,026, 1996.

Zheleznyakov, V. V., and E. YA. Zlotnik, Cyclotron wave instability in the corona and origin of solar radio emission with fine structure, *Sol. Phys., 43*, 431-451, 1975.

Zhou, H. L., J. Huang and S. P. Kuo, Cascading of upper hybrid/electron Bernstein wave in the ionospheric heating experiments, *Phys. Plasmas, 1,* 3044-3052, 1994.

Vita

Hong Xi was born in Hubei, P. R. China in 1971. He received his B.S. and M.S. in engineering from Nanjing University of Aeronautics and Astronautics, P. R. China in 1993 and 1996 respectively. Upon graduation he stayed with Beijing Institute of Control Engineering for one year. In 1997 he was accepted as a Ph.D student in Electrical Engineering at Virginia Tech where he was privileged to work under the supervision of Dr. Wayne A. Scales in the area of numerical simulation of ionospheric electromagnetic emission. From May 2000 he started to work for Hughes Network Systems as a software engineer in the fields of network management systems, wireless and satellite communication systems, and e-commerce. Since March 2004 he has been a team leader and senior developer with Freddie Mac. Hong's areas of interest are broad, including numerical simulation, software engineering, telecommunication and computer networks.